

UCSF

UC San Francisco Electronic Theses and Dissertations

Title

Concurrent loss of FTD genes C9orf72 and Grn exacerbates neuroinflammation via autoimmune dysfunction

Permalink

<https://escholarship.org/uc/item/1nt629c3>

Author

Jahan, Naznin

Publication Date

2024

Peer reviewed|Thesis/dissertation

Concurrent loss of FTD genes C9orf72 and Grn exacerbates neuroinflammation via autoimmune dysfunction

by
Naznin Jahan

DISSERTATION
Submitted in partial satisfaction of the requirements for degree of
DOCTOR OF PHILOSOPHY

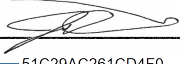
in

Biomedical Sciences

in the

GRADUATE DIVISION
of the
UNIVERSITY OF CALIFORNIA, SAN FRANCISCO

Approved:

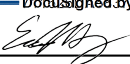
DocuSigned by:

51C29AC261CD4F0... Jayanta Debnath
Chair

DocuSigned by:

Aimee Kao

DocuSigned by:

Saul Villeda

DocuSigned by:

9A805C3F0428410... Dr. Eric Huang

Committee Members

Copyright 2024

by

Naznin Jahan

Dedication

To Ammu and Abbu,

The ones who gifted my life and learning and made me the person I am today,

With heartfelt gratitude,

Naznin

Acknowledgments

Just as they say, “It takes a village to raise a child”, this project would not have been possible without the incredible support of my colleagues, family, and friends. I owe my mentor, Dr. Eric Huang, a tremendous debt of gratitude. His guidance, patience, and expertise in pathology and neurodegeneration have been invaluable throughout my doctoral journey. He has been there through the highs and lows, providing crucial advice and support that helped shape this project and the fellowships I pursued. I cannot thank him enough for helping me navigate some of the toughest moments of the past six years. Second, I would like to thank my committee members: Drs Jay Debnath, Saul Villeda, and Aimee Kao, whose suggestions during our yearly meetings have helped shape the trajectory of this project. Many thanks to our collaborating labs of Dr. Christine Hseih, Dr. Michael Wilson, and Dr. Jimmie Ye whose scientific expertise helped improve my thesis project.

My scientific journey at UCSF would not have been complete without the day-to-day welcoming generosity of all the past and present Huang lab members. I especially want to thank Dr. Jiasheng Zhang, and Dr. Yu-Hsin Huang whose meticulous help with general lab procedures, primary mouse cultures, and quantifications was crucial in generating some of the data. Dr. Rufei Lu and Jennifer Choi’s knowledge of handling sequencing data was crucial in understanding some of the intricacies of this project. Not only were they an immense source of support and knowledge in carrying out experiments, but their fun sense of humor and comradery helped make the long days in the lab feel less tiresome. I want to shout out to our mouse expert Yao Xuan and my ex-lab partners in crime Lana Ho and Dr. Elise Marsan, who made the lab feel like home.

Outside of lab, I am fortunate to have a supportive group of friends and mentors, who have helped me power through tough times, explore the city, and try different activities. While I may not have named each of you individually, please know that your presence has made a profound impact on my journey. I want to thank my undergraduate mentor Dr. Daniela Kaufer, whose encouragement has led me to pursue graduate school. I want to also thank Dr. Anita Sil and Dr. Mercedes Paredes for their sage life advice and patience as I navigated the challenges of graduate school. Big thanks to my friends Oscar, Andres, Alex, Dianne, Yash, Mohini, Kadelynn, Max, Jackson, Walter, Mago, and Rhogerry for always being up for quality time together, whether it was lounging, cooking dinner, hiking, or trying out new restaurants. Your companionship and support have truly made this journey enjoyable, and I cannot thank you enough for also keeping me well-fed along the way. I would like to also express my gratitude to my friend and fellow PhD student, Jiapei, for embracing our artistic explorations together. Last but not least, I extend my heartfelt gratitude to Tiffany Lam and the First Generation to College Community at UCSF for their invaluable support in helping me tackle moments of imposter syndrome while navigating various leadership roles.

I am immensely grateful to my family for their unwavering belief in my education and steadfast support as the first in our family to pursue graduate studies. Their prayers and encouragement have been my guiding light throughout this journey. To my mother and brother: we have weathered many challenges together, and I hope to have brought you pride as I near the end of this chapter of my life. My love for you transcends what can be captured in these pages.

Concurrent loss of FTD genes *C9orf72* and *Grn* exacerbates neuroinflammation via autoimmune dysfunction

by Naznin Jahan

Abstract

The majority of familial FTD stems from mutations in *Progranulin* (*GRN* gene, PGRN protein) or hexanucleotide (CCCCGG) repeat expansion in *C9orf72* gene. Recent studies highlight the key roles of *C9orf72* and PGRN in endo-lysosomal trafficking, with their deficiencies causing abnormal microglial activation in the aging brain. Alongside potential interactions between PGRN and *C9orf72* in vesicle trafficking, there are documented instances of concurrent mutations in both *C9orf72* and *GRN* genes linked to earlier disease onset and heightened neurodegeneration in familial cases of FTD-ALS spectrum disease. In my thesis work, I hypothesized that simultaneous deletion of *C9orf72* and *GRN* exacerbates neuroinflammation and neurodegeneration. To test this, I generated aging cohorts of *wild type* (*WT*), *Grn*^{-/-}, *C9orf72*^{-/-}, and *Grn*^{-/-};*C9orf72*^{-/-} mice. *Grn*^{-/-};*C9orf72*^{-/-} mice exhibited heightened microgliosis and astrogliosis, extending beyond the thalamocortical circuit, and disrupted blood-brain barrier. Brain RNA-seq revealed novel transcriptomics signatures of increases in B-cell receptor signaling in *Grn*^{-/-};*C9orf72*^{-/-} mice. CITE-seq and flow cytometry revealed age-dependent clonal expansions of age-associated B cells and activated B cells. PhIP-seq and protein arrays demonstrated that clonally expanded B cells produced autoantibodies that target many neural antigens, including axon guidance protein ROBO3. Together, these results support that concurrent loss-of-function in both *C9orf72* and *Grn* genes intensify neuroinflammation and peripheral immune system defects, thereby synergistically promoting neurodegeneration.

TABLE OF CONTENTS

Introduction.....	1
Epidemiology and Clinical Manifestation of FTD.....	1
Pathology and Genetics of FTD.....	3
<i>GRN</i> and <i>C9orf72</i> Mutations in FTD.....	5
FTD and Immune Dysfunction in CNS and Peripheral organs.....	8
PGRN and <i>C9orf72</i> interaction in immune homeostasis.....	10
Chapter 1: Generation and characterization of <i>Grn</i>^{-/-}, <i>C9orf72</i>^{-/-} and <i>Grn</i>^{-/-};<i>C9orf72</i>^{-/-} mice.....	11
Introduction.....	12
Results	
<i>Grn</i> ^{-/-} ; <i>C9orf72</i> ^{-/-} mice exhibit earlier lethality compared to <i>Grn</i> ^{-/-} , <i>C9orf72</i> ^{-/-} mice.....	13
<i>C9orf72</i> ^{-/-} and <i>Grn</i> ^{-/-} ; <i>C9orf72</i> ^{-/-} mice have splenomegaly and lymphadenopathy.....	13
<i>C9orf72</i> ^{-/-} and <i>Grn</i> ^{-/-} ; <i>C9orf72</i> ^{-/-} mice have elevated antibodies against Double-stranded DNA (ds-DNA) and anti-nuclear antigens (ANA).....	14
<i>C9orf72</i> ^{-/-} and <i>Grn</i> ^{-/-} ; <i>C9orf72</i> ^{-/-} mice have increased levels of immunoglobulins.....	15
Circulating C1q and C3 levels do not show significant changes in mice of different genotypes.....	17
<i>C9orf72</i> ^{-/-} and <i>Grn</i> ^{-/-} ; <i>C9orf72</i> ^{-/-} mice exhibit glomerulonephritis similar to that seen in SLE patients.....	18
Discussion.....	19

Chapter 2: Neuropathological characterization of <i>Grn</i>^{-/-}, <i>C9orf72</i>^{-/-} and <i>Grn</i>^{-/-}; <i>C9orf72</i>^{-/-} mice...	24
Introduction...	25
Results	
<i>Grn</i> ^{-/-} ; <i>C9orf72</i> ^{-/-} mice have increased gliosis compared to that in <i>Grn</i> ^{-/-} , and <i>C9orf72</i> ^{-/-} mice...	26
<i>Grn</i> ^{-/-} ; <i>C9orf72</i> ^{-/-} mice have a more compromised blood brain barrier (BBB) compared to that in <i>Grn</i> ^{-/-} , <i>C9orf72</i> ^{-/-} mice...	29
<i>Grn</i> and <i>C9orf72</i> have opposing functions in the excitatory neuronal population in the limbic region...	31
Knockout mice have mis-localization of nuclear proteins...	33
<i>Grn</i> ^{-/-} ; <i>C9orf72</i> ^{-/-} mice show an age dependent increase in inflammation and B-cell receptor signaling...	34
<i>Grn</i> ^{-/-} ; <i>C9orf72</i> ^{-/-} mice have increased immune activation, blood vessel morphogenesis and regulation related gene signatures in non-neuronal cells.	35
Discussion...	38
Chapter 3: Multi-omic characterization of <i>Grn</i>^{-/-}, <i>C9orf72</i>^{-/-} and <i>Grn</i>^{-/-};<i>C9orf72</i>^{-/-} of peripheral immune cells...	52
Introduction...	53
Results	
<i>Grn</i> ^{-/-} ; <i>C9orf72</i> ^{-/-} mice have and increased proportion of reactive B-cells population...	54
<i>Grn</i> ^{-/-} ; <i>C9orf72</i> ^{-/-} mice have shared autoantibodies that target peripheral and	

CNS cells.....	55
Discussion...	56
Chapter 4: Neuronal and microglial characterization of all four genotypes	
<i>in-vitro</i> (In Progress).....	59
Introduction.....	60
Results	
Anti-ROBO3 does not affect the survival of neurons <i>in vitro</i>	60
<i>Grn</i> ^{-/-} microglia show increased accumulation of zymosan beads over time.....	61
Discussion.....	64
Future Directions.....	65
Materials and Methods.....	67
References...	79

LIST OF FIGURES

Figure 1.1. Increased peripheral immune dysfunction in <i>C9orf72</i> ^{-/-} and <i>Grn</i> ^{-/-} ; <i>C9orf72</i> ^{-/-} mice.....	21
Figure 1.2. <i>C9orf72</i> ^{-/-} and <i>Grn</i> ^{-/-} ; <i>C9orf72</i> ^{-/-} mice have elevated levels of immunoglobulins.....	22
Figure 1.3. <i>C9orf72</i> ^{-/-} and <i>Grn</i> ^{-/-} ; <i>C9orf72</i> ^{-/-} mice exhibit glomerulonephritis similar to that seen in SLE patients.....	23
Figure 2.1. <i>Grn</i> ^{-/-} ; <i>C9orf72</i> ^{-/-} mice have increased gliosis compared to that in <i>Grn</i> ^{-/-} , <i>C9orf72</i> ^{-/-} mice.....	41
Figure 2.2. <i>Grn</i> ^{-/-} ; <i>C9orf72</i> ^{-/-} and <i>Grn</i> ^{-/-} mice have compromised blood brain barrier (BBB) and inflammatory markers.....	43
Figure 2.3. <i>Grn</i> ^{-/-} ; <i>C9orf72</i> ^{-/-} mice have a more compromised blood brain barrier (BBB) compared to that in <i>Grn</i> ^{-/-} , <i>C9orf72</i> ^{-/-} mice.....	44
Figure 2.4. Thalamic neuronal loss in 12 months <i>Grn</i> ^{-/-} ; <i>C9orf72</i> ^{-/-} and <i>Grn</i> ^{-/-} ; <i>C9orf72</i> ^{-/-} mice brain thalamus.....	45
Figure 2.5. Distribution of Pkcδ ⁺ neurons in the 12 months old brain of all four genotypes.....	46
Figure 2.6. Neuronal nuclear protein mislocalization in knockout mice thalamus.....	47
Figure 2.7. Heatmap of bulk-transcriptomic analysis of WT, <i>Grn</i> ^{-/-} , <i>C9orf72</i> ^{-/-} and <i>Grn</i> ^{-/-} ; <i>C9orf72</i> ^{-/-} mice at ages 7 and 12 months old show age dependent changes in DEGs and pathways involved.....	48
Figure 2.8. Increased inflammatory and antigen presentation signatures in <i>Grn</i> ^{-/-} ; <i>C9orf72</i> ^{-/-} microglial cluster.....	49

Figure 2.9. Contribution of astrocytes and endothelial cells in *Grn*^{-/-}, and *Grn*^{-/-};*C9orf72*^{-/-} mice brain thalamus BBB disruption.....50

Figure 3.1. Expansion of B-Cell subsets in *Grn*^{-/-};*C9orf72*^{-/-} mice peripheral immune tissues 57

Figure 3.2. Sankey Plot of autoantibody targets from CDI microarray analysis of *WT*, *Grn*^{-/-}, *C9orf72*^{-/-} and *Grn*^{-/-};*C9orf72*^{-/-} mice blood plasma at 7 months58

Figure 4.1. Figure 4.1. *In vitro* *WT*, *Grn*^{-/-}, *C9orf72*^{-/-} and *Grn*^{-/-};*C9orf72*^{-/-} neuron and microglial culture...63

Introduction

Frontotemporal dementia (FTD), characterized by progressive and selective degeneration of the frontal and temporal lobe of the brain among younger patients, presents as a distinct entity within the vast spectrum of neurodegenerative diseases. Although rarer in occurrence than its more well-known counterparts like Alzheimer's disease (AD), the heterogeneity of the clinical presentation of FTD presents both the challenge in its diagnosis and treatment, and an opportunity to uncover unknown mechanisms of disease progression that are common among multiple types of neurodegenerative diseases. Current literature established inflammation as one of the common etiologies leading to neurodegenerative diseases. As recent studies bring attention to the potential involvement of autoimmune dysregulation in the initiation and progression of FTD, the connection between the two diseases brings a novel dimension to our understanding of FTD etiology, with strong implications for diagnostic approaches and therapeutic interventions made us embark on the quest to elucidate the dialogue between the two occurrences. Thus, to elucidate the dialogue between the two occurrences, this thesis explores the complex interplay between aberrant immune responses that underscore autoimmune dysregulation and frontotemporal dementia.

Epidemiology and Clinical Manifestation of FTD

FTD (previously known as Pick's disease) was first described by Czech neurologist Arnold Pick almost 100 years ago, recording patients with slow progressive language and behavioral disorders (Hofmann et al., 2019; Olszewska et al., 2016). It is the second to third most prevalent form of dementia after Alzheimer's Disease (AD), representing 5–10% of all dementia and 10–20% cases under age 65 (Hofmann et al., 2019; Olszewska

et al., 2016). FTD encompasses a group of progressive early-onset dementia syndrome in patients such as changes in behavior, executive functions, language, or motor function (Olszewska et al., 2016). While FTD has undergone various categorical and nomenclature changes, currently the term is used to identify the core FTD spectrum disorders, including behavioral variant FTD (bvFTD) behavioral variant FTD, nonfluent/agrammatic variant progressive primary aphasia (nfvPPA) primary progressive aphasia, and semantic variant PPA (svPPA). Related FTD disorders include frontotemporal dementia with motor neuron disease (FTD-MND) motor neuron disease, progressive supranuclear palsy syndrome (PSP-S) progressive supranuclear palsy, and corticobasal syndrome (CBS) (Olney et al., 2017). Currently no disease modifying treatment is available for FTD, and patients can only receive treatments to alleviate certain symptoms (e.g. antipsychotics and behavioral therapy targeting irrational or unacceptable behaviors, and physical therapy to aid with motor dysfunction in patients) (Hofmann et al., 2019).

In a recent study, the prevalence of FTD was estimated to be in between 0.01-4.61 per 1000 person and the incidence rate to be in between 0.01-2.5 per 1000 person/year (Hogan et al., 2016; Leroy et al., 2021). Dementia cohort studies in Sweden and Amsterdam suggest that FTD accounts for 1.6-7% of dementia cases (Religa et al., 2015; Van Der Flier & Scheltens, 2018). These studies need to be considered with caution due to known issues of FTD being underdiagnosed. Some of the factors resulting in the underdiagnosis of FTD stems from misdiagnosis and delay in diagnosis compared to other dementias, (Rosso, 2003; Van Vliet et al., 2013) due to its varied nature of manifestation. Yet advances in genetic screening, cerebrospinal fluid (CSF) biomarkers,

neuroimaging, and neuropsychology have improved FTD diagnosis in challenging situations such as psychiatric, amnesic, or late-onset presentations of the disease (Ducharme et al., 2015).

Pathology and Genetics of FTD

Histopathological hallmarks of FTD involve neuronal loss, gliosis, and abnormal protein aggregation involving Transactive response DNA binding protein 43 (TDP-43), FUS (fused in sarcoma), or Tau] in frontal and temporal lobes. The neuropathological diagnosis for FTD, also known as frontotemporal lobar degeneration (FTLD), can be classified into 3 major categories according to the types of protein aggregation: FTLD-Tau, FTLD-TDP and FTLD-FUS; each of which can be further divided into subtypes based on the morphology and distribution of the protein inclusions (Hofmann et al., 2019). Although FTLD-Tau was discovered first, FTLD-TDP has a greater prevalence compared to the other subtypes, accounting for greater than 50% of all FTD cases (Hashimoto et al., 2022). In addition to being prominent in FTLD, TDP-43 inclusion is also present as a major protein inclusion in amyotrophic lateral sclerosis (ALS), in some AD patients, and in the healthy aging population, suggesting the broader implication of TDP-43 protein aggregates in the brain. The remaining 5-10% of FTD patients that had ubiquitin-positive, Tau, and TDP negative inclusions were later shown to have FUS protein-containing inclusions similar to ALS patients with mutations in *FUS* gene (Hofmann et al., 2019).

Between 20-50% of FTD cases have a family history of dementia, with 10% of cases having a clear autosomal dominant inheritance pattern (Benussi et al., 2015; Olszewska et al., 2016; Rohrer et al., 2009). Cross-sectional studies performed over the

last decade estimated that up to 50% of ALS patients develop FTD related cognitive impairment, while up to 30% of FTD patients develop motor dysfunction (Ambrazon 2020). Given the known link between ALS and FTD protein inclusions, it is considered that FTD and ALS diseases are on a spectrum, with the shared genetic mutations manifesting in either or both of the conditions. Three of the most common mutations causing familial FTD are *MAPT*, *GRN*, and the (GGGGCC)_n hexanucleotide repeat expansion (HRE) in the *C9orf72* gene (Pottier et al., 2016). Rare FTLD disease-associated genes include *CHCHD10* (coiled-coil-helix-coiled-coil-helix domain containing 10), *CHMP2B* (charged multivesicular body protein 2B), *DCTN1* (dynactin 1), *FUS*, *hnRNPA1* (heterogeneous nuclear ribonucleoprotein A1), *hnRNPA2B1* (heterogeneous nuclear ribonucleoprotein A2/B1), *OPTN* (optineurin), *SQSTM1* (sequestosome 1; p62), *TARDBP*, *TBK1*, *TIA1*, *UBQLN2* (ubiquilin 2), and *VCP*. FTLD patients with atypical clinical presentations have mutations in *CSF1R* (colony stimulating factor 1 receptor), *PRKAR1B* (protein kinase cAMP-dependent type I regulatory subunit beta), and *TREM2* (triggering receptor expressed on myeloid cells 2), while other genes implicated in increasing the risk for FTLD include the *HLA* locus on chromosome 6p21.3, *CTSC* (cathepsin C) and *RAB38* on chromosome 6p21.3. Shared genes among FTD and ALS include *TARDBP*, *SQSTM1*, *VCP*, *FUS*, *TBK1*, *CHCHD10*, and most importantly *C9orf72*. Mutations in *GRN* and *C9orf72* are the most prevalent familial form of FTD mutations, each accounting for 13.9% and 25.5% of all FTD cases respectively. Both *GRN* and *C9orf72* mutations are also the most prevalent neuropathological type of FTLD: FTLD-TDP (Hashimoto et al., 2022; Pottier et al., 2019). This along with their possible convergent cellular mechanisms, is discussed in the following sections of my thesis, again

underscoring the importance of investigating the role of PGRN and C9orf72 protein in FTD disease progression.

GRN and C9orf72 Mutations in FTD

The human *Progranulin* [*GRN* gene; PGRN protein] gene located in chromosome 17q21 encodes an 88 kDa secretory glycosylated protein containing a signal peptide and 7.5 tandem repeats of highly conserved granulin motifs each with 12 cysteine residues (He & Bateman, 2003; Van Damme et al., 2008). PGRN is widely expressed with pleiotropic effects such as development, tumor growth and proliferation, vasculogenesis, wound healing, and inflammation (Ahmed et al., 2007; Bateman & Bennett, 1998, 2009; Bhandari et al., 1993; Daniel et al., 2003; He & Bateman, 2003). In peripheral tissues, extracellular proteases, such as elastase, have been shown to cleave PGRN into several 6kDa GRNs (GRN A–F and paraganulin), probably performing separate functions (He & Bateman, 2003; Zhu et al., 2002). While both PGRN and granulins are involved in cell growth, PGRN is associated with neuroprotective and anti-neuroinflammatory functions, whereas some studies suggest granulins can exhibit neuroinflammatory properties (Kessenbrock et al., 2008; Salazar et al., 2015).

Two landmark studies in 2006 have pinned that mutations in *GRN* gene, resulting in PGRN haploinsufficiency via either truncated PGRN due to premature stop codon, or loss of mutant transcript due to nonsense mediated RNA decay as a causal link to the familial form of FTD linked to chromosome 17q21 (Baker et al., 2006; Cruts et al., 2006). Interestingly, patients with homozygous mutation in *GRN* develop a lysosomal storage disorder called neuronal ceroid lipofuscinosis (NCL), which lead to the hypothesis of

PGRN being important for lysosomal function and proteostasis (Almeida et al., 2016; Kao et al., 2017; Smith et al., 2012) . In mice models, deficiency in PGRN levels has been associated with age-dependent, progressive upregulation of lysosomal and innate immune genes, increased phagocytic activity in microglia and macrophages, along with increased proinflammatory cytokine (eg. Tumor necrosis factor (TNF), Interleukin-6 (IL-6)) and complement (C1qa, C1qb, C1qc and C3) production, and dysfunction in the thalamocortical circuit via preferential inhibitory synapse loss via C1q-dependent microglia synapse pruning (Y. Chen et al., 2015; Hickman et al., 2018; Lui et al., 2016; Martens et al., 2012; Yin et al., 2010). This mouse model data has been shown to reflect pathology in patients with *GRN* mutation as their CSF show increased levels of C1qa and C3, along with increased microglial infiltration in the frontal cortex (Kao et al., 2017). Furthermore, selective reduction and overexpression studies in the microglia of A β mice (an AD mice *in vivo* model) has shown that PGRN is important in reducing plaque deposition (Minami et al., 2014). Loss of PGRN has also been shown to disrupt autophagy and intracellular trafficking by inhibiting lysosome fusion and autophagosome accumulation in microglia and macrophage. In cortical neurons PGRN appears to have modest effects in regulating autophagic flux and TDP-43 accumulation (Chang et al., 2017). These studies further solidify the case for PGRN being involved in an important immune checkpoint that suppresses aberrant microglial activation.

The human *Chromosome 9 open reading frame 72 (C9orf72)* gene encodes a protein that belongs to the Differentially Expressed in Normal and Neoplastic cells (DENN)-domain protein family and its function is an active area of research. Studies have shown it being involved in activation of Rab-GTPases via its Guanine nucleotide

exchange factor (GEF) activity (Levine et al., 2013). In humans, alternative splicing of *C9orf72* gene product results in a short 25kDa and a long 55kDa isoform of the protein, whereas in mice, 3 isoforms of sizes 35kDa, 50kDa, and 55kDa are produced (Atkinson et al., 2015; Xiao et al., 2015). Bioinformatic and structural analysis suggests that the long isoform of *C9orf72* is more abundantly produced, has structural homology to FLCN binding protein 1 and 2 (FNIP1/2), and forms a heterodimer with SMRC8 and WDR41 (similar to FNIP1/2:FLCN heterodimer) (Amick et al., 2016; Amick & Ferguson, 2017). Both *C9orf72*:SMRC8:WDR41 and FNIP1/2:FLCN heterodimers colocalize near lysosomes and are implicated in membrane trafficking and cellular nutrient sensing via mechanistic target of rapamycin (mTOR1) pathway regulation. Not only that, *C9orf72* proteins have a critical role in the autophagy-lysosome pathway via regulating autophagy initiation by controlling the expression and activity of ULK1 (Amick et al., 2016; Sullivan et al., 2016; Yang et al., 2016). It has also been shown that *C9orf72* deficiency leads to dysregulated autophagic digestion which induces endoplasmic reticulum-derived lipid droplets accumulation and free fatty acid secretion under nutrient stress due to its involvement in supporting coactivator-associated arginine methyltransferase 1 (CARM1)-related autophagy-lysosome pathway (Liu et al., 2018).

Intronic (GGGGCC)_n hexanucleotide repeat expansion (HRE) ($n > 30$) within the non-coding of exon 1a and 1b of *C9* gene is reported to cause neurodegeneration in FTD and ALS via three potential mechanisms: 1) toxic gain of function (GOF) via HRE-containing RNA foci and RNA/DNA-G quadruplex formation; 2) toxic GOF via repeat associated-non ATG (RAN)-translation and formation of dipeptide repeats; and 3) *C9orf72* protein haploinsufficiency, which in essence leads to a loss of function (LOF) in

C9orf72 protein (Gendron & Petrucelli, 2018). While studies have primarily focused on targeting therapeutics against toxic species in neurons, these strategies have not fully rescued the degeneration in patient derived neurons, thus further solidifying the need for investigation of C9orf72 protein function and its role in mediating neuro-immune dysfunction and degeneration in FTD/ALS patients. Interestingly, similar to PGRN deficiency, C9orf72 LOF results in lysosomal accumulation and altered immune responses in microglia and macrophages (McCauley et al., 2020a; O'Rourke et al., 2016), suggesting that C9orf72 haploinsufficiency can facilitate neurodegeneration in FTD by disrupting glia-neuron homeostasis in CNS.

FTD and Immune Dysfunction in CNS and Peripheral organs

FTLD-TDP patients, especially those who are either *GRN* or *C9orf72* mutation carriers tend to have cooccurrences of autoimmune diseases. Compared to AD patients and age-matched controls, FTLD-TDP patients have an increased prevalence of non-thyroid autoimmune diseases, such as inflammatory arthritis, cutaneous disorders, and gastrointestinal conditions (Hashimoto et al., 2022; Miller et al., 2013, 2016). Multiple lines of evidence corroborate the dual presence of peripheral immune and central nervous system dysregulation that leads to FTD-TDP pathology. E.g. elevated levels of plasma tumor necrosis factor alpha (TNF- α) present in patients with *GRN* mutations, as well as patients with rheumatoid arthritis (RA) and systemic lupus erythematosus (SLE), have a higher propensity of carrying intermediate repeat expansion length (n= 9-30) of G₄C₂ in the 5' intronic region of C9orf72 (Fredi et al., 2019; Hashimoto et al., 2022).

Consistent with the above-mentioned clinical features, mouse models of *Grn* and *C9orf72* LOF mutations show peripheral immune dysfunction and shorter lifespan. *Grn*^{-/-} mice tend to present dysfunction in various organs such as liver, spleen and the brain. In the periphery, *Grn*^{-/-} macrophages produce proinflammatory cytokines and have impaired pathogen clearing abilities, possibly due to reduced lysosomal clearing ability (Yin et al., 2010). In the CNS, *Grn*^{-/-} mice have shown age dependent transcriptomic changes towards a proinflammatory state, preferential expansion of microglia in the thalamocortical circuit and cerebellar white matter, resulting in OCD like behavior, and gait balance in mice (Krabbe et al., 2017; Lui et al., 2016; J. Zhang et al., 2020).

Interestingly, while there are signatures of CNS inflammatory changes, *C9orf72*^{-/-} mice show profound autoimmune dysregulation, which contributes to their reduced lifespan. RNA-seq of *C9orf72*^{-/-} mouse brain show features that activate the interferon signaling and lysosomal dysfunction, as well as increased detection of *C9orf72* transcript in microglia followed by that in neurons (O'Rourke et al., 2016). However, the most striking feature in these mice is lymphadenopathy, splenomegaly, and glomerulonephritis as a result of their prominent autoimmune dysregulation, which can be recapitulated by selective loss of *C9orf72* in the myeloid population using the CX3Cr1-Cre (Atanasio et al., 2016; Burberry et al., 2016; O'Rourke et al., 2016). *C9orf72*^{-/-} has been shown to induce STING-mediated interferon activation in peripheral myeloid cells, as well as in microglia in the CNS, thus promoting C1q mediated neuronal synapse pruning in aging mouse brain (Lall et al., 2021; McCauley et al., 2020b).

Given this information, it is logical to conclude that both *C9orf72* and *GRN* gene products are involved in possible peripheral and CNS immune regulation and that the

mutations result in a vicious cycle where immune dysregulation between the CNS and the periphery cooperates to promote neurodegeneration in FTD patients. Due to their involvement in the autophagy-lysosomal pathways, both PGRN and C9orf72 protein may regulate the myeloid population in both the CNS and the periphery in a similar manner.

PGRN and C9orf72 interaction in immune homeostasis

Given the wealth of literature on *PGRN* and *C9orf72* mutation, my thesis work aims to investigate the intracellular interaction that have been overlooked previously. Consistent with the role of *C9orf72* and *PGRN* in neuroinflammation, several transcriptomic datasets show that *C9orf72* and *GRN* mRNA are highly expressed in microglia in human and mouse brain followed by neurons and astrocytes (Lui et al., 2016; O'Rourke et al., 2016; Sharma et al., 2015; Y. Zhang et al., 2014). In addition, clinical studies have shown that co-occurrence of *C9orf72* and *GRN* mutations can be identified in about 1.8% of familial FTD cases who develop more severe pathologies at younger age (Lashley, Tammarn et al., 2014; Testi et al., 2015; Van Blitterswijk et al., 2013). Furthermore, the patients with dual *GRN* and *C9orf72* mutation reportedly exhibit Celiac diseases (a known immune mediated disease). Although comprehensive characterization of the neuropathology in these cases is still lacking, these studies raise the possibility that *C9orf72* and *PGRN* may cooperatively regulate glia-neuron homeostasis during brain aging as well as peripheral immune homeostasis. Since both *C9orf72* and *PGRN* are implicated in the autophagy-endolysosomal pathway, the exacerbated phenotype seen in these patients could be attributed to the synergistic disruption in these pathways.

Chapter 1

Generation and characterization of *Grn*^{-/-}, *C9orf72*^{-/-} and *Grn*^{-/-};*C9orf72*^{-/-} mice

Introduction

Previous studies from our lab show that, compared to *wild type (WT)* littermates, *Grn*^{-/-} mice exhibit excessive grooming behavior leading to skin ulceration that starts as early as 8 months old (Lui et al., 2016). In addition to the grooming and skin phenotypes, around 10% *Grn*^{-/-} mice show motor dysfunction when they reached 19-24 months old. These phenotypes directly contribute to early lethality in these mice (median survival for *Grn*^{-/-} mice was 529 days, compared to 735 days in *WT* mice, $p < 0.0001$, log-rank [Mantel-Cox] test) (Lui et al., 2016). Upon comparing *WT* mice survival with that of *C9orf72*^{-/-} for 500 days' time period, O'Rourke et al have shown no difference between their survival (O'Rourke et al., 2016). Although interestingly, in a later publication, Burberry et al. have shown that there *C9orf72*^{-/-} mice show earlier lethality compared to that of *WT* mice in one mice facility, whereas no difference in lethality in another, suggesting that environmental factors and gut microbiota are heavily involved in the premature mortality caused by *C9orf72* LOF (Burberry et al., 2020). Both O'Rourke and Burberry et al. have shown an increase in spleen weight in *C9orf72*^{-/-} mice compared to that seen in *WT* mice. In another model of conditional *Grn*^{-/-} mice with the first four exon deletions of *Grn* gene, it was shown that the spleen size to body ratio of these *Grn*^{-/-} mice is greater than that of *WT* mice (Jian et al., 2016; Yin et al., 2010). Given the importance of the spleen as a secondary immune organ, these findings suggest immune dysfunction in *Grn*^{-/-} and *C9orf72*^{-/-} mice.

Results

Grn^{-/-};C9orf72^{-/-} mice have earlier lethality compared to Grn^{-/-} and C9orf72^{-/-} mice

I established an aging cohort of *WT*, *C9orf72^{-/-}*, *Grn^{-/-}* and *Grn^{-/-};C9orf72^{-/-}* mice (generated via breeding *C9orf72^{-/-}* and *Grn^{-/-}* mice and subsequent compound breeding of double heterozygous mice to generate *Grn^{-/-};C9orf72^{-/-}* mice). Using Kaplan-Meier's survival curve and log-rank (Mantel-Cox) test for statistical analysis, I found that *Grn^{-/-};C9orf72^{-/-}* mice have a median survival of 442 days (14.5 months), whereas *Grn^{-/-}* and *C9orf72^{-/-}* mice had median survival of 528 day (17.6 months) and 645 days (21.5 months), respectively (compared to median survival of (760 days) 25 months in *WT* mice)(**Figure 1.1a**). The phenotypes that contributed to the lethality in *C9orf72^{-/-}* mice and *Grn^{-/-};C9orf72^{-/-}* mice included skin ulceration, peripheral immune dysfunction, and neuroinflammation.

The following sections further characterize the peripheral immune dysfunction in *Grn^{-/-};C9orf72^{-/-}* mice.

Splenomegaly and lymphadenopathy in C9orf72^{-/-} and Grn^{-/-};C9orf72^{-/-} mice

To investigate the early lethality in *C9orf72^{-/-}* mice and *Grn^{-/-};C9orf72^{-/-}* mice, we performed dissections and gross measurements of peripheral tissues with an emphasis on immune organs such as the spleen and lymph nodes. Gross anatomical observation of all the genotypes showed that *C9orf72^{-/-}* mice and *Grn^{-/-};C9orf72^{-/-}* mice have splenomegaly (enlarged spleen) and cervical lymphadenopathy (cervical lymph node enlargement). Upon normalizing the spleen and lymph node weights to that animals' body

weights, we find a significant increase in the spleen and lymph node weight to bodyweight ratio in both *C9orf72*^{-/-} mice and *Grn*^{-/-};*C9orf72*^{-/-} mice as early as 7 months old and persisted till 12 months old and beyond compared to *WT* and *Grn*^{-/-} mice (**Figure 1.1 d-g**). Interestingly, *C9orf72*^{-/-} mice show an increase in organ size to body ratio from 7 to 12 months old, whereas *Grn*^{-/-};*C9orf72*^{-/-} mice show similar spleen weight to body weight ratio from 7 to 12 months old, and a slight reduction of cervical lymph node weight to body weight ratio from 7 to 12 months old. No difference in spleen or lymph node to body weight ratio is observed between *WT* and *Grn*^{-/-} mice at 7 months old, although a modest increase in spleen weight to body weight is also observed in *Grn*^{-/-} mice at 12 months old.

Taken together, these data corroborate the gross lymphadenopathy and splenomegaly observed in *C9orf72*^{-/-} mice and *Grn*^{-/-};*C9orf72*^{-/-} mice.

C9orf72^{-/-} and *Grn*^{-/-};*C9orf72*^{-/-} mice have elevated antibodies against double-stranded DNA (ds-DNA) and anti-nuclear antigens (ANA)

Normally, due to their containment within the nucleus or mitochondria of the cell, along with quick cytoplasmic DNase degradation nuclear antigens such as ds-DNA are not accessible to the immune system unless released by apoptotic cells post-infection or exposure to stressors (Wang & Xia, 2019). Upon release of ds-DNA, it can be recognized by anti-ds-DNA antibodies which form complexes and act as antigens, stimulating the B-cells by activating the recognition receptors, such as Toll-like receptors (TLRs). TLR7 and TLR9 are the key receptors for the recognition of self-DNA or immune complexes and trigger the production of IFN-1 and inflammatory responses (Santiago-Raber et al., 2009, 2010; Wang & Xia, 2019). Since Atanasio et al. have shown that *C9orf72*^{-/-} mice show

autoantibody production (Atanasio et al., 2016), I investigated whether concurrent loss of C9orf72 and PGRN led to further increase in the levels of autoantibodies in *Grn^{-/-};C9orf72^{-/-}* mice. Using ELISA assays for antibodies against dsDNA (mouse anti-dsDNA Ig(A+G+M) ELISA kit [Alpha Diagnostic, 5110] and nuclear antigens (mouse anti-ANA Ig(A+G+M) ELISA kit [Alpha Diagnostics, 5210]), I found that both anti-ds-DNA and anti-ANA antibodies were indeed elevated in the plasma of *C9orf72^{-/-}* mice and *Grn^{-/-};C9orf72^{-/-}* mice as early as 7 months old and persisted at 12 months old (**Figure 1.1 b-c**). Interestingly, the levels of anti-ANA and anti-dsDNA autoantibody concentrations were higher in *C9orf72^{-/-}* mice compared to that seen in the *Grn^{-/-};C9orf72^{-/-}* mice at 7 months old. Autoantibody levels in *Grn^{-/-};C9orf72^{-/-}* mice persisted at similar levels from 7 to 12 months of age, whereas those in *C9orf72^{-/-}* mice reduced slightly with age. *Grn^{-/-}* mice show a slight increase in the trend of anti-dsDNA antibody presence at 12 months old compared to *WT* mice.

These data support the presence of autoimmune dysregulation in both *C9orf72^{-/-}* mice and *Grn^{-/-};C9orf72^{-/-}* mice as early as 7 months of age. In addition, my results support that *Grn^{-/-}* mice can develop age-associated autoimmune dysregulation.

C9orf72^{-/-} and Grn^{-/-};C9orf72^{-/-} mice have increased levels of immunoglobulins

The presence of elevated levels of antibodies against self-antigens (aka autoantibodies) is a hallmark for autoimmune diseases and plays a role in the diagnosis of the diseases as highly specific biomarkers (Volkov et al., 2022). Immunoglobulins (Ig) or antibodies are produced by plasma cells (activated B lymphocytes) after interacting with immunogens or antigens such as bacterial, viral, and fungal proteins, cellular

antigens, and foreign chemicals. Depending on their functions, there are several isotypes of immunoglobulins (IgA, IgD, IgE, IgG and IgM) and each class can have their subclasses (for example IgG1, IgG2, IgG3 IgG4, IgA1, IgA2 among many others). Among these, IgG, IgM and IgA are known to play a pivotal role in the presence of certain autoimmune diseases, with dysregulation of certain subclasses involved in disease pathogenesis. For example, in systemic lupus erythematosus (SLE) – a devastating autoimmune disease with immune dysregulation targeting many organs in the body – IgG autoantibodies targeting nuclear antigens levels are particularly elevated, contributing to the chronic inflammatory state. Similarly for Rheumatoid Arthritis, another autoimmune disease, elevated IgG IgM and IgA levels plays a crucial role in the immune response (Veys et al., 1976). Given our data showing elevated levels of autoantibodies against nuclear antigen (**Figure 1.1b-c**), I asked whether *Grn*^{-/-}, *C9orf72*^{-/-} and *Grn*^{-/-};*C9orf72*^{-/-} mice also had elevated circulating Ig's in their blood. To test this, I performed ELISAs to measure the levels of mouse IgA (Thermo Scientific, 88-50450-22), mouse IgE (Fisher Scientific, EMIGHE), mouse IgG (Thermo Scientific, 88-50400-22), and mouse IgM (Thermo Scientific, 885047022) in serum. My results showed elevated levels of total Ig(A+E+G+M) in *C9orf72*^{-/-} mice and *Grn*^{-/-};*C9orf72*^{-/-} mice at 7 months of age compared to that in *WT* and *Grn*^{-/-} mice (**Figure 1.2a-d**). IgE levels in *C9orf72*^{-/-}, and *Grn*^{-/-};*C9orf72*^{-/-} mice were modestly elevated compared to *WT* and *Grn*^{-/-} mice. Except for IgM levels which increase from 7 to 12 months old *C9orf72*^{-/-} mice, both IgG and IgA levels decrease with age in *C9orf72*^{-/-} mice. IgM and IgG levels in blood serum of *Grn*^{-/-};*C9orf72*^{-/-} mice remain similar across 7 to 12 months of age with a slight age related elevation in IgA

levels. Between *C9orf72*^{-/-} and *Grn*^{-/-};*C9orf72*^{-/-} mice, I consistently observed higher levels of immunoglobulins (A+G+M) in *C9orf72*^{-/-} mice, except for IgE levels.

Serum C1q and C3 levels show no significant changes in mice of different genotypes

Our lab has previously shown that C1q and C3 RNA and protein levels are higher in *Grn*^{-/-} mouse brain as early as 9 months of age (Lui et al., 2016). In addition, the complement system is activated in almost all antibody-mediated autoimmune diseases (Thurman & Yapa, 2019). To investigate the levels of circulating complements in mice, I performed ELISA for C1q (Human Complement C1q ELISA Kit [Abcam, ab170246]) and C3b levels (Human Complement C3b ELISA Kit [Abcam, ab170246]). Although the changes in circulating C1q were not significantly different among the different genotypes in both 7 and 12 months of age, at 7 months of age, the trend of concentration presents to be modestly higher in *Grn*^{-/-};*C9orf72*^{-/-} mice followed by that in *C9orf72*^{-/-} mice and *Grn*^{-/-} mice when compared to that of *WT* mice (**Figure 1.2e**). Although the trend between the genotypes remains similar at 12 months of age, the total concentration of circulating C1q is modestly decreased for all genotypes compared to that seen at 7 months of age. For C3b, no significant changes are observed among the genotypes at 7 and 12 months of age, although C3 levels are modestly elevated in *C9orf72*^{-/-} mice and *Grn*^{-/-} mice (**Figure 1.2f**). Taken together, the circulating levels of complement C1q and C3b are not significantly different between the genotypes at 7 months and 12 months.

Glomerulonephritis in C9orf72^{-/-} and Grn^{-/-};C9orf72^{-/-} mice

Our data support that *C9orf72^{-/-}* mice and *Grn^{-/-};C9orf72^{-/-}* mice exhibit immune dysregulation as early as 7 months of age. Given the elevated levels of IgA, IgG, and IgM at 12 months of age, I hypothesized that immune cell infiltration and subsequent damage could occur in peripheral organs in *Grn^{-/-};C9orf72^{-/-}* mice – a common pathologic feature observed in patients with autoimmune diseases. To test this, I performed a series of immunohistochemical stains on the liver, lungs, and kidneys, which are known to be prominently affected in autoimmune diseases, such as SLE, due to aberrant activations in both humoral and cellular immunity. For instance, in autoimmune diseases kidney is known to be the site of immune complex (an amalgam of antigens and antibodies) deposition and formation in these diseases, which activate complement-mediated recruitment of neutrophils and other myeloid and lymphoid cells, thus causing inflammation and tissue damage (Pisetsky, 2023). I performed Hematoxylin and eosin (H&E) stains on 4% PFA-fixed and paraffin-embedded kidneys from 12 months old mice from all four genotypes (**Fig 1.3**). These results showed that the glomeruli (kidney's filtering unit) in *C9orf72^{-/-}* mice and *Grn^{-/-};C9orf72^{-/-}* mice present with increased number of infiltrating immune cells as denoted by the smaller and darker nuclear stain present in both. Comparison between these two genotypes indicated that *Grn^{-/-};C9orf72^{-/-}* mice kidney had much more infiltrating immune cells compared to that seen in the kidneys of *C9orf72^{-/-}* mice. In addition, the *Grn^{-/-};C9orf72^{-/-}* mice have greater numbers of sclerotic glomeruli, which are commonly found in patients with lupus nephritis, compared to other genotypes. These results raised the hypothesis that, although the immune biomarkers such as the Ig's and the anti-dsDNA and anti-ANA antibody were comparable in *C9orf72^{-/-}*

^{-/-} and *Grn*^{-/-};*C9orf72*^{-/-} mice, the immune-mediated damages in targeted organs, such as the kidney, can be more prominent in *Grn*^{-/-};*C9orf72*^{-/-} mice. To test this hypothesis, we performed additional stains on the kidney, including the Toluidine Blue stain, which highlights nucleic acids and polysaccharides, thus making it ideal for staining the basement membrane and surrounding cells in the glomeruli. In both *C9orf72*^{-/-} and *Grn*^{-/-};*C9orf72*^{-/-} mice kidney, I detected more abundant toluidine blue-positive deposits in the glomeruli with *Grn*^{-/-};*C9orf72*^{-/-} kidney compared to those from *C9orf72*^{-/-} mice (**Fig 1.3**). Using transmission electron microscopy, I further validated the accumulation of proteinaceous debris accumulation and complete effacement of podocyte foot processes in the kidneys from *C9orf72*^{-/-} mice and even more severely in the kidneys from *Grn*^{-/-};*C9orf72*^{-/-} mice (**Fig 1.3**). Immunofluorescent confocal microscopy showed much more abundant IgG deposits in the glomeruli of *Grn*^{-/-};*C9orf72*^{-/-} kidney, than that in *C9orf72*^{-/-} kidney. Finally, IHC of the kidney for CD11c, a marker for monocytes, B cells, and dendritic cells are increased in the *Grn*^{-/-};*C9orf72*^{-/-} kidney glomeruli compared to that seen in the WT and single knockouts suggesting immune cell infiltration and subsequent damage caused to the kidney by them (**Fig 1.3**).

Discussion

To investigate the interaction of PGRN and *C9orf72*, I generated a cohort of WT, *Grn*^{-/-}, *C9orf72*^{-/-}, and *Grn*^{-/-};*C9orf72*^{-/-} mice and found that *Grn*^{-/-};*C9orf72*^{-/-} mice have a significantly shorter life span compared with WT, *Grn*^{-/-} and *C9orf72*^{-/-} mice (**Figure 1.1a**). Gross anatomical analysis shows splenomegaly and lymphadenopathy in both *C9orf72*^{-/-} and *Grn*^{-/-};*C9orf72*^{-/-} mice (**Figure 1.1d-g**). These findings support our hypothesis that the simultaneous loss of PGRN and *C9orf72* aggravates peripheral immune dysfunction, with

similar autoimmune disease-like phenotypes between *C9orf72*^{-/-} and *Grn*^{-/-};*C9orf72*^{-/-} mice,

To investigate the peripheral immune dysfunction, I performed ELISA for autoantibodies (**Figure 1.1b,c**), Igs, and complements which are known to be elevated in autoimmune diseases (**Figure 1.2**). Similar to our gross anatomical findings, I observe that *C9orf72*^{-/-} and *Grn*^{-/-};*C9orf72*^{-/-} mice have elevated levels of autoantibodies and Igs as early as 7 months old. Interestingly, levels of these circulating Igs in *C9orf72*^{-/-} mice are higher than that of *Grn*^{-/-};*C9orf72*^{-/-} mice. Given these findings, I investigated whether these antibodies target peripheral organs using histopathological analysis (**Figure 1.2**). My results provide definitive evidence supporting increased damage in the kidneys of *Grn*^{-/-};*C9orf72*^{-/-} mice, resulting in glomerulonephritis as shown by increased immune cell infiltration, increased proteinaceous deposits, loss of glomerular podocyte end-feet and increased IgG deposits, similar to that found in patients with end-stage renal failure caused by autoimmune dysfunction.

Together, these findings show that concurrent loss of PGRN and C9orf72 exacerbates peripheral immune dysfunction and targeted tissue damage in the kidney, which leads to early lethality seen in *Grn*^{-/-};*C9orf72*^{-/-} mice.

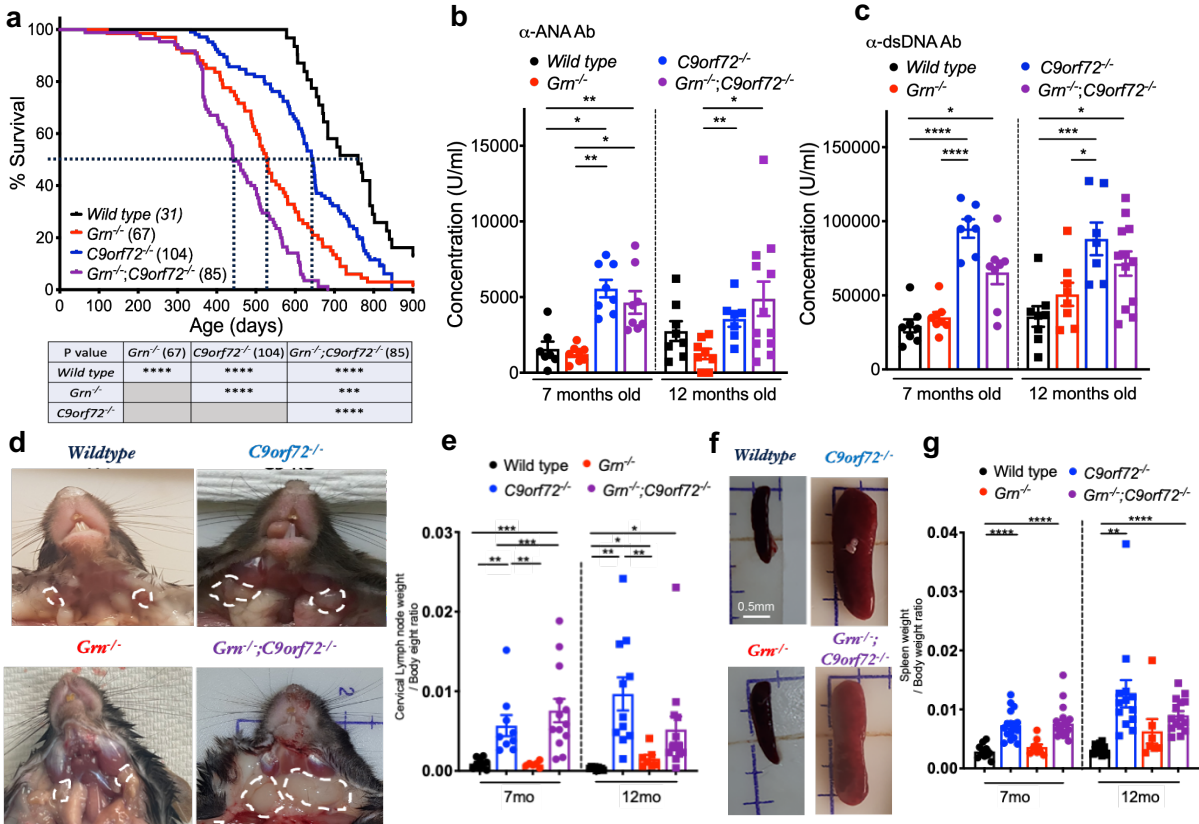


Figure 1.1. Increased peripheral immune dysfunction in *C9orf72*^{-/-} and *Grn*^{-/-};*C9orf72*^{-/-} mice.

(a) Kaplan-Meier curve for skin lesion onset and survival in WT, *Grn*^{-/-}, *C9orf72*^{-/-} and *Grn*^{-/-};*C9orf72*^{-/-} mice. * $p < 0.05$, **** $p < 0.001$, Long-rank (Mantel-Cox) test. (b-c) ELISA assays for antibodies against Anti-nuclear antigens (α -ANA) and double-stranded DNA (α -dsDNA) in 7 and 12 months old blood plasma from WT, *Grn*^{-/-}, *C9orf72*^{-/-} and *Grn*^{-/-};*C9orf72*^{-/-} mice ($n \geq 6$) * $p < 0.05$, *** $p < 0.001$, **** $p < 0.0001$, Student's unpaired t-test with Welch's correction. (d) Gross image of cervical lymphadenopathy in *C9orf72*^{-/-} and *Grn*^{-/-};*C9orf72*^{-/-} mice at 12 months of age (broken line). (e) Cervical lymph node weight to body weight ratio of WT, *Grn*^{-/-}, *C9orf72*^{-/-} and *Grn*^{-/-};*C9orf72*^{-/-} mice at 7 and 12 months of age ($n \geq 6$) * $p < 0.05$, ** $p < 0.01$, *** $p < 0.001$, **** $p < 0.0001$, one-way ANOVA with Tukey's multiple comparison test (f) Gross image of splenomegaly in *C9orf72*^{-/-} and *Grn*^{-/-};*C9orf72*^{-/-} mice at 12 months of age. (g) Spleen weight to body weight ratio of WT, *Grn*^{-/-}, *C9orf72*^{-/-} and *Grn*^{-/-};*C9orf72*^{-/-} mice at 7 and 12 months of age ($n \geq 6$) * $p < 0.05$, ** $p < 0.01$, *** $p < 0.001$, **** $p < 0.0001$, one-way analysis of variance (ANOVA) with Tukey's multiple comparison test.

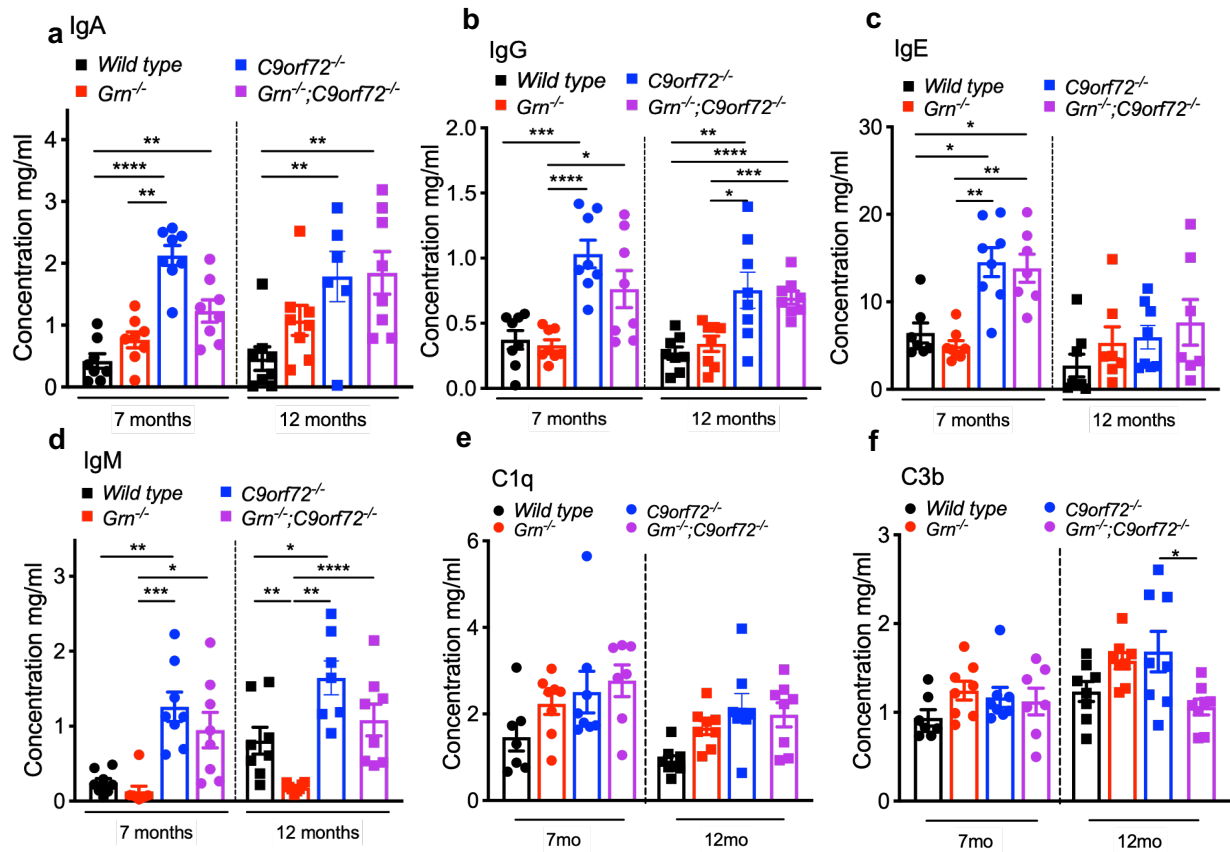


Figure 1.2. *C9orf72*^{-/-} and *Grn*^{-/-};*C9orf72*^{-/-} mice have elevated levels of immunoglobulins.

(a-e) ELISA assays for protein levels of Immunoglobulin-A (IgA), Immunoglobulin-G (IgG), Immunoglobulin-E (IgE), Immunoglobulin-M (IgM) and complements C1q and C3b in 7 and 12 months old blood plasma from WT, *Grn*^{-/-}, *C9orf72*^{-/-} and *Grn*^{-/-};*C9orf72*^{-/-} mice (n ≥ 6) * p < 0.05, *** p < 0.001, **** p < 0.0001, one-way ANOVA with Tukey's multiple comparison test.

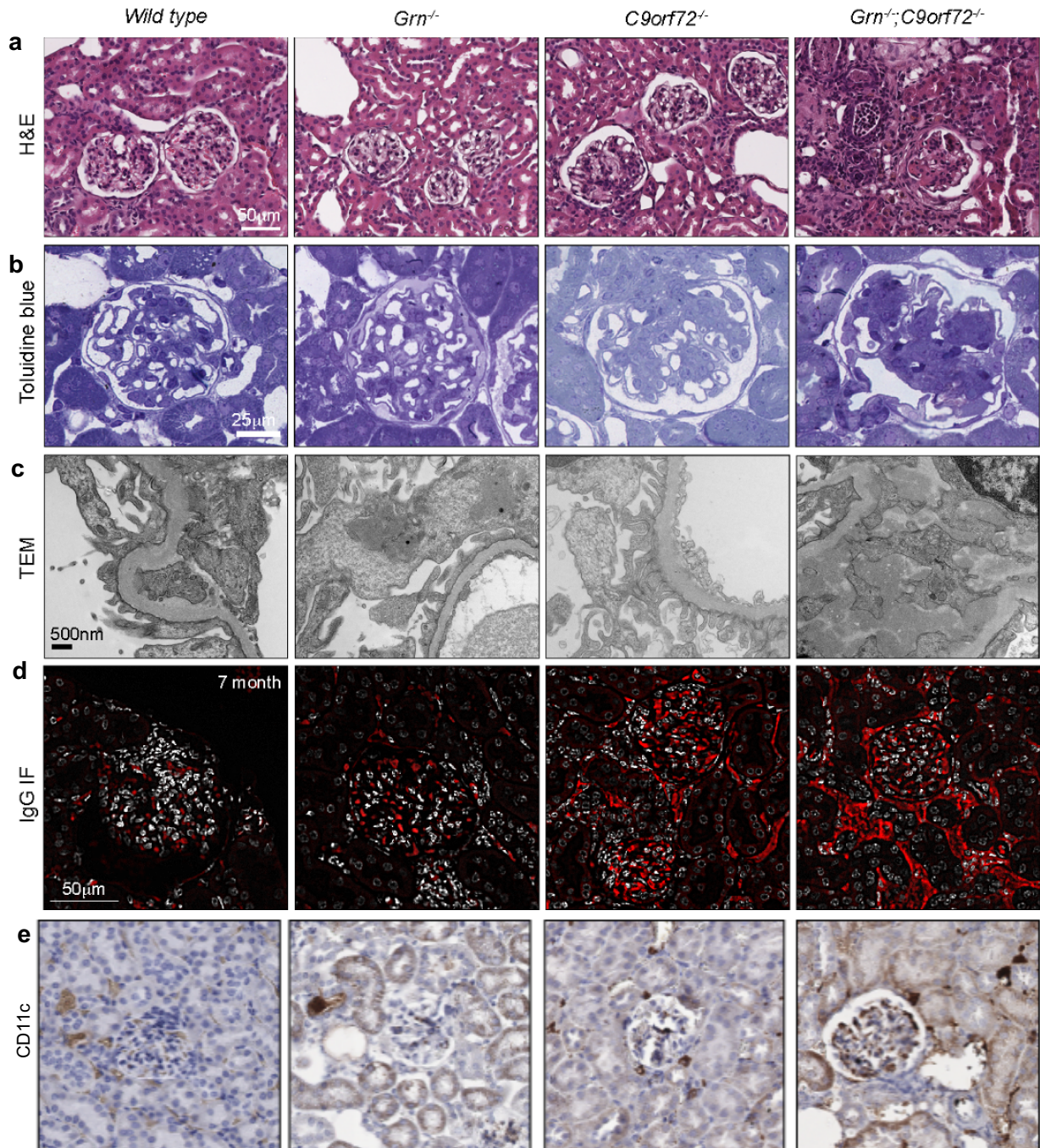


Figure 1.3. *C9orf72*^{-/-} and *Grn*^{-/-};*C9orf72*^{-/-} mice exhibit severe glomerulonephritis. (a) H&E stain (Scale Bar = 50µm), (b) Toluidine blue (Scale Bar = 25µm) and (c) Transmission electron microscopy (Scale Bar = 500µm) of *WT*, *Grn*^{-/-}, *C9orf72*^{-/-} and *Grn*^{-/-};*C9orf72*^{-/-} mice kidney at 12 months (d) IgG IF of *WT*, *Grn*^{-/-}, *C9orf72*^{-/-} and *Grn*^{-/-};*C9orf72*^{-/-} mice kidney at 7 months (Scale Bar = 50µm) (e) CD11c IHC of *WT*, *Grn*^{-/-}, *C9orf72*^{-/-} and *Grn*^{-/-};*C9orf72*^{-/-} mice kidney at 12 months (Scale Bar = 50µm)

Chapter 2

Neuropathological characterization of *Grn*^{-/-}, *C9orf72*^{-/-} and *Grn*^{-/-};*C9orf72*^{-/-} mice

Introduction

Neuroinflammation, characterized by the activation of the glial cells of the brain (microglia and astrocytes) and the release of pro-inflammatory mediators within the CNS is a hallmark of neurodegenerative diseases. Multiple lines of evidence support the importance of neuroinflammation in the onset and progression of neurodegenerative diseases such as AD, ALS, FTD, Parkinson's disease, and multiple sclerosis (Hashimoto et al., 2022; W. Zhang, Xiao, et al., 2023). In addition, there is mounting evidence of crosstalk between peripheral immune dysregulation and aging brain health, resulting in cooccurrences of autoimmune diseases in patients with neurodegenerative diseases (Bettcher et al., 2021; Hashimoto et al., 2022; Lashley et al., 2014). In the previous chapter, I provide evidence supporting the increased immune dysregulation in *Grn*^{-/-};*C9orf72*^{-/-} mice, supporting that the peripheral immune dysregulation in the aging process in these mice could contribute to neurodegeneration.

In this chapter, I investigate how loss-of-function in *Grn* and *C9orf72* genes impact the central nervous system. Our lab has previously shown that loss of PGRN in mice results in C1q-mediated synaptic pruning by activated microglia in the thalamus in an age-dependent manner. In addition, loss of PGRN causes age-dependent transcriptomic changes in microglia that result in a reduction in their homeostatic genes and up-regulation of genes involved in endolysosomal trafficking (Lui et al., 2016; J. Zhang et al., 2020). In a recent study, our lab also used snRNA-seq to compare the cell type-specific transcriptomic changes in the thalamus and frontal cortex from *Grn*^{-/-} mice and FTLN patients with *GRN* mutations. This approach reveals highly conserved transcriptomic changes in astrocytes with an increase in gene signatures for autophagy, glia-vascular

coupling, and positive regulation of cell death (Marsan et al., 2023). Studies from the Baloh group have shown that loss-of-function in *C9orf72* gene results in microglial activation with an increase in proinflammatory cytokine production such as type 1 interferons possibly due to reduction of *C9orf72* mediated STING pathway suppression, along with increased phagocytic capabilities (Lall et al., 2021; McCauley et al., 2020a; O'Rourke et al., 2016). In light of these results, I hypothesize that simultaneous loss of PGRN and *C9orf72* will exacerbate glial phenotypes in *Grn^{-/-};C9orf72^{-/-}* mice.

Results

Grn^{-/-};C9orf72^{-/-} mice have increased gliosis compared to that in Grn^{-/-} and C9orf72^{-/-} mice

Given the importance of neuroinflammation in neurodegenerative disease pathology, we investigated the changes in both microglial and astroglial density in both the anterior coronal section and midbrain coronal section containing the thalamus. Our lab has previously shown an increase in microgliosis in the thalamic region of the mouse brain as early as 7 months of age. To compare the difference in gliosis phenotype, I used immunohistochemistry for Iba-1 (microglial marker) and GFAP (reactive astrocyte marker). My results showed that at 12 months of age, *Grn^{-/-};C9orf72^{-/-}* mice have a more widespread increase in microgliosis compared to other genotypes (**Figure 2.1a**). Morphologically, *Grn^{-/-}* microglia had large cell bodies with a flattened appearance and thick and less complex processes (ameboid-like appearance) that extended larger areas. *Grn^{-/-};C9orf72^{-/-}* microglia were similar to those seen in *Grn^{-/-}* mice, although smaller and

aggregating together. Both *WT* and *C9orf72*^{-/-} brains had small cell bodies and ramified processes, as seen in homeostatic stages. Astrogliosis on the other hand follows a similar suite between *Grn*^{-/-};*C9orf72*^{-/-} mice and *Grn*^{-/-} mice, as they have greater numbers of GFAP+ astrocytes present in the thalamus and surrounding regions (**Figure 2.1d**). In contrast, *WT* and *C9orf72*^{-/-} brains showed no increase in reactive astrocytes in the thalamus and the neighboring regions compared to that in *Grn*^{-/-};*C9orf72*^{-/-} mice and *Grn*^{-/-} mice.

Using Stereo Investigator's volumetric analysis for quantification, I quantified the gliosis in three regions (thalamus, amygdala and the piriform cortex) due to overt microgliosis seen in these regions in the *Grn*^{-/-};*C9orf72*^{-/-} mice. I showed similar increase in microgliosis in the 7 months old thalamus in *Grn*^{-/-};*C9orf72*^{-/-} mice and *Grn*^{-/-} mice, whereas at 12 months of age, *Grn*^{-/-};*C9orf72*^{-/-} mice and *Grn*^{-/-} mice had increased microgliosis, although *Grn*^{-/-};*C9orf72*^{-/-} mice thalamus showed greater microglial cells per area compared to that in the *Grn*^{-/-} mice (**Figure 2.1b,c**). *WT* and *C9orf72*^{-/-} mice brains did not show significant age-related changes in microglia. In the 12 months amygdala and piriform cortex region, all genotypes have a slightly higher microgliosis compared to that in *WT*, although *Grn*^{-/-};*C9orf72*^{-/-} mice have the highest number of cells per area compared to other genotypes. Upon quantifying the astrocytes in these same regions, I found *Grn*^{-/-};*C9orf72*^{-/-} mice and *Grn*^{-/-} mice had greater number of astrocytes per area as early as 7 months of age with *Grn*^{-/-};*C9orf72*^{-/-} mice having greater number than that of *Grn*^{-/-} mice (**Figure 2.1e,f**). No difference was seen in the astrogliosis in *WT* and *C9orf72*^{-/-} mice at that age. At 12 months of age, although the number of astrocytes per area increases, the general trend between the genotypes remains the same.

In addition, I performed immunofluorescence (IF) staining using C1q, Iba1 and GFAP and found the *Grn*^{-/-};*C9orf72*^{-/-} mice and *Grn*^{-/-} thalamus at 12 months of age showed profound increase in C1q (red) positive stains colocalizing mostly with microglia (green), in addition to few GFAP+ (blue) cells (**Figure 2.2d**). Our lab's previous findings have shown that complement is involved in the microglia mediated synapse pruning. In addition, previous literature also suggests that cells of myeloid lineage (microglia) produce C1q (W. Zhang, Chen, et al., 2023). Thus the presence of C1q in predominantly Iba-1 cells in 12 months old *Grn*^{-/-};*C9orf72*^{-/-} mice and *Grn*^{-/-} thalamus proves that the aged microglia in the mice of these two genotypes have increased C1q production, with possible implications in microglial complement-mediated clearing via phagocytosis.

These findings suggest that as early as 7 months of age, *Grn*^{-/-};*C9orf72*^{-/-} mice and *Grn*^{-/-} mice showed an age-dependent increase in the glial accumulation in the thalamus. Although *C9orf72*^{-/-} brains show no overt gliosis histologically, *Grn*^{-/-};*C9orf72*^{-/-} brains show an increase in gliosis in regions previously not seen in the single knockout mice. Of note, these regions (thalamus, amygdala, and the entorhinal cortex) together form the limbic region, which is involved in emotion regulation and is strongly affected in patients with FTD. My IF stain further suggests that the microglia in the aged *Grn*^{-/-};*C9orf72*^{-/-} mice and *Grn*^{-/-} thalamus are reactive and primed for phagocytic clearing activity in a C1q mediated pathway. Thus, it shows that simultaneous knockout of the two genes unmasks previously unknown regions of vulnerability that are of importance to the disease pathology in humans.

Grn^{-/-};C9orf72^{-/-} mice have a more compromised blood brain barrier (BBB) compared to that in Grn^{-/-}, C9orf72^{-/-} mice

Our findings in the previous chapter and above section dictated our next set of experiments, where I investigated the presence of local inflammation and possible presence of immunoglobulins. To test my hypothesis, I performed a set of immunofluorescence stains in the mouse brain thalamus due to this region's consistent gliosis phenotype. To investigate the presence of immunoglobulins, I stained for IgG and co-stained with Iba-1 and GFAP in 12 months old mouse brain thalamus (**Figure 2.2c**). Although all genotypes have a basal level of IgG stain (red), the presence of IgG is significantly stronger in *Grn^{-/-};C9orf72^{-/-}* mice brain thalamus, with strong colocalization in Iba-1 positive cells. This was validated using Imaris software for 3D reconstruction and visualization of these stains (not shown). I also performed Immunogold EM for IgG on mice brain thalamus at 12 months of age and found an increase in the number of IgG positive particles in the brain parenchyma in all four genotypes, with *Grn^{-/-};C9orf72^{-/-}* brain thalamus having the highest number of IgG gold particles per area (**Figure 2.3a,d**). These findings raised the question of the source of IgG either from within the CNS or from peripheral sources. Given our findings from Chapter 1, along with recent findings of the presence of peripheral immune T-cells in AD patients CSF and mouse models (X. Chen et al., 2023; Gate et al., 2020; Merlini et al., 2018), the odds of the IgG entering the CNS from the periphery are much higher. To test this hypothesis, first I stained for Integrin beta-2 (ITGB2), a known marker for cell adhesion and phagocytosis, and antigen presentation and processing in immune cells) Iba-1 and fibrinogen (FGG) (a blood protein known as a marker for local inflammation in the brain) in 12 months old thalamus (**Figure**

2.2b). I showed an increase in FGG (blue) in all the knockout mice along the blood vessels, although particularly strongly expressed in *C9orf72*^{-/-} mice thalamus. Interestingly, the proportion of ITGB2+ (green) cells significantly increased along the FGG positive blood vessels in *Grn*^{-/-};*C9orf72*^{-/-} mice and *Grn*^{-/-} mice brain thalamus. These cells are almost all Iba-1 positive (red) suggesting both local inflammation, a possible blood-brain barrier disruption, and microglial phagocytic activity around the region of inflammation. Although *C9orf72*^{-/-} mice blood vessels had a strong presence of fibrinogen, ITGB2+ Iba-1+ cells were markedly less than that of *Grn*^{-/-};*C9orf72*^{-/-} mice and *Grn*^{-/-} mice brains.

Another finding of note, is that the FGG stain along the blood vessels of *Grn*^{-/-};*C9orf72*^{-/-} mice and *Grn*^{-/-} brain thalamus are more fragmented and colocalized with microglia, suggesting possible BBB disruption. To test this hypothesis, I performed 40kDA sized Fluorescein (FITC) Dextran dye (Thermo Fisher, D1845) intravenous injection in 4-, 7- and 12-month-old animals and fixed the brains without perfusion. Upon staining these brains with Iba-1 and GFAP, I showed that the BBB is severely compromised in 12 months old *Grn*^{-/-};*C9orf72*^{-/-} mice and *Grn*^{-/-} mice brains, more so in the *Grn*^{-/-};*C9orf72*^{-/-} mice. This is denoted by the loss of “train track” like blood vessel structures in these animals and replaced by smaller green fragmented vessels that are taken up by the glial cells. Imaris 3D reconstruction allowed us to show that these dextran positive targets are colocalized with blue Iba-1 positive cells mostly (**Figure 2.2b**). In addition, Immunogold EM for ITGB2 and GFAP further validated my finding, where I saw a decrease in the presence of GFAP around the blood vessels in *Grn*^{-/-};*C9orf72*^{-/-} mice and *Grn*^{-/-} mice brains compared to that in *WT* and *C9orf72*^{-/-} thalamus, with *WT* having the most number of GFAP+ gold particles

around the blood vessels (**Figure 2.3c**). ITGB2 particles stayed similar among the four different genotypes (**Figure 2.3b**). Given astrocytes are involved in the BBB integrity, lack of GFAP+ particles around the blood vessels indicated possible disruption in the BBB at 12 months of age in *Grn*^{-/-};*C9orf72*^{-/-} mice and *Grn*^{-/-} mice thalamus. At 7 and 4 months old, we do not observe noticeable changes in the BBB architecture (not shown).

These findings make a case for a peripheral immune interaction with the CNS aggravating the neuro-immune phenotypes in the *Grn*^{-/-};*C9orf72*^{-/-} mice and *Grn*^{-/-} mice thalamus

Grn and *C9orf72* have opposing functions in the excitatory neuronal population in the limbic region

Our lab has previously established that in addition to increased gliosis in *Grn*^{-/-};*C9orf72*^{-/-} and *Grn*^{-/-} mice brains, there is an increased presence of peripheral immune components such as IgG in the brain parenchyma via BBB disruption in the thalamus. To compare the changes in neuronal composition in these mice due to double mutation in the genes and subsequent inflammatory phenotypes in the brain parenchyma, I quantified the number of neurons in the thalamus at 12 months of age. Given that the gliosis phenotype was not prominent at 7 months of age, along with our lab previously showing microglial reactivity being the possible initiator of neurodegenerative phenotype seen in the *Grn*^{-/-} mice, I quantified the total number of NeuN+ neurons in the thalamus at 12 months of age using Stereo Investigator's volumetric analysis. I find a reduction in neurons in the thalamus of *Grn*^{-/-};*C9orf72*^{-/-} and *Grn*^{-/-} mice. *C9orf72*^{-/-} mice, although showed a trend in reduced presence of NeuN+ neurons in the thalamus, their

quantification showed animal to animal variability and thus was not significant (**Figure 2.4a,b**). Closer inspection of the NeuN+ neuronal nuclei in the thalamus shows irregular, and expanded “popcorn like appearance” cell body in 12 months old *Grn*^{-/-};*C9orf72*^{-/-} and *C9orf72*^{-/-} mice as denoted by the white arrows. We were interested in knowing whether the reduction in neuronal numbers in the *Grn*^{-/-};*C9orf72*^{-/-} and *Grn*^{-/-} mice thalamus were of excitatory origin and thus stained for protein kinase-C delta (Pkcδ), a marker for a subset of excitatory neurons from the thalamus found in our previous study to be reduced with age in *Grn*^{-/-} mice (J. Zhang et al., 2020). Interestingly, Pkcδ is also expressed in microglia and astrocytes according to the Barres RNA seq website, suggesting in *Grn*^{-/-} mice the expression of Pkcδ reduces overall with age in the thalamus. I performed similar thalamic quantification in all four genotypes at 7 and 12 months of age, and have found that only in *Grn*^{-/-} mice do we see an age-dependent reduction of Pkcδ positive cells in the thalamus region of the brain (**Figure 2.5a,b**). Interestingly, I observe an increase in the Pkcδ+ thalamo-cortical projections in the barrel cortex region, and Pkcδ+ neurons in the hippocampal dentate gyrus and amygdala in the *Grn*^{-/-};*C9orf72*^{-/-} and *C9orf72*^{-/-} mice. Given that dysregulation of Pkcδ signaling has been implicated in both cancer and neurodegeneration such as AD (Lorden et al., 2021), our running hypothesis is that there is a possible increase in the proportion of excitatory neurons in similar brain regions. To test this, I performed vesicular glutamate transporter-2 (VGlut-2) (a marker for excitatory presynaptic terminal) IHC on 12 months of age animals and have noted an increase in the intensity of VGlut-2 in the thalamus and the barrel cortex of *Grn*^{-/-};*C9orf72*^{-/-} and *C9orf72*^{-/-} mice at 12 months of age (**Figure 2.4c**). These findings suggest a possibility of greater number of excitatory neurons forming increased number of presynaptic terminals

in the limbic regions in *Grn*^{-/-};*C9orf72*^{-/-} and *C9orf72*^{-/-} mice, independent of the neuroimmune phenotype conferred due to the reduced expression of C9orf72 protein. Hence loss of function of Grn in mice brain results in reduction in a subset of excitatory neurons in the limbic region, which can be rescued via reduced C9orf72 protein expression.

Knockout mice have mislocalization of nuclear proteins

One of the common features of neurodegenerative diseases is the mislocalization of nuclear proteins such as TDP-43 and the disruption of the nuclear pore complexes (NPC) that are embedded in the nuclear membrane and are involved in the nuclear-cytoplasmic transport and its selective permeability (Dickinson et al., 2022; Nag and Tripathi, 2023). NPCs are made up of around 30 nucleoporins (NUP)s, of which Nup98 is essential for the NPCs' barrier maintenance activity. Nup98 mislocalization is a common feature in tauopathies such as AD and is associated with tau accumulation and neurotoxicity (Nag and Tripathi, 2023). In addition to that, our lab has shown that mislocalization of TDP-43 and Nup98 are features present in 12 months old *Grn*^{-/-} mice.

To test for possible neurodegenerative phenotypes, I performed IF stain for 12 months old mice brain thalamus using the markers Nup98 (red), Lamin-B1 (marker for nuclear membrane) (green) and Map-2 (blue) (**Figure 2.6a**). I validated our lab's previous findings of Nup98 increase and extension into the neuronal cytoplasm in *Grn*^{-/-} mice at 12 months of age. In addition to that, I find that increased presence of Nup98 in *Grn*^{-/-};*C9orf72*^{-/-} and *C9orf72*^{-/-} mice thalamus at 12 months, with *Grn*^{-/-};*C9orf72*^{-/-} mice having the most prevalent amount and mislocalization of Nup98 into the neuronal cytoplasm. I

also performed IHC for TDP-43 and found similar mislocalization of TDP-43 in all three genotypes in their thalamus at 12 months of age, with greater presence of diffused TDP-43 in the cytoplasm of *Grn*^{-/-};*C9orf72*^{-/-} and *C9orf72*^{-/-} mice (**Figure 2.6b**). These findings indicate that all three of our knockout mice models have the common signatures of neurodegeneration.

Grn^{-/-};*C9orf72*^{-/-} mice show an age dependent increase in inflammation and B-cell receptor signaling

To augment our histological findings with transcriptional changes in these mice, I performed bulk transcriptomics in both 7- and 12-months old mice hemi sections. Topmost differentially expressed genes (DEG) were obtained with the help of UCSF Colabs and our in-house bioinformatician Dr. Rufei Lu. Using age as a covariate, these DEGs were organized into pathways that change with age and a heatmap was generated (**Figure 2.7**). In the mice brain, we only see age-dependent increase in pathways involving lysosome (*Ctsb*, *Ctsd*, *Lamp1*, *Lamp2*, *Npc2*, *Cd68*, *Hexb*), phagosome (*Rab7b*, *Clec7a*, *Lamp1*, *Lamp2*, *Tlr2*, *Fcgr2b*), B-cell receptor signaling pathway (*Cd22*, *Fcgr2b*, *Cd19*, *CD81*) and complement pathway (*C1qa*, *C1qb*, *C1qc*, *C3ar1*, *C4b*) in *Grn*^{-/-};*C9orf72*^{-/-} and *Grn*^{-/-} mice, with *Grn*^{-/-};*C9orf72*^{-/-} mice having greater expression increase of genes in our pathways of interest.

While we expected the lysosomal, phagosomal, and complement pathways to come up and subsequently increase with age in our analysis, we were surprised by the gene expression module of the B-cell signaling pathway. With our data from chapter 2.2 suggesting compromised BBB and IgG expression in the parenchyma, we hypothesize

IgG from the periphery that enter the brain parenchyma are interacting with the glial cells, thereby possibly stimulating the expression of their genes that result in antigen presentation.

Grn^{-/-};C9orf72^{-/-} mice have increased immune activation, blood vessel morphogenesis and regulation-related gene signatures in non-neuronal cells.

In light of our histopathological characterization of the brain and bulk transcriptomic data indicating gliosis and blood-brain barrier breakdown as key factors that could potentially be the cause of the neuroimmune and neurodegeneration phenotypes we see in both the single and more so in the double knockout animals, I performed snRNA-seq of the thalamus of 12 months old mice brain in all four genotypes. With the help of UCSF Colabs bioinformatics core, Jennifer Choi, and Dr. Rufe Lu, we were able to identify and visualize different clusters of cells that were affected by the single and double knockouts using the Seurat bioinformatics pipeline.

Similar to our Pkc δ results in chapter 2.3, the UMAP generated from this pipeline shows a reduced number of cells corresponding to clusters 1,2, and 3, denoting separate excitatory clusters in *Grn^{-/-}* mice thalamus only (**Figure 2.8a**). Interestingly, the thalamus in all three knockout mice had the presence of cluster number 6, which we have denoted as unclassified neurons. More work is in progress to understand the changes in different neuronal clusters.

Clusters 12, 13 and 14 corresponding to microglia, astrocytes, and endothelial cells respectively have been characterized more in-depth. Upon comparing the microglial cluster (12) between the genotypes, the *Grn^{-/-};C9orf72^{-/-}* mice have an increased number

of microglia in their thalamus as shown by the UMAP compared to the other genotypes. Upon comparing the microglial cluster DEGs between all three genotypes, we observe greater overlap between *Grn*^{-/-};*C9orf72*^{-/-} and *Grn*^{-/-} mice, with a greater increase in pathways in *Grn*^{-/-};*C9orf72*^{-/-} that correspond to “Response to wounding”, “Regulation of immune system process” and “Lipoprotein metabolic process” compared to that seen in *Grn*^{-/-} mice (**Figure 2.8b-d**). Interestingly, *Grn*^{-/-};*C9orf72*^{-/-} microglial clusters have some unique signatures that are absent in the single knockout microglial clusters, some of which are “Extracellular vesicle biogenesis”, “Autophagy” and “Antigen presentation and processing” to name a few (**Figure 2.8c,d**). These findings further confirm that the microglial cluster found in *Grn*^{-/-};*C9orf72*^{-/-} mice thalamus are involved in antigen presentation and processing such as peripheral IgG.

Upon comparing the DEGs of the astrocyte clusters of the four genotypes, we see that both *Grn*^{-/-};*C9orf72*^{-/-} and *Grn*^{-/-} mice have gene signatures that are involved with blood vessel integrity and immune response, *Grn*^{-/-};*C9orf72*^{-/-} have a more pronounced gene signature for “Blood vessel morphogenesis” and “Response to immune system process” compared to the similar gene signatures seen in *Grn*^{-/-} mice such as “Vasodilation” and “Humoral immune response” (**Figure 2.8a,c**). This, in addition to the Immunogold GFAP findings from chapter 2.2 with reduced reactive astrocytic coverage around the blood vessel in *Grn*^{-/-};*C9orf72*^{-/-} and *Grn*^{-/-} mice confirms the loss of BBB integrity in these 2 mice brain thalamus at 12 months old, more so in the *Grn*^{-/-};*C9orf72*^{-/-} mice.

DEGs of endothelial cluster show gene signatures for reduced cell-cell adhesion, and increased regulation of vascular permeability in *Grn*^{-/-};*C9orf72*^{-/-} mice, further

confirming our histological findings of Dextran dye leakage from the blood vessels and uptake by microglial cells due to loss of BBB integrity in Chapter 2.2 (**Figure 2.8b,d**). Using Col4a1(basement membrane marker) in red, Iba-1 (blue) and Dextran dye (Green) to compare the BBB integrity in thalamus of 7 and 12 months old animals, we find that *Grn^{-/-};C9orf72^{-/-}* and *Grn^{-/-}* mice as early as 7 months show signs of BBB basement membrane fragmentations which aggravates with age, albeit to a greater extent in *Grn^{-/-};C9orf72^{-/-}* mice (**Figure 2.8e**).

Discussion

Neuropathological analysis of the four genotypes involved immunohistochemical and transcriptomic investigation of mice brains at 7 and 12 months old. I find increased microgliosis and astrogliosis in the thalamus of *Grn^{-/-};C9orf72^{-/-}* and *Grn^{-/-}* mice as early as 7 months old which increases with age (**Figure 2.1, 2.2**). Interestingly in *Grn^{-/-};C9orf72^{-/-}* I observe microgliosis in other limbic regions such as the amygdala and piriform cortex, starting from 7 months old which is not observed in the other two knockouts (not shown). Astrogliosis in *Grn^{-/-};C9orf72^{-/-}* and *Grn^{-/-}* mice spreads to the other limbic regions at 12 months of age. In addition, I performed IHC for Fcεr1a (a cell surface scavenger receptor marker involved in the clearance activity of myeloid and dendritic cells) (Chou et al., 2023), and found an increase in its expression in microglia-like cells in the thalamus of *Grn^{-/-};C9orf72^{-/-}* and *Grn^{-/-}* mice, in addition to its increased expression in amygdala and piriform cortex in *Grn^{-/-};C9orf72^{-/-}* mice at 12 months old (**Figure 2.1g**). These findings suggest that simultaneous loss of PGRN and C9orf72 protein unmask additional microglial activation characteristics in brain regions relevant to FTD pathogenesis in mice models as early as 7 months of age.

snRNA sequencing of mice brain thalamus suggest activation of inflammatory pathways and antigen presentation pathways in microglia, immune system activation and blood vessel morphogenesis pathways in astrocytes and disruption of cell adhesion in blood vessel endothelial cells, in *Grn*^{-/-};*C9orf72*^{-/-} suggesting disruption of BBB and activation of glial cells (**Figure 2.8, 2.9**). Bulk transcriptomics of 7 and 12 months old mice brains show an age-dependent increase in inflammatory, pathways involving lysosome, phagosome, complement cascade, and B-cell receptor signaling pathways in *Grn*^{-/-};*C9orf72*^{-/-} and *Grn*^{-/-} mice, albeit to a greater extent in *Grn*^{-/-};*C9orf72*^{-/-} mice further hinting towards BBB disruption and possible Ig entrance into the brain parenchyma in *Grn*^{-/-};*C9orf72*^{-/-} mice (**Figure 2.7**). Using 40 kDa FITC dextran dye injection in 4-, 7-, and 12-months old mice and Immunogold EM imaging, I show that *Grn*^{-/-};*C9orf72*^{-/-} and *Grn*^{-/-} mice have increased BBB disruption, via fragmented blood vessels in the thalamus (**Figure 2.9g**), the increased presence of IGTB2 (phagocytic cell surface marker found in microglia) around the blood vessels in *Grn*^{-/-};*C9orf72*^{-/-} and *Grn*^{-/-} mice and increased dye leakage from the blood vessels increased dye uptake by microglia (**Figure 2.2**), with *Grn*^{-/-};*C9orf72*^{-/-} mice having greater BBB fragmentation than that of *Grn*^{-/-} mice.

I observed greater neuron loss of excitatory origin at 12 months old thalamus in *Grn*^{-/-} mice compared to other genotypes, in addition to the increased thalamo-cortical projection of Pkcδ⁺ neurons in *Grn*^{-/-};*C9orf72*^{-/-} and *C9orf72*^{-/-} brains at 12 months old, suggesting loss of PGRN results in increased neuron loss that is rescued by the reduction in *C9orf72* protein (**Figure 2.4, 2.5**). Interestingly, upon comparing mislocalization of nuclear pore proteins (a possible indicator of neurotoxicity and neurodegeneration) in the thalamus among the four genotypes, I observe greater presence and mislocalization of

NUP98 in *Grn*^{-/-};*C9orf72*^{-/-} neuronal cytoplasm followed by that of *C9orf72*^{-/-} and *Grn*^{-/-} (**Figure 2.6**). These suggest that although reduced C9orf72 protein activity does not immediately result in neuronal death, it results in changes in neuronal protein composition that can result in neurodegenerative phenotypes in the future.

Taken together, loss of function in PGRN protein imparts a greater portion of inflammatory activation gene signatures seen in the non-neuronal cells of double knockout mice. In, addition, the loss of function of C9orf72 protein results in reduced neuronal cell death observed in *Grn*^{-/-} thalamus, although all three knockout mice have underlying accumulation and mislocalization of nuclear pore complexes, suggesting changes occurring in the regular function of the existing neurons. These neuronal and glial findings point towards the changes in neural circuitry seen in both mice and patients, although more functional circuitry characterization needs to be done to address this.

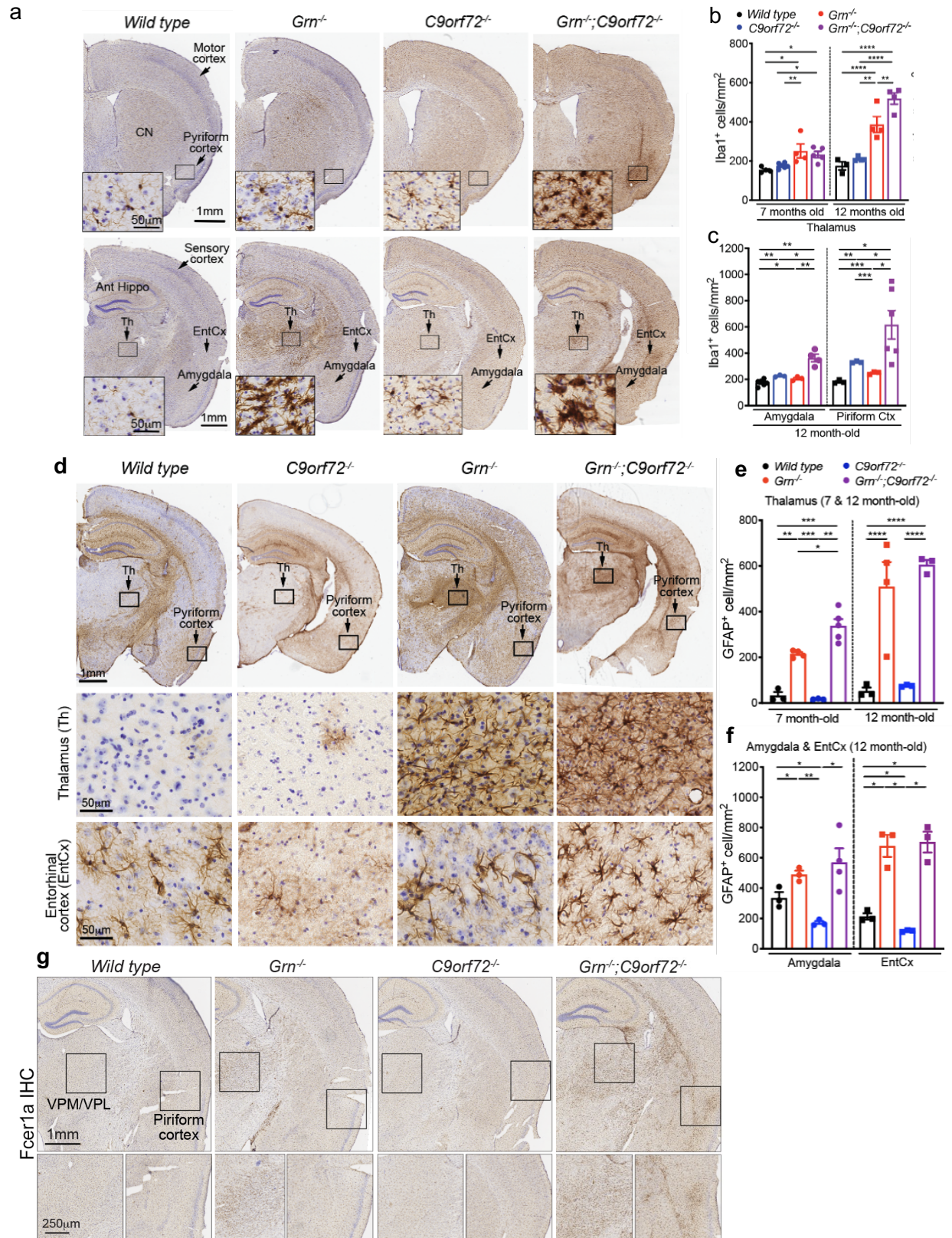


Figure 2.1. *Grn*^{-/-};*C9orf72*^{-/-} mice have increased gliosis compared to that in *Grn*^{-/-}, *C9orf72*^{-/-} mice (Figure caption continued on the next page.)

(Figure caption continued from the previous page.) **(a)** Iba-1 IHC of *WT*, *Grn*^{-/-}, *C9orf72*^{-/-} and *Grn*^{-/-};*C9orf72*^{-/-} mice at 12 months (Scale Bar = 50μm inset, Scale bar = 1mm hemibrain) **(b)** Thalamic quantification of Iba-1+ cells per area in *WT*, *Grn*^{-/-}, *C9orf72*^{-/-} and *Grn*^{-/-};*C9orf72*^{-/-} mice at 7 and 12 months (n≥4), * *p* < 0.05, ** *p* < 0.01, *** *p* < 0.001, **** *p* < 0.0001, one-way analysis of variance (ANOVA) with Tukey's multiple comparison test **(c)** Amygdala and Piriform cortex Iba-1+ cells per area in *WT*, *Grn*^{-/-}, *C9orf72*^{-/-} and *Grn*^{-/-};*C9orf72*^{-/-} mice at 12 months (n≥4), * *p* < 0.05, ** *p* < 0.01, *** *p* < 0.001, **** *p* < 0.0001, one-way analysis of variance (ANOVA) **(d)** GFAP IHC of *WT*, *Grn*^{-/-}, *C9orf72*^{-/-} and *Grn*^{-/-};*C9orf72*^{-/-} mice at 12 months (Scale Bar = 50μm inset, Scale bar = 1mm hemibrain) **(e)** Thalamic quantification of GFAP+ cells per area in *WT*, *Grn*^{-/-}, *C9orf72*^{-/-} and *Grn*^{-/-};*C9orf72*^{-/-} mice at 7 and 12 months (n≥4), * *p* < 0.05, ** *p* < 0.01, *** *p* < 0.001, **** *p* < 0.0001, one-way analysis of variance (ANOVA) with Tukey's multiple comparison test **(f)** Amygdala and Piriform cortex GFAP+ cells per area in *WT*, *Grn*^{-/-}, *C9orf72*^{-/-} and *Grn*^{-/-};*C9orf72*^{-/-} mice at 12 months (n≥4), * *p* < 0.05, ** *p* < 0.01, *** *p* < 0.001, **** *p* < 0.0001, one-way analysis of variance (ANOVA) **(g)** Fcεr1a HC of *WT*, *Grn*^{-/-}, *C9orf72*^{-/-} and *Grn*^{-/-};*C9orf72*^{-/-} mice at 12 months (Scale Bar = 250μm inset, Scale bar = 1mm hemibrain)

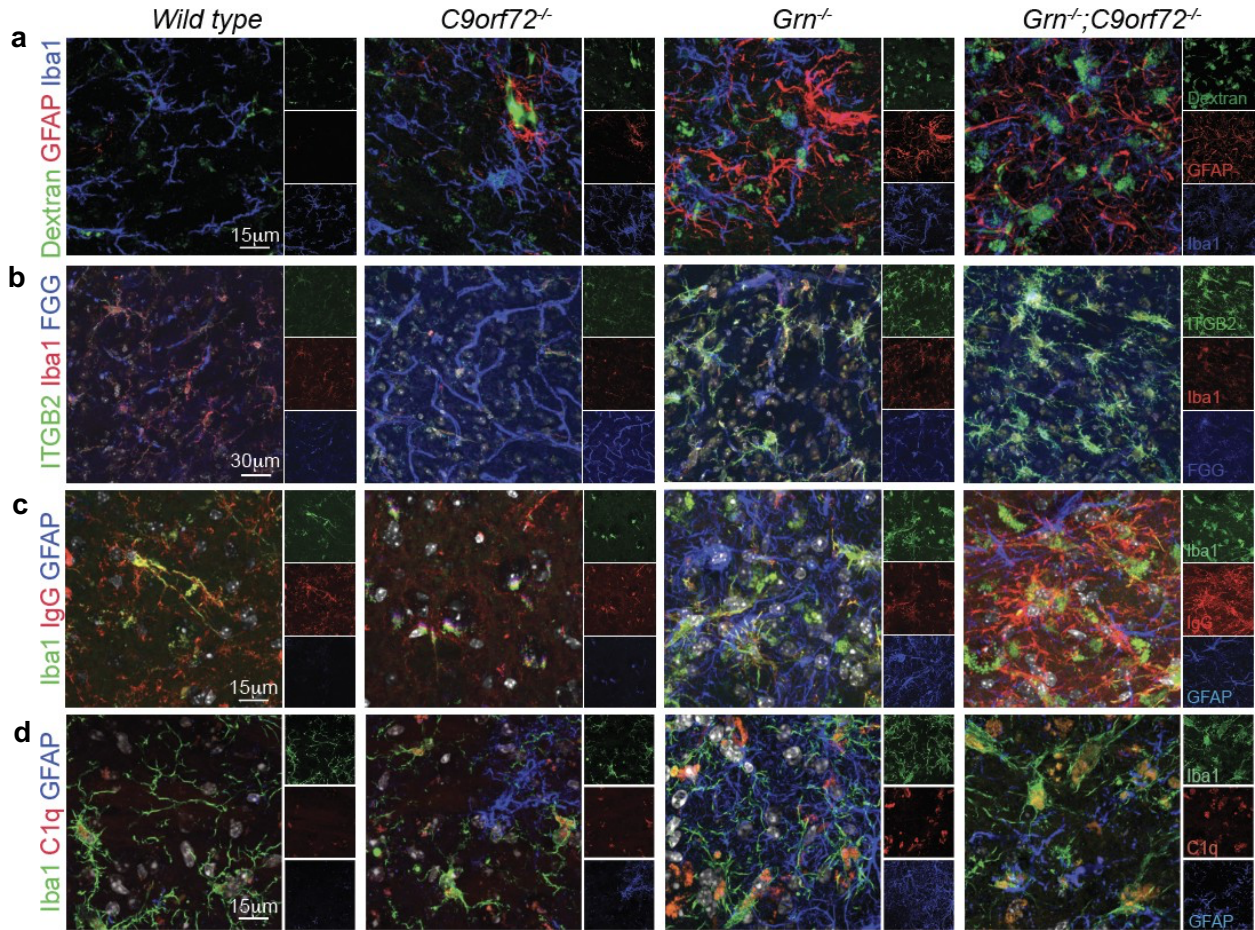


Figure 2.2. *Grn*^{-/-};*C9orf72*^{-/-} and *Grn*^{-/-} mice have compromised blood brain barrier (BBB) and inflammatory markers

(a) Dextran 40kDA (green) Iba-1(blue) and GFAP (red) IF of *WT*, *Grn*^{-/-}, *C9orf72*^{-/-} and *Grn*;*C9orf72*^{-/-} mice brain thalamus at 12 months (Scale bar = 15 μm) **(b)** ITGB2 (green) FGG (blue) and Iba-1 (red) IF of *WT*, *Grn*^{-/-}, *C9orf72*^{-/-} and *Grn*^{-/-};*C9orf72*^{-/-} mice brain thalamus at 12 months (Scale bar = 30 μm) **(c)** Iba-1 (green) GFAP(blue) and IgG (red) IF of *WT*, *Grn*^{-/-}, *C9orf72*^{-/-} and *Grn*;*C9orf72*^{-/-} mice brain thalamus at 12 months (Scale bar = 15 μm) **(d)** Iba-1 (green) GFAP(blue) and C1q (red) IF of *WT*, *Grn*^{-/-}, *C9orf72*^{-/-} and *Grn*^{-/-};*C9orf72*^{-/-} mice brain thalamus at 12 months (Scale bar = 15 μm)

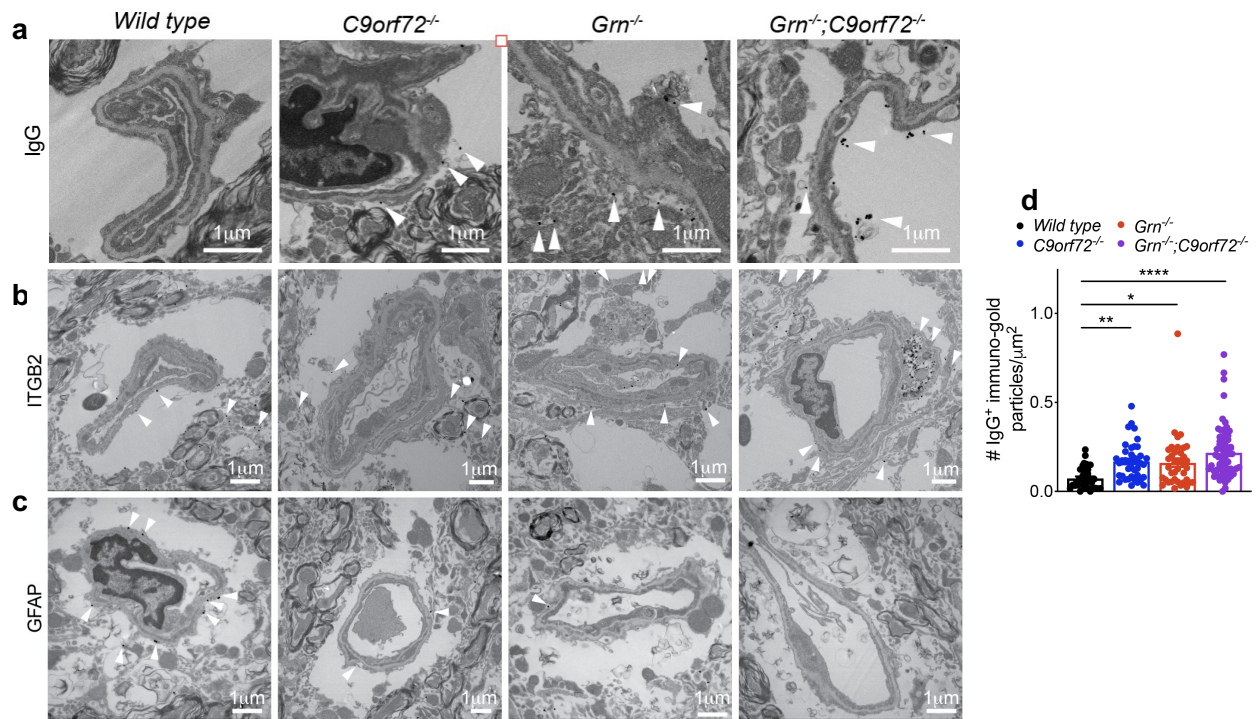


Figure 2.3. *Grn*^{-/-};*C9orf72*^{-/-} mice have a more compromised blood brain barrier (BBB) compared to that in *Grn*^{-/-}, *C9orf72*^{-/-} mice
 ImmunoGold EM for (a) IgG (b) ITGB2 and (c) GFAP of WT, *Grn*^{-/-}, *C9orf72*^{-/-} and *Grn*^{-/-};*C9orf72*^{-/-} mice brain thalamus at 12 months (Scale bar = 1 μm) (d) IgG gold particle quantification in the brain parenchyma in the thalamus of WT, *Grn*^{-/-}, *C9orf72*^{-/-} and *Grn*^{-/-};*C9orf72*^{-/-} mice at 12 months (n=2, ≥10 image per n), * $p < 0.05$, ** $p < 0.01$, *** $p < 0.001$, **** $p < 0.0001$, one-way analysis of variance (ANOVA) with Tukey's multiple comparison test

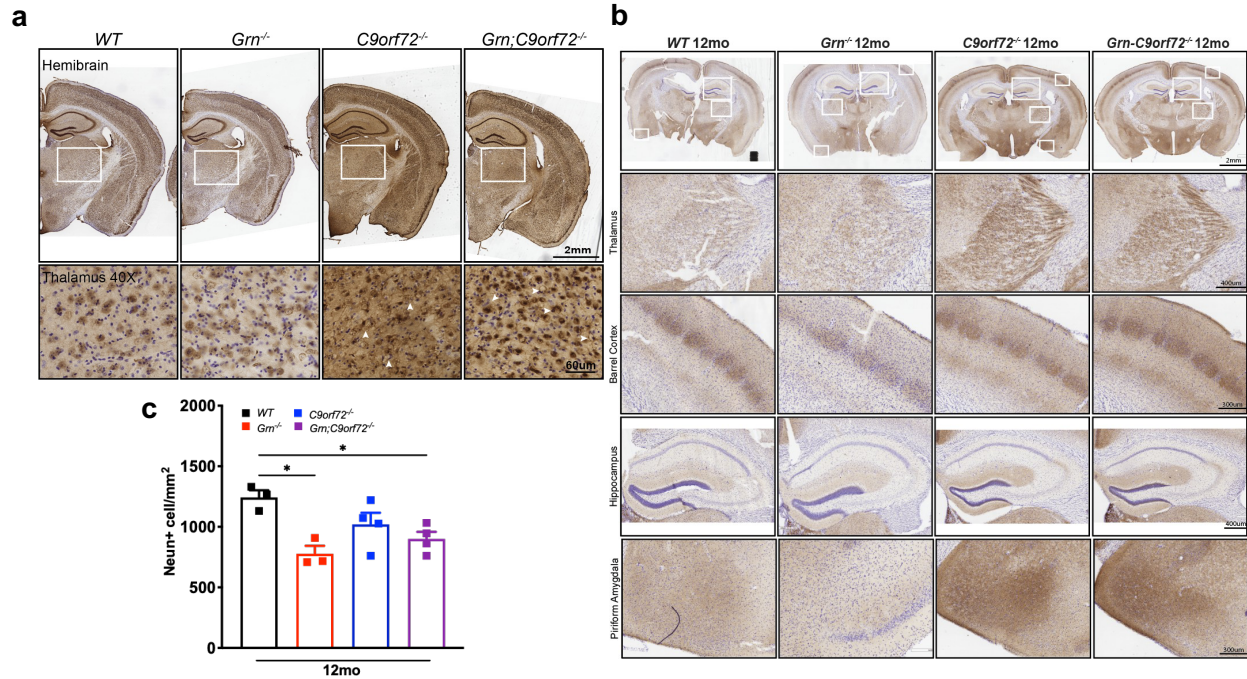


Figure 2.4. Thalamic neuronal loss in 12 months *Grn*^{-/-}, *C9orf72*^{-/-} and *Grn*^{-/-};*C9orf72*^{-/-} mice brain thalamus

(a) Neun IHC of *WT*, *Grn*^{-/-}, *C9orf72*^{-/-} and *Grn*^{-/-};*C9orf72*^{-/-} mice at 12 months (Scale Bar = 50µm inset, Scale bar = 2mm hemibrain) (b) Neun quantification in the thalamus of *WT*, *Grn*^{-/-}, *C9orf72*^{-/-} and *Grn*^{-/-};*C9orf72*^{-/-} mice at 12 months (n ≥3 image per n), * *p* < 0.05, ** *p* < 0.01, *** *p* < 0.001, **** *p* < 0.0001, one-way analysis of variance (ANOVA) with Tukey's multiple comparison test (c) Neun IHC of *WT*, *Grn*^{-/-}, *C9orf72*^{-/-} and *Grn*^{-/-};*C9orf72*^{-/-} mice at 12 months (Scale Bar = 400µm inset Scale bar = 300µm inset, Scale bar = 2mm hemibrain)

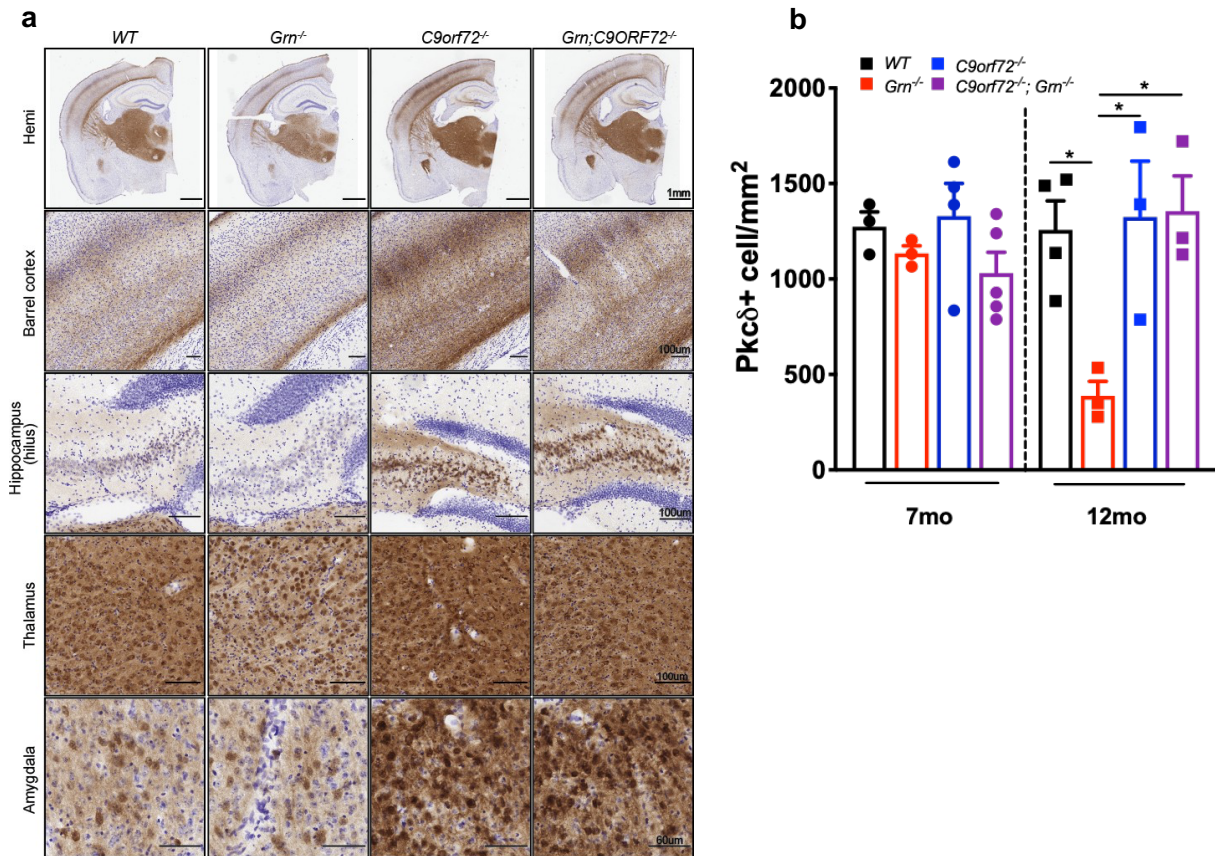


Figure 2.5. Distribution of Pkcδ⁺ neurons in 12 months old brain of all four genotypes.

(a) Pkcδ IHC of *WT*, *Grn*^{-/-}, *C9orf72*^{-/-} and *Grn*^{-/-};*C9orf72*^{-/-} mice at 12 months (Scale Bar = 100µm, inset, Scale Bar = 50µm inset, Scale bar = 2mm hemibrain) **(b)** Pkcδ quantification in the thalamus of *WT*, *Grn*^{-/-}, *C9orf72*^{-/-} and *Grn*^{-/-};*C9orf72*^{-/-} mice at 12 months (n ≥ 3 image per n), * *p* < 0.05, ** *p* < 0.01, *** *p* < 0.001, **** *p* < 0.0001, one-way analysis of variance (ANOVA) with Tukey's multiple comparison test

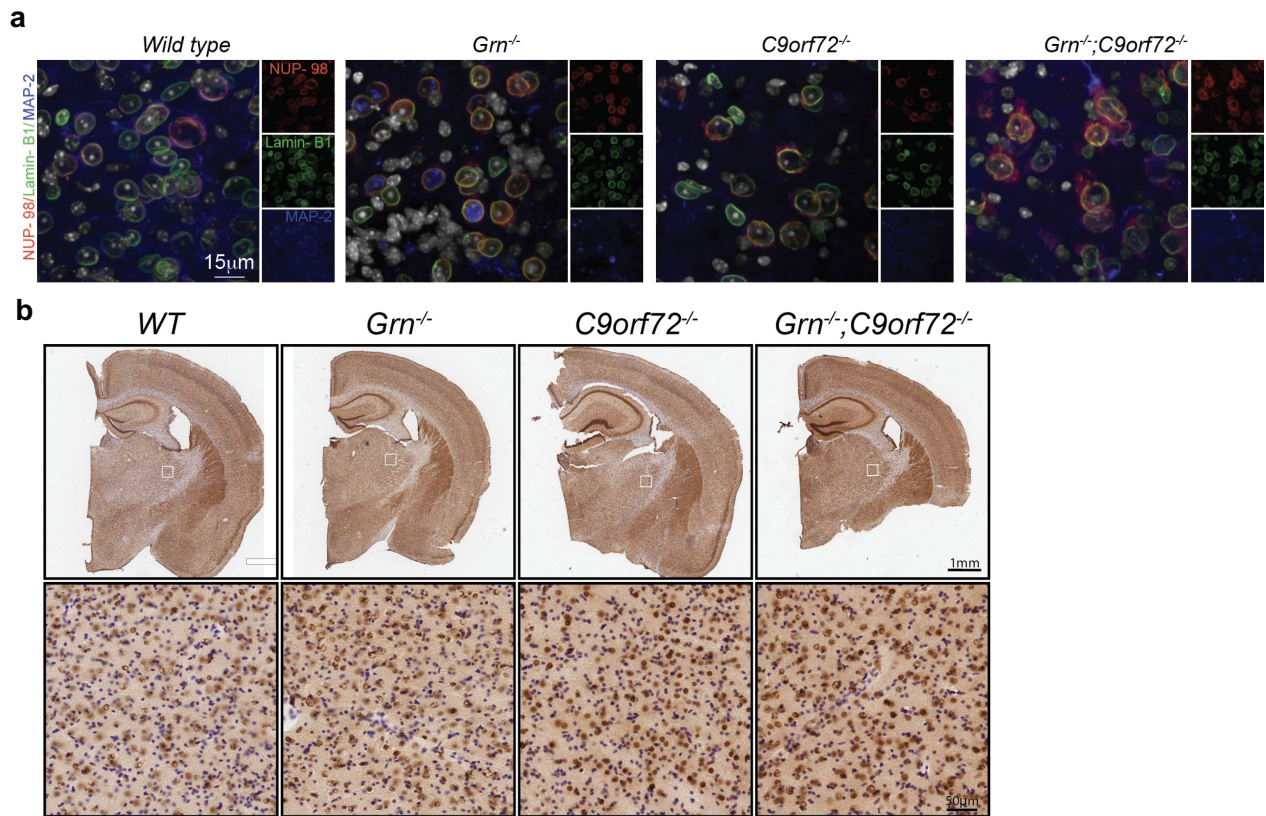


Figure 2.6. Neuronal nuclear protein mislocalization in knockout mice thalamus.
(a) Lamin-B1 (green) Map-2(blue) and Nup98(red) IF of *WT*, *Grn^{-/-}*, *C9orf72^{-/-}* and *Grn^{-/-};C9orf72^{-/-}* mice brain thalamus at 12 months (Scale bar = 15 μm) **(b)** TDP-43 IHC of *WT*, *Grn^{-/-}*, *C9orf72^{-/-}* and *Grn^{-/-};C9orf72^{-/-}* mice at 12 months (Scale Bar = 50μm inset, Scale bar = 1mm hemibrain)

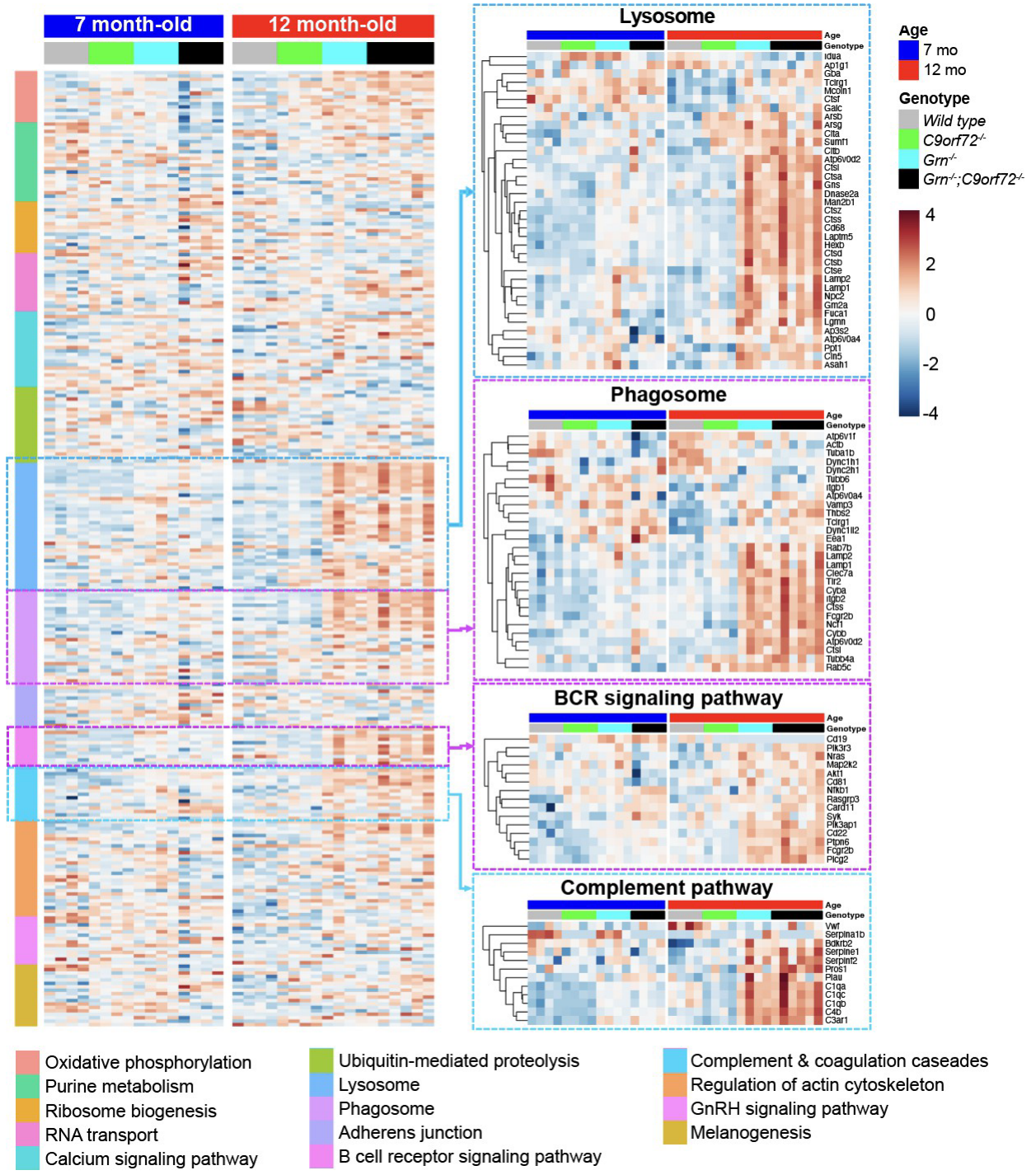


Figure 2.7. Heatmap of bulk-transcriptomic analysis of WT, *Grn*^{-/-}, *C9orf72*^{-/-} and *Grn*^{-/-};*C9orf72*^{-/-} mice at ages 7 and 12 months old show age dependent changes in DEGs and pathways involved.

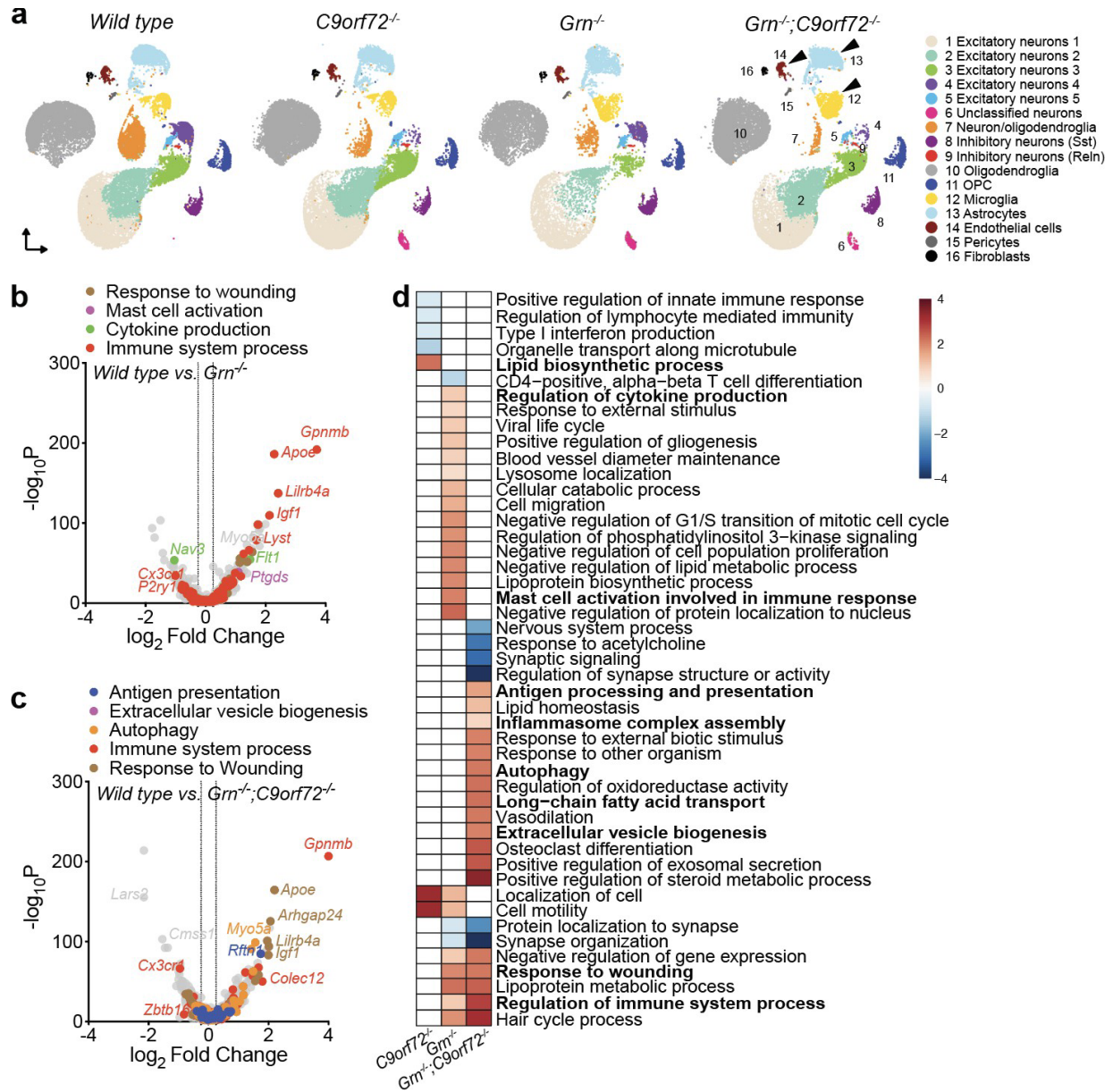


Figure 2.8. Increased inflammatory and antigen presentation signatures in *Grn*^{-/-};*C9orf72*^{-/-} microglial cluster.

(a) Unbiased clustering of single-nucleus RNA-seq (snRNA-seq) data from WT, *Grn*^{-/-}, *C9orf72*^{-/-} and *Grn*^{-/-};*C9orf72*^{-/-} mice thalamus at 12 months (b) Volcano plot showing persistent up- or downregulated genes in *Grn*^{-/-} microglia (c) Volcano plot showing persistent up- or downregulated genes in *Grn*^{-/-};*C9orf72*^{-/-} microglia (d) Heatmap of snRNA-seq analysis of *Grn*^{-/-}, *C9orf72*^{-/-} and *Grn*^{-/-};*C9orf72*^{-/-} mice microglia

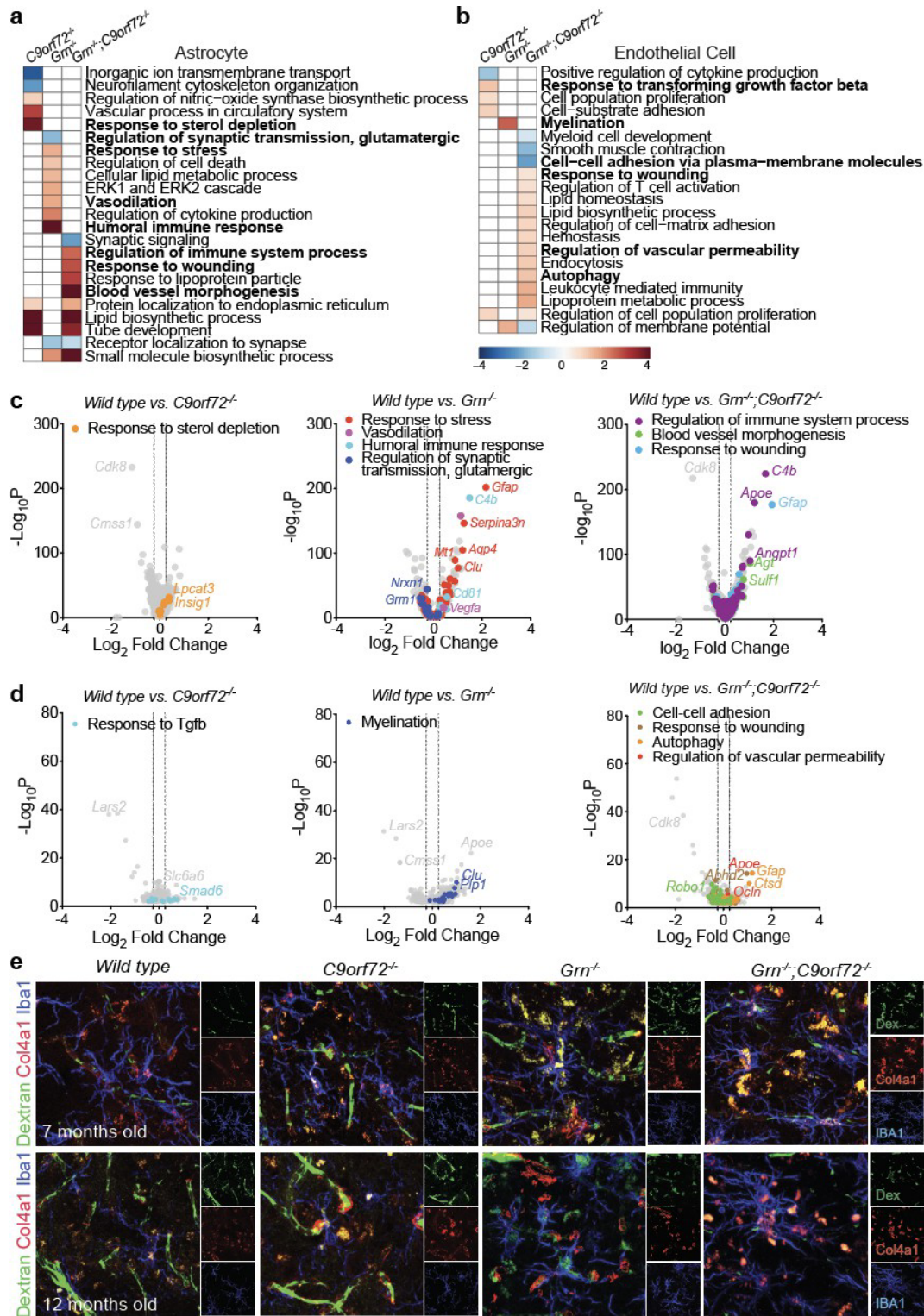


Figure 2.9. Contribution of astrocytes and endothelial cells in *Grn^{-/-}*, and *Grn^{-/-};C9orf72^{-/-}* mice brain thalamus BBB disruption. (Figure caption continued on the next page.)

(Figure caption continued from the previous page.) **(a)** Heatmap of sn-RNA seq analysis of *Grn*^{-/-}, *C9orf72*^{-/-} and *Grn*^{-/-};*C9orf72*^{-/-} mice astrocytes **(b)** Heatmap of sn-RNA seq analysis of *Grn*^{-/-}, *C9orf72*^{-/-} and *Grn*^{-/-};*C9orf72*^{-/-} mice endothelial cells **(c)** Volcano plot showing persistent up- or downregulated genes in *Grn*^{-/-}, *C9orf72*^{-/-} and *Grn*^{-/-};*C9orf72*^{-/-} mice astrocytes **(d)** Volcano plot showing persistent up- or downregulated genes in *Grn*^{-/-}, *C9orf72*^{-/-} and *Grn*^{-/-};*C9orf72*^{-/-} mice endothelial cells **(e)** Dextran 40kDA (green) Iba-1 (blue) and Col4a1 (red) IF of *WT*, *Grn*^{-/-}, *C9orf72*^{-/-} and *Grn*^{-/-};*C9orf72*^{-/-} mice brain thalamus at 7 and 12 months (Scale bar = 15 μm)

Chapter 3

Multi-omic characterization of *Grn*^{-/-}, *C9orf72*^{-/-} and *Grn*^{-/-};*C9orf72*^{-/-} of peripheral immune cells

Introduction

Results in Chapters 1 and 2 support my hypothesis of a possible autoimmune dysregulation, and interaction of CNS and peripheral immune cells in *Grn*^{-/-};*C9orf72*^{-/-} mice, resulting in peripheral and CNS tissue damage orchestrated by the immune cells. Of interest, were the findings of increased IgG expression in the blood plasma in the *Grn*^{-/-};*C9orf72*^{-/-} and *C9orf72*^{-/-} mice (**Figure 1.2**) deposition of IgG in the *Grn*^{-/-};*C9orf72*^{-/-} and *C9orf72*^{-/-} mice (Figure 1.3), BBB disruption in *Grn*^{-/-};*C9orf72*^{-/-} and *C9orf72*^{-/-} mice (**Figure 2.2, 2.3**) and increased transcriptomic signature of B-cell receptor signaling and antigen processing and presentation in *Grn*^{-/-};*C9orf72*^{-/-} mice (**Figure 2.7, 2.8**). These findings indicate that C9orf72 protein has a more profound function in the peripheral immune cells, and that loss of function in PGRN results in greater CNS inflammation and BBB. Together, reduction in both genes' activity resulted in the unmasking of affected brain regions important in disease pathology, in addition to a possible mechanism of action via upregulation of B- cell signature.

Current literature has predominantly focused on the effects of T cells in the progression of neurodegeneration, although new evidence of B-cells' contribution is emerging in diseases such as AD and Parkinson's (Sabatino et al., 2019). This chapter focuses on the transcriptomic characterization of peripheral immune tissues (blood and spleen) by Dr. Rufei Lu to find evidence of the aforementioned B-cell signature in the periphery.

Results

Grn^{-/-};C9orf72^{-/-} mice have an increased proportion of reactive B cell population

To understand the role of peripheral immune cells in modulating the observed transcriptomic and histological changes, we performed Cellular indexing of transcriptomes and epitopes sequencing (CITE-seq) on 7-month-old spleen tissue from all four genotypes due to its capability of providing single cell based transcriptomic readout in addition to cell surface marker quantification. UMAP of the dataset generated from spleen CITE-seq shows an increase in the size of clusters 19, 20 and 21 denoting for Age-associated B-cells, IgM- IgD- B-cells and Activated b- cells respectively in only the *Grn^{-/-};C9orf72^{-/-}* mice (**Figure 3.1a**). Flow cytometry of spleen at 4, 7 and 12 months old spleen shows and slight elevation in Activated B cells (CD19⁺CD80/86^{hi}MHCII^{hi}) of *Grn^{-/-};C9orf72^{-/-}* and *C9orf72^{-/-}* mice as early as 4 months old, although at 7 months old only *Grn^{-/-};C9orf72^{-/-}* mice have an increased proportion of activated B-cells (**Figure 3.1b**). At 12 months of age both *Grn^{-/-};C9orf72^{-/-}* and *C9orf72^{-/-}* mice have increased proportion of activated B-cells, although higher in *Grn^{-/-};C9orf72^{-/-}* mice. Age-associated B (CD19⁺T-bet⁺) cells population in the spleen increased in *Grn^{-/-};C9orf72^{-/-}* mice spleen at 7 months old and at 12 months old *Grn^{-/-};C9orf72^{-/-}* and *C9orf72^{-/-}* mice have increased in age associated B-cells with *Grn^{-/-};C9orf72^{-/-}* mice spleen having the greater proportion in comparison. Circulating activated and age-associated B-cells starts increasing at 7 months of age only in *Grn^{-/-};C9orf72^{-/-}* mice, with both *Grn^{-/-};C9orf72^{-/-}* and *C9orf72^{-/-}* mice showing increased proportion of circulating activated B-cells at 12 months of age (**Figure 3.1c**).

Given that activated B-cells further proliferate into antibody-producing B-cells and plasma cells (Pierce, 2009), our findings in this chapter of increased activated B-cells in *Grn*^{-/-};*C9orf72*^{-/-} and *C9orf72*^{-/-} mice corroborate the increase in Ig's in the blood plasma seen in our findings from Chapter 1. Interestingly, premature accumulation of age-associated B-cells has been shown in literature as a hallmark for patients with infectious or autoimmune diseases such as SLE (Sachinidis et al., 2020). With the high proportion of age-associated B-cells in 7 months old *Grn*^{-/-};*C9orf72*^{-/-} mice and 12 months old *Grn*^{-/-};*C9orf72*^{-/-} and *C9orf72*^{-/-} mice, in addition to our ELISA results showing accumulation of antibodies against ANA and ds-DNA in *Grn*^{-/-};*C9orf72*^{-/-} and *C9orf72*^{-/-} mice at 7 months old (**Figure 1.1 b,c**), our data further validates the presence of autoimmune dysfunction in *Grn*^{-/-};*C9orf72*^{-/-} and *C9orf72*^{-/-} mice preceding the neuro-immune and neurodegenerative phenotypes we observe in the *Grn*^{-/-};*C9orf72*^{-/-} mice.

Knockout mice have shared autoantibodies that target peripheral and CNS cells

In light of our data showing the presence of autoimmune dysfunction in *Grn*^{-/-};*C9orf72*^{-/-} and *C9orf72*^{-/-} mice, we performed CDI whole genome microarray screening from 12-month-old mice to characterize the autoantibody repertoire in *Grn*^{-/-};*C9orf72*^{-/-} and *C9orf72*^{-/-} mice. We identified a notable enrichment of autoantibodies targeting CNS in our knockout mice plasma (**Figure 3.2**). Among the shared autoantibodies, anti-ROBO3 was consistently detected in all knockouts. ROBO3 is an astrocytic and neuronal surface receptor that regulates axonal guidance during development. In addition to that, ROBO3 is also moderately expressed in the proximal renal tubules.

Discussion

Findings from this chapter offers an insight into B-cells mediated autoimmune dysfunction in all four knockout mice. In addition to that, our results indicate potential targets for autoantibodies that are present in both the CNS and the peripheral organs, one of which is the target ROBO3, found in the CNS astrocytes and the neurons, in addition to the kidney in the periphery.

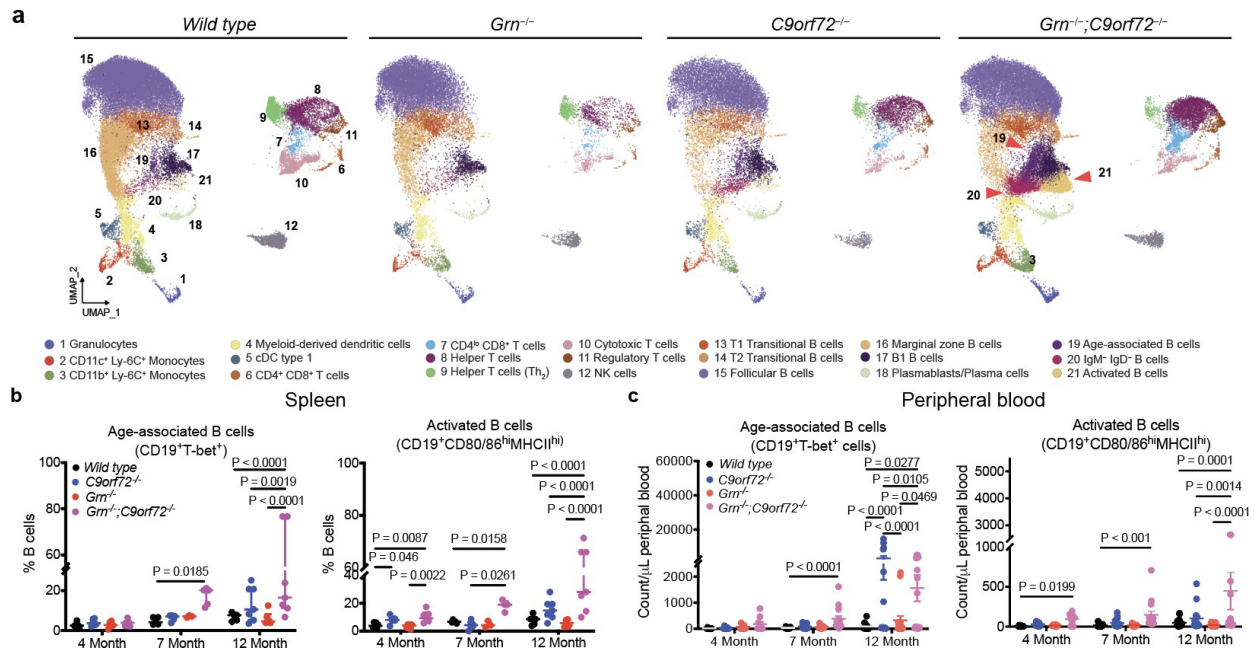


Figure 3.1. Expansion of B-Cell subsets in *Grn*^{-/-};*C9orf72*^{-/-} mice peripheral immune tissues

(a) Unbiased clustering of CITE-seq data from *WT*, *Grn*^{-/-}, *C9orf72*^{-/-} and *Grn*^{-/-};*C9orf72*^{-/-} mice spleen at 7 months. Proportion of Age-associated and Activated B-cells in *WT*, *Grn*^{-/-}, *C9orf72*^{-/-} and *Grn*^{-/-};*C9orf72*^{-/-} mice (b) spleen and (c) thalamus at 4, 7, and 12 months

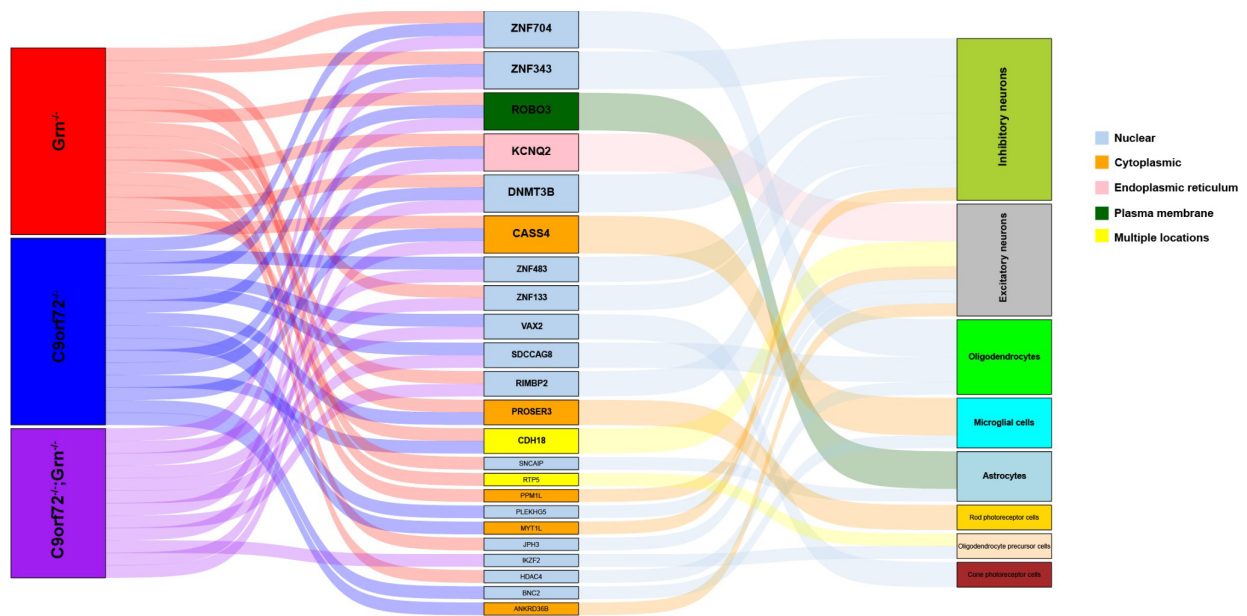


Figure 3.2. Sankey Plot of autoantibody targets from CDI microarray analysis of *WT*, *Grn*^{-/-}, *C9orf72*^{-/-} and *Grn*^{-/-};*C9orf72*^{-/-} mice blood plasma at 7 months

Chapter 4

Neuronal and microglial characterization of all four genotypes *in-vitro* (In Progress)

Introduction

Our findings now have provided the basis for our hypothesis that in addition to cell-intrinsic differences in the knockout glial and neuronal cells that result in their neuroimmune phenotypes, peripheral autoantibodies, such as anti-ROBO3 targeting neurons and astrocytes can mediate neuroinflammation and subsequent neurodegeneration.

This chapter includes preliminary results from our in-vitro neuronal and microglia culture.

Results

Anti-ROBO3 does not affect the survival of neurons in vitro

Primary neuronal culture generated from e15.5 embryos from all four genotypes were subjected to treatments with anti-ROBO3 antibody (1µg/ml) or Ctrl IgG2a,k antibody (1µg/ml) for 72 hours and fixed on Day 14 with 4% Paraformaldehyde. I stained the neurons for Map2 and cleaved-caspase2 (a marker for cell death) and quantified their dendritic arborization and the proportion of cleaved-caspase2+Map2 positive neurons post-treatment. Untreated *Grn^{-/-};C9orf72^{-/-}* and *Grn^{-/-}* neurons have increased presence of cleaved-caspase2+ Map2+ neurons that do not change after the addition of anti-ROBO3 (**Figure 4.1d**). Interestingly, Control IgG2a,k results in no change of cleaved-caspase2+ Map2+ *Grn^{-/-}* neuron or WT neuron proportions. Although more n's need to be added to the conditions, our working hypothesis is that the addition of either the Control IgG2a,k or anti-ROBO3 antibody to the neurons does not result in additional cell death

phenotype. Histological analysis of the neurons against ROBO3 expression shows that ROBO3 is present in the synapses and thus I am in the process of quantifying the total number of functional synapses present in treated versus untreated neurons with anti-ROBO3 antibody.

Upon performing Sholl analysis to compare the branching complexity in these neurons, we observe that *WT* neurons have a greater number of branch intersections early on compared to other genotypes in untreated conditions (**Figure 4.1a**) suggesting that morphologically, all three knockout neurons are less ramified compared to other genotypes. Upon treatment with Control IgG2ak, *WT* neurons Sholl intersection drastically reduces, along with a slight reduction in that of *C9orf72*^{-/-} neurons and no change in *Grn*^{-/-} neurons arborization complexity (**Figure 4.1b**). Upon treatment with anti-ROBO3 antibody, we observe no significant changes in the branching complexity in *WT* neurons, although neuron arbor length is reduced compared to that of untreated neurons (**Figure 4.1c**). No noticeable changes were observed in knockout neurons. We are currently missing data points *C9orf72*^{-/-} and *Grn*^{-/-};*C9orf72*^{-/-} neurons treated with Control IgG2a,k and are in the process of generating biological replicates for quantification to finalize the results.

Grn^{-/-} microglia show increased accumulation of zymosan beads over time

Given our data from the previous chapter demonstrating an age-dependent increase in genes representing lysosome and phagosome-related pathways in both *Grn*^{-/-};*C9orf72*^{-/-} and *Grn*^{-/-} mice brains, I treated serum-free microglia from all four genotypes with pHrodo Green zymosan beads (Invitrogen, P35365) and observed their phagocytic

engulfment activity. Given that these beads fluoresce green upon being in acidic solutions, the microglial engulfment activity was observed in the IncuCyte Live cell imaging system every hour for 24 hours.

I observe that *Grn*^{-/-} microglia accumulate a greater number of fluorescent zymosan beads over time (**Figure 4.1e**). On the other hand, *C9orf72*^{-/-} microglia accumulate a reduced number of fluorescent zymosan over time compared to that seen in *WT* microglia. *Grn*^{-/-};*C9orf72*^{-/-} microglia have a similar level of green fluorescence as that seen in *WT* microglia. These results indicate that *Grn*^{-/-} microglia accumulate zymosan particles over time and have trouble digesting the particles. Given that the particles fluoresce green with *Grn*^{-/-} microglia, it is safe to say that the lysosomal compartment taking up the particles *Grn*^{-/-} microglia does not have issues with acidification, rather, the enzymatic digestion required for the breakdown of the zymosan particles in *Grn*^{-/-} microglia are dysfunctional. These findings are similar to other lysosomal storage diseases, where there is an accumulation of substrates in the lysosome due to defects in the lysosomal enzymatic activity, such as that observed in Neuronal Ceroid Lipofuscinosis (NCL) diseases, occurring in patients with PGRN haploinsufficiency (Ward et al., 2017). Interestingly, reduction in *C9orf72* protein activity brings the zymosan accumulation level similar to that seen in *Grn*^{-/-};*C9orf72*^{-/-} microglia. More work is currently on the way to parse the involvement of Toll-Like receptors in the phagocytosis activity of the microglia in all four genotypes.

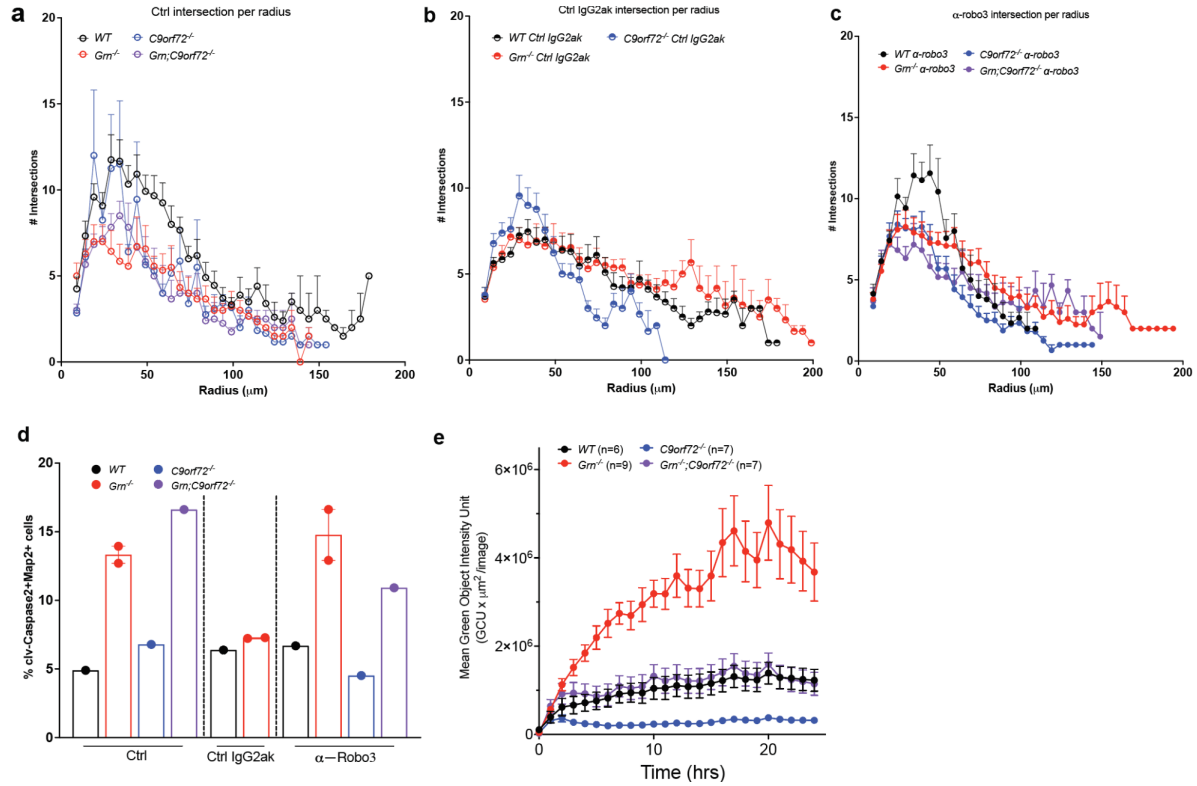


Figure 4.1. *In vitro* WT, *Grn*^{-/-}, *C9orf72*^{-/-} and *Grn*^{-/-};*C9orf72*^{-/-} neuron and microglial culture

(a-c) Sholl analysis of WT, *Grn*^{-/-}, *C9orf72*^{-/-} and *Grn*^{-/-};*C9orf72*^{-/-} Map2+ neurons at DIV14 upon 72 hours of **(a)** No treatment **(b)** Control IgG2a,k antibody **(c)** anti-ROBO3 antibody (n≥6 from 1 coverslip, two e15.5 embryonic neurons for one coverslip) **(d)** cleaved-Caspase2+Map2+ neuron proportion of WT, *Grn*^{-/-}, *C9orf72*^{-/-} and *Grn*^{-/-};*C9orf72*^{-/-} neurons (n≥1, ≥10 image per coverslip) **(e)** MOI of 24 hour pHrodo Zymosan Phagocytosis assay from WT, *Grn*^{-/-}, *C9orf72*^{-/-} and *Grn*^{-/-};*C9orf72*^{-/-} microglia (n≥6)

Discussion

I observed two concurrent activities occurring in our knockout animals due to the loss of function in *Grn* and *C9orf72* genes. One part of it is the cell intrinsic neuroinflammation occurring within the CNS due to loss of function in *Grn* resulting in glial (microglia and astrocytes) activation in the thalamus via upregulation of pathways involved in lysosomal, phagocytic, and complement pathways. Simultaneous loss of function in *Grn* and *C9orf72* genes also results in the unmasking of glial activation in additional limbic regions (amygdala, piriform cortex) that are relevant to patients with FTD. I also observe blood-brain barrier disruption occurring in *Grn*^{-/-} and *Grn*^{-/-};*C9orf72*^{-/-} mice, albeit much exacerbated in *Grn*^{-/-};*C9orf72*^{-/-} mice. All three knockout conditions have dystrophic neuronal nuclear membranes with mislocalization of nuclear proteins, although I only observe a greater loss of neurons in the thalamus that are of excitatory origin in the *Grn*^{-/-}. Additional experiments to characterize the neuronal phenotypes need to be executed to uncover the activities of PGRN and C9orf72 proteins within the neurons.

Gross peripheral characterization of the tissues such as blood and spleen and kidney allowed us to uncover that the early lethality I observed in the *Grn*^{-/-};*C9orf72*^{-/-} mice occurred due to organ damage caused by the presence of autoantibodies. Transcriptomic analysis of blood and spleen allowed us to identify the autoantibodies within *Grn*^{-/-};*C9orf72*^{-/-} mice that are also found in single knockout animals, that target both the peripheral and CNS tissue. Not only that, CITE-seq and flow data from blood and spleen show that *Grn*^{-/-};*C9orf72*^{-/-} mice have a greater number of activated and age-associated B cells present in their spleen and blood at an earlier age compared to the single knockout mice. According to the literature, precocious expansion of age-associated B-cells is a

hallmark for autoimmune related issues. Hence, the abundance of autoantibodies in the *Grn^{-/-};C9orf72^{-/-}* mice and *C9orf72^{-/-}* mice have the greater CNS effects in the double knockout due their added disruption in their BBB, not observed in the *C9orf72^{-/-}* mice.

Considering these findings, the double knockout mouse model provides a tool to study the additional gliosis and B-cell mediated autoimmune phenotype that is relevant to the disease model which the individual knockout mice were previously lacking.

Future Directions

Our study has uncovered the involvement of B-cell mediated autoantibody formation as a potential driver for the autoimmune phenotype seen in the double knockout mice in addition to the disease-relevant expansion of gliosis in the CNS limbic regions. With the uncovering of these mechanisms, we are faced with several research questions that will shed light on the mechanisms behind the co-occurring phenotypes I observe in our double knockout mice model.

Some of the questions that require further investigation involve dissecting the glial lysosomal and phagocytic activities in all four genotypes. We are currently in the process of performing in vitro microglia phagocytic assays to uncover the receptors involved in the differential phagocytic activities in the four genotypes. In addition, I find that the accumulation of substrate in *Grn^{-/-}* microglia is reversed by the loss of function in the C9orf72 protein. To uncover the intracellular interaction of PGRN and C9orf72 proteins via proteomic analysis of the microglial lysosome contents would allow us to dissect the difference in digestion of zymosan substrates in the different genotypes.

I observe greater neuronal nuclear pore protein mislocalization in the double knockout animals, although the individual knockouts have similar phenotype, but to a lesser extent. In vitro culture shows that both *Grn*^{-/-};*C9orf72*^{-/-} and *Grn*^{-/-} neurons are prone to accumulating cleaved-caspase2 (a marker for cell death) suggesting that loss of function in *Grn* renders the neurons more prone to cell death. Given that *C9orf72* loss of function results in increased thalamocortical arborization, electrophysiological characterization of this circuit would allow us to see whether single double knockout results in changes in neuronal activity.

My finding of BBB disruption in *Grn*^{-/-};*C9orf72*^{-/-} and *Grn*^{-/-} mice further begs the question whether the BBB disruption occurred due to the intrinsic cellular architecture change of the BBB in these mice, or did it occur in response to the elevated levels of B-cells and autoantibodies that are present in these animals. To test these questions, *in vitro* endothelial cultures would allow us to observe the effect of loss of function in PGRN and C9orf72 proteins in the BBB, along with characterizing CNS specific loss of function in these two proteins.

Materials and Methods

Animals:

All experiments were conducted in accordance with the University of California San Francisco Institutional Animal Care and Use Committee guidelines that followed the National Institute of Health guidelines (IACUC Protocol #AN169548). Mice carrying deletion of exons 2–13 of the mouse *Grn* gene were used from previous studies in our laboratory (Martens et al., 2012; Nguyen et al., 2018). *C9orf72*^{-/-} mice were obtained from Jackson Laboratory (RRID:IMSR_JAX:027068) with the F12 *C9orf72* null allele (deletion of 79bp in exon 2) as described in the 2016 publication from the Baloh group (O'Rourke et al., 2016). *Grn*^{-/-};*C9orf72*^{-/-} double knockout mice were generated by sequential mating between *Grn*^{-/-} and *C9orf72*^{-/-} mice and between the compound heterozygote mice.

Enzyme Linked Immunosorbent Assay (ELISA)

In this study, ELISA assays were employed to quantify the protein concentrations of anti-ds-DNA antibodies, anti-ANA antibodies, IgG, IgA, IgM, IgE, C1q and C3 in mice blood plasma. Depending on the manufacturer's instructions, 96 well plates were coated with a coating solution containing the capture antibody against the target of interest overnight at room temperature or 4°C. Following coating, wells are washed and blocked with a blocking buffer for 1-2 hours to minimize non-specific binding. Samples and standards were added to the wells at manufacturer's recommended dilution subsequently and incubated for 2 hours, followed by another set of washes, enzyme conjugated secondary antibody incubation and washes. Enzymatic reaction was initiated using Tetramethylbenzidine (TMB) substrate and stopped after 5-10 minutes of incubation

using the stop solution provided by the manufacturer where the color of the solution turns from blue to yellow. The absorbance value was recorded using Spectramax ID3 microplate reader and SoftMax Pro software at 450 nm. All steps were conducted according to the manufacturer's instructions and optimized for maximum sensitivity. Prism 10 (Graphpad) was used to generate the standard curve and a linear regression analysis was performed on the plotted data to determine the goodness of fit (R^2) and significance of the linear trend.

Immunohistochemical staining and stereology quantification

Chromogenic Immunohistochemical stains were performed on 40 μm free-floating brain sections of 4% PFA-fixed mouse brains and 5 μm deparaffinized spleen, lymph node and kidney. The immunostaining was developed using 3,3' diaminobenzidine (DAB) technique. Sections were rinsed in TBS and quenched with 10% methanol and 3% H_2O_2 in TBS for 10 minutes. Antigen retrieval was performed using 0.01M sodium citrate buffer (pH 6.0) or Tris EDTA (pH 9) for 5-10 minutes at 95 $^\circ\text{C}$ when needed. Sections were rinsed three times with TBS and incubated with TBS+ (10% goat serum and 0.2% Triton X-100) blocking buffer for 1 hour, followed by overnight incubation of primary antibodies at RT. Biotinylated secondaries were incubated for 2 hours at RT and rinsed three times with TBS. The VECTASTAIN Elite ABC HRP system with A (Avidin) and B (Biotinylated HRP) complexes in TBS++++ (10% goat serum, 3% BSA, 1% glycine, and 0.4% Triton X-100) was used to amplify staining specificity. Signals were developed in DAB reaction solution (0.05% DAB and 0.05% H_2O_2 in 0.1 M Tris, pH 8.0) and stopped with three washes in 0.1 M Tris (pH 8.0), ending with dehydration in 100% ethanol and

counterstaining using Cresyl Violet Staining. Slides were coverslipped using Cytoseal mounting medium. Primary antibodies for immunohistochemistry Iba-1 (Wako, 019-19741, 1:3000), GFAP (Dako, Z 0334, 1:3000), Neun (Millipore MAB377, 1:300), VGlut2 (Synaptic Systems, 135404, 1:500) and Pkc δ (Abcam, 1812126, 1:2000). Secondary antibodies for immunohistochemistry included goat anti-rabbit IgG antibody (H+L), biotinylated (Vector Laboratories, BA-1000, 1:300) and goat anti-mouse IgG antibody (H+L), biotinylated (Vector Laboratories, BA-9200, 1:300). For stereology-based quantification, Iba-1-positive microglia, GFAP-positive astrocytes and Neun-positive neurons were counted using optical fractionator based unbiased method using Stereo Investigator on a PC that is attached to an Olympus BX5 microscope with a motorized XYZ stage (MBF Biosciences, Williston, VT)(Martens et al., 2012). DAB staining images were captured using the Aperio AT2 scanner and Aperio ImageScope (Leica Biosystems) with a 40X objective.

Immunofluorescent staining

Immunofluorescent staining was done on 40 μ m free-floating sections of 4% PFA-fixed mouse brain tissue and glass coverslips of fixed neurons culture. Antigen retrieval was performed for selected antigens with 10 mM sodium citrate buffer (pH 6.0) Tris EDTA (pH 9) for 5-10 at 95 $^{\circ}$ C. . Samples were then washed with TBS for 5 minutes and repeated 3 times, before blocking with TBS++++ for 1 hour. Slides were incubated with primary antibodies with denoted dilutions overnight at RT. Alexa fluorophore conjugated secondary antibodies diluted in TBS++++ (1:300) were added on the following day for 2 hours. Slides were then stained with DAPI and coverslipped.

Immunogold electron microscopy (IEM)

Mouse brain tissues for IEM analysis were fixed with 4% PFA overnight. Following the fixation, 40 μm -thick free-floating sections were incubated with a cryoprotectant solution for 2 hours at room temperature and freeze-thawed. The sections were incubated with 4% blocking normal goat serum for 1 hour and with anti-CD18(ITGB2) antibody (Proteintech, 10554-1-AP, 1:50), GFAP (Dako, Z 0334, 1:50), Iba-1 (Wako, 019-19741, 1:50) in 1% blocking normal goat serum overnight. After that, the sections were incubated with 0.2% BSAc and 0.2% fish gelatin (both from Electron Microscopy Sciences, Hatfield, PA) in PBS for 10 minutes and with gold nanoparticle-conjugated secondary antibodies, including goat anti-rabbit IgG (H+L), Ultra Small (Electron Microscopy Sciences, 25101, 1:100) or goat anti-mouse IgG (H+L), Ultra Small (Electron Microscopy Sciences, 25123, 1:100) for 2 hours. After the PBS washes, the sections were fixed in 1% glutaraldehyde for 10 minutes. The immunogold particle signal was increased using a silver enhancement kit (Electron Microscopy Sciences, 25521) at 37°C for 2 hours. Finally, the sections were post-fixed in 0.5% osmium tetroxide for 10 minutes, dehydrated, and embedded in resin. To quantify IgG granule, we used NIH ImageJ, traced the area within the blood vessel, and used Cell Counter to quantify the number of particles within the blood vessel lumen and in the parenchyma.

Bulk RNA sequencing, analysis, and GSEA

Bulk RNA sequencing of 12 months and 7 months mouse left brain hemisphere was performed on Illumina HiSeq4000 machine (with an average depth of 35 million reads/sample) as a paid service at UCSF Genomics Core Facility. For this study, we sent

cDNA samples from 12 months *WT* (2 female+2 male), 7 months *WT* (2 female+2 male) 12 months *Grn*^{-/-} (2 female+2 male), 7 months *Grn*^{-/-} (2 female+2 male), 12 months old *C9orf72*^{-/-} (2 female+2 male), 7 months old *C9orf72*^{-/-} (2 female+2 male) 12 months old *Grn*^{-/-};*C9orf72*^{-/-} (2 female+4 male) and 7 months old *Grn*^{-/-};*C9orf72*^{-/-} (2 female+2 male). For each sample, RNA was extracted from the left-brain hemisphere using the QUIAGEN RNeasy Mini kit and loaded as input for cDNA amplification. RNA concentration was measured using Agilent 2100 BioAnalyser with RIN>7 and diluted to 10 ng/μL with the total RNA amount of 100 ng per sample provided to the Genomics Core Facility. Libraries were constructed by them using Takara SMART-seq (v4) and Illumina Nextera XT following the manufacturer's instructions. Library pools were quality-controlled and normalized using Illumina MiniSeq before pair-ended (150-bp reads). Finally, reads were aligned to hg38 using STAR (v2.7.2.b). EdgeR (version 3.34.1) in R software was used to normalize raw counts and perform differential gene expression analyses. In addition, DESeq2 (version 1.32.0) was used to generate heatmaps with variance stabilizing transformation (vst). Gene set enrichment analysis (GSEA) was performed with biological pathways in Gene ontology (c5.go.bp) from MSigDB (<https://www.gsea-msigdb.org/gsea/msigdb/>).

snRNAseq sample preparation

Single-nucleus libraries were sequenced on a S2 flowcell of the Illumina NovaSeq 6000 machine (with an average depth of 500 million reads/sample) as a paid service at UCSF Genomics Core Facility. The protocol for nuclei isolation for 10× snRNA-Seq was adapted from previous studies (Velmeshev et al., 2019; J. Zhang et al., 2020). Fresh

frozen mouse brain thalamus from the left hemisphere were dissected out over ice. 12 months old *WT* (3 female+3 male), 12 months old *Grn*^{-/-} (2 female+2 male), 12 months old *C9orf72*^{-/-} (4 female+4 male) 12 months old *Grn*^{-/-};*C9orf72*^{-/-} (3 female+ 3 male). They were homogenized in 5 mL of RNAase-free lysis buffer (0.32 M sucrose, 5 mM CaCl₂, 3 mM Mg(Ac)₂, 0.1 mM EDTA, 10 mM Tris-HCl, 1 mM DTT, 0.1% Triton X-100 in DEPC-treated water) using glass Dounce homogenizer (size A; Thomas Scientific) on ice. The homogenate was loaded into a 30 mL–thick polycarbonate ultracentrifuge tube (Beckman Coulter). Nine mL of sucrose solution (1.8 M sucrose, 3 mM Mg(Ac)₂, 1 mM DTT, 10 mM Tris-HCl in DEPC-treated water) was added to the bottom of the tube with the homogenate. The tubes were placed in a SW28 rotor and centrifuged at 107,000g for 2.5 hours at 4°C. The supernatant was aspirated, and the nuclei pellets were incubated in 250 µL of DEPC-treated PBS for 20 minutes on ice before resuspending the pellet. The nuclear suspension was filtered through a 30 µm cell strainer (Miltenyi Biotec). Nuclei were counted before performing single-nucleus capture on the 10× Genomics Single-Cell 3' system V2 for human samples, V3 for mouse samples. Target capture of 4,000 nuclei per sample was used. The 10× capture and library preparation were performed using the manufacturer's protocol.

snRNA seq data processing and dimensionality reduction

Analyses of snRNA-Seq data were adapted from our previous studies (J. Zhang et al., 2020). CellRanger software v.1.3.1 default parameters were used for fastq files generation, reads alignment and unique molecular identifiers (UMIs) quantification, with the exception of the use of a pre-mRNA reference file (ENSEMBL, GRCh38) to insure

capturing intronic reads originating from pre-mRNA transcripts abundant in the nuclear fraction. Individual expression matrices containing numbers of UMIs per nucleus per gene were filtered to retain nuclei with at least 500 genes expressed and less than 5% of total UMIs originating from mitochondrial and ribosomal RNAs. Genes expressed in less than 3 nuclei were filtered out. In addition, mitochondrial RNAs were filtered out to exclude transcripts coming from outside of the nucleus to avoid biases introduced by nuclei isolation and ultracentrifugation. Individual matrices were combined. UMIs were normalized to the total UMIs per nucleus and log transformed. A filtered log-transformed UMI matrix was used to perform truncated singular value decomposition (SVD) with $k = 50$. A scree plot was generated to select the number of significant principal components (PCs) by localizing the last PC before the explained variance reaches plateau. The significant PCs were used to calculate Jaccard distance-weighted nearest-neighbor distances; the number of nearest neighbors was assigned to the root square of the number of nuclei. Resulting graph with Jaccard-weighted edges was used to perform Louvain clustering.

To visualize nuclei transcriptomic profiles in 2-dimensional space, Uniform Manifold Approximation and Projection for dimensionality reduction or UMAP was performed with the selected PCs and combined with cluster annotations. Cell types were annotated based on expression of known marker genes visualized on the UMAP plot and by performing gene marker analysis. Primary cell type annotations of clusters were performed by comparison with previously annotated cell types, and when a repository of substantial matching was not available, a combination of literature-based annotation was used. For sub-clusters, a set of markers, specifically, overexpressed genes, was defined

by differential expression analysis of the cells grouped in each subcluster against the remaining cells within the corresponding broad cell-type cluster. This analysis was applied to all cell types independently. DEGs interactions were assessed using the Venn diagrams software on the Van de Peer lab website (<https://www.vandeppeerlab.org/software?page=2>). Final Venn diagram was generated using the Eulerr.co website (<https://eulerr.co/>). For statistics, hypergeometric tests were performed on the Graeber Lab website (<https://systems.crump.ucla.edu/hypergeometric/>). GO enrichment analyses were performed using Metascape. For all cases we used the set of 17,926 protein-coding genes included in the QC data as background. All other plots including Heatmaps, Volcano plots and Scatter plots, were generated with ggplot2 on R studio.

CDI microarray

The evaluation of autoantibodies within mice blood was performed as a paid service from CDI ILabs, Toronto, Canada. Briefly, we used the HuProt™ V4 Human Proteome Microarray for this study and the mouse plasma samples were placed on array plates at a concentration of 1 µg/mL.

Statistical analysis of CDI

Raw intensity values are normalized using mouse anti-IgG isotype control. Kruskal-Wallis test (non-parametric) was performed using normalized intensity values to identify antigen targets that were significantly different among the genotypes. Pairwise comparisons were calculated using a non-parametric analysis (Wilcoxon test) on antigen

targets with adjusted p-value <0.1. Positivity of an autoantibody was defined as normalized intensity values greater than 2.5 standard deviations above the mean of the wildtype. Antibodies with q-value <0.05 and positivity rate >30% was used for final orthogonal assay comparison analysis.

Primary Microglia Cultures

Microglia Primary microglia cultures were prepared as previously described (Martens et al., 2012). Briefly, cerebral cortices were harvested from P3-4 *WT*, *Grn*^{-/-}, *C9orf72*^{-/-} and *Grn*^{-/-};*C9orf72*^{-/-} pups. The meninges were removed, and the cerebral cortices were dissected into smaller pieces with forceps and then triturated in DMEM, 20% FBS, Penicillin/Streptomycin (P/S), and 20 ng/ml of GM-CSF (PeproTech, Rocky Hill, NJ). The cells were grown in poly-L-lysine coated flasks. The media was replenished three days after the initial harvest. The microglia were harvested from the astrocyte layer 6-10 days later by shaking the flasks at 200 rpm for 1-2 hours at 37° C. The media was removed, and the cells were pelleted. For live cell imaging in the IncuCyte system, the microglia were re-suspended in Neurobasal media supplemented with N2 supplement, L-glutamine, and P/S for 18-24 hours before experimentation and seeded at 80,000 cells/well in 96 well plates. Right before the experiment, each well is seeded with 10µl pHrodo Bioparticles (Invitrogen, P35365) and imaged every hour for 24 hours.

Primary Neuronal Cultures

Primary cortical neurons were prepared from the cerebral cortex of E15.5 *WT*, *Grn*^{-/-}, *C9orf72*^{-/-} and *Grn*^{-/-};*C9orf72*^{-/-} embryos. Briefly, the cortical plates were dissected from embryos in ice cold HBSS, then transferred to 2 ml of 0.25% trypsin/EDTA solution, and incubated in 37°C water bath for 15 min. The dissociated cells were placed in DMEM/high glucose supplemented with 10% FBS, 1X penicillin/streptomycin, and 2 mM L-glutamine (Gibco) as previously reported (Lee et al., 2016; Shang et al., 2018). We routinely combined 2 or more E15.5 embryonic cortices with the goal to obtain enough cells to grow on multiple 12 mm coverslips. As such, each coverslip was considered as a biological replicate. Approximately 80,000 cells were plated on 12 mm glass coverslips, pre-coated with 1mg/ml poly-L-lysine (P2636, Sigma) in borate buffer solution, in 24-well plates. On in vitro day 1 (DIV1), cultured cortical neurons were switched to Neurobasal medium with 2% B-27 supplement (Invitrogen) and 200 µM L-glutamine twice to completely remove serum from culture media. On DIV2, 5 µM of Ara C was added to culture media to inhibit the growth of glial cells. Neurons are treated at DIV11 with anti-ROBO3 antibody (MyBiosource. MBS6012146) at 1µg/ml, or Control IgG2a,k mouse (Clone eBM2a)(Thermo eBioscience,1447282) at 1µg/ml and fixed with 4% Paraformaldehyde at DIV 14.

Cellular indexing of Transcriptome and Epitopes by sequencing (CITE-seq)

For this study, we obtained fresh spleen from 7 months *WT* (6 female+2 male), 7 months *Grn*^{-/-} (2 female+2 male), 7 months old *C9orf72*^{-/-} (2 female+2 male) and 7 months old *Grn*^{-/-};*C9orf72*^{-/-} (5 female+2 male). Each sample is stained with a uniquely tagged anti-

CD45 antibody and then samples are pooled and stained with antibodies tagged with a unique nucleotide sequence on ice. Stained cells are loaded onto a 10x Chromium Controller. Sample processing for single B cell receptor (BCR) V(D)J clonotype was done using Chromium Single Cell 5' Library and the Gel Bead Kit following the manufacturer's user guide. Subsequent library preparation using the published 10X Chromium Single Cell 3' v2 Solution protocol, libraries were sequenced on the NovaSeq6000 at a depth of 20,000 reads/cell using the recommended cycle numbers. BCL data were converted to FASTQ using Illumina bcl2fastq. Sequences are aligned; count matrices are generated using cellranger. Freemuxlet is used to de-multiplex the barcoded cells into its original donor. Doublets are removed using DoubletFinder. Cells with <5% mitochondrial genes, <1% hemoglobin genes, and <1% platelet genes are used for subsequent dimensional reduction (UMAP), differential gene expression (deseq2 and MAST), and pathway enrichment analysis (ClusterProfiler). V(D)J gene annotations are done using Immcantation R package.

B-cell specific flow cytometry of Spleen and blood

To validate the clusters identified in scRNA-seq, we performed flow cytometry of whole blood and spleen. For spleen dissociation, fresh spleen is minced in HBSS solution and then incubated in 5ml HBSS solution with Collagenase IV (100 U/mL Gibco Collagenase, Type IV, 17104019), DNase I (20 U/mL, Thermo Scientific DNase I solution, Cat. No. 90083), and 1% FBS and stopped by incubation with EDTA 1mM solution for 5 minutes. Digested spleen is passed through 70 µm cell strainer with excess PBS for single cell dissociation, followed by centrifugation at 400-600g at 4°C for 5 minutes, and

resuspension in cold PBS. Red blood cells are removed from dissociated spleen and whole blood using ACK lysis buffer (Thermo Fisher, A1049201) according to the manufacturer's instructions. Live/dead staining was performed with LIVE/DEAD Cell Vitality Assay Kit, C (Thermo Fisher Scientific, L34951) according to the manufacturer's instructions. Cells were subsequently stained at room temperature in the dark for 20 min with flow cytometry antibodies, diluted in FACS buffer (1 × PBS, 2% FBS, 2 mM EDTA). Cells were then washed twice with FACS buffer and resuspended in 1 × PBS for acquisition using BD FACS ARIA. Antibodies used in this study were: APC-CD93 (Thermo Scientific, 17-5892-32; 1:100), BV786-CD23 (BD, 563988, 1:100), PE-CF594-CD86 (BD, 567592, 1:100), PE-CF594-CD80 (BD, 562504, 1:100), BV421-CD138 (BD, 562610, 1:100), BV650-IgD (Biolegend, 748098, 1:100), PE-Cy7-IgM (Thermo Scientific, 25-5790-82, 1:100), FITC-CD11c (Thermo Fisher Scientific, 11-0114-85, 1:100), BV605-CD5(Clone 53.7.3, 1:100), PE-Cy5-MHCII (Clone M5/114.15.2, 1:100), APC-CD11b(Biolegend, 101211,1:100), PE-Tbet (Biolegend, 644809, 1:100), BV711-CD19 (BD, 563157).

Statistics and reproducibility

Results are mean ± SEM unless otherwise stated. Differences between 2 groups were assessed with unpaired, 2-tailed *t* tests. Comparisons involving more than 2 groups used an ANOVA with Tukey's post-hoc test. *P* values less than 0.05 were considered significant for all statistical analyses. Statistical analyses were done using Prism 10 (GraphPad).

Reference

- Ahmed, Z., Mackenzie, I. R., Hutton, M. L., & Dickson, D. W. (2007). Progranulin in frontotemporal lobar degeneration and neuroinflammation. *Journal of Neuroinflammation*, 4(1), 7. <https://doi.org/10.1186/1742-2094-4-7>
- Almeida, M. R., Macário, M. C., Ramos, L., Baldeiras, I., Ribeiro, M. H., & Santana, I. (2016). Portuguese family with the co-occurrence of frontotemporal lobar degeneration and neuronal ceroid lipofuscinosis phenotypes due to progranulin gene mutation. *Neurobiology of Aging*, 41, 200.e1-200.e5. <https://doi.org/10.1016/j.neurobiolaging.2016.02.019>
- Amick, J., & Ferguson, S. M. (2017). C9orf72: At the intersection of lysosome cell biology and neurodegenerative disease. *Traffic*, 18(5), 267–276. <https://doi.org/10.1111/tra.12477>
- Amick, J., Roczniak-Ferguson, A., & Ferguson, S. M. (2016). C9orf72 binds SMCR8, localizes to lysosomes, and regulates mTORC1 signaling. *Molecular Biology of the Cell*, 27(20), 3040–3051. <https://doi.org/10.1091/mbc.e16-01-0003>
- Atanasio, A., Decman, V., White, D., Ramos, M., Ikiz, B., Lee, H.-C., Siao, C.-J., Brydges, S., LaRosa, E., Bai, Y., Fury, W., Burfeind, P., Zamfirova, R., Warshaw, G., Orengo, J., Oyejide, A., Fralish, M., Auerbach, W., Poueymirou, W., ... Lai, K.-M. V. (2016). C9orf72 ablation causes immune dysregulation characterized by leukocyte expansion, autoantibody production and glomerulonephropathy in mice. *Scientific Reports*, 6(1), 23204. <https://doi.org/10.1038/srep23204>
- Atkinson, R. A. K., Fernandez-Martos, C. M., Atkin, J. D., Vickers, J. C., & King, A. E. (2015). C9ORF72 expression and cellular localization over mouse development.

Acta Neuropathologica Communications, 3(1), 59.

<https://doi.org/10.1186/s40478-015-0238-7>

- Baker, M., Mackenzie, I. R., Pickering-Brown, S. M., Gass, J., Rademakers, R., Lindholm, C., Snowden, J., Adamson, J., Sadovnick, A. D., Rollinson, S., Cannon, A., Dwosh, E., Neary, D., Melquist, S., Richardson, A., Dickson, D., Berger, Z., Eriksen, J., Robinson, T., ... Hutton, M. (2006). Mutations in progranulin cause tau-negative frontotemporal dementia linked to chromosome 17. *Nature*, 442(7105), 916–919. <https://doi.org/10.1038/nature05016>
- Bang, J., Spina, S., & Miller, B. L. (2015). Frontotemporal dementia. *The Lancet*, 386(10004), 1672–1682. [https://doi.org/10.1016/S0140-6736\(15\)00461-4](https://doi.org/10.1016/S0140-6736(15)00461-4)
- Bateman, A., & Bennett, H. (1998). Granulins: The structure and function of an emerging family of growth factors. *Journal of Endocrinology*, 158(2), 145–151. <https://doi.org/10.1677/joe.0.1580145>
- Bateman, A., & Bennett, H. P. J. (2009). The granulin gene family: From cancer to dementia. *BioEssays*, 31(11), 1245–1254. <https://doi.org/10.1002/bies.200900086>
- Benussi, A., Padovani, A., & Borroni, B. (2015). Phenotypic Heterogeneity of Monogenic Frontotemporal Dementia. *Frontiers in Aging Neuroscience*, 7. <https://doi.org/10.3389/fnagi.2015.00171>
- Bettcher, B. M., Tansey, M. G., Dorothée, G., & Heneka, M. T. (2021). Peripheral and central immune system crosstalk in Alzheimer disease—A research prospectus. *Nature Reviews Neurology*, 17(11), 689–701. <https://doi.org/10.1038/s41582-021-00549-x>

- Bhandari, V., Giaid, A., & Bateman, A. (1993). The complementary deoxyribonucleic acid sequence, tissue distribution, and cellular localization of the rat granulin precursor. *Endocrinology*, *133*(6), 2682–2689.
<https://doi.org/10.1210/endo.133.6.8243292>
- Burberry, A., Suzuki, N., Wang, J.-Y., Moccia, R., Mordes, D. A., Stewart, M. H., Suzuki-Uematsu, S., Ghosh, S., Singh, A., Merkle, F. T., Koszka, K., Li, Q.-Z., Zon, L., Rossi, D. J., Trowbridge, J. J., Notarangelo, L. D., & Eggan, K. (2016). Loss-of-function mutations in the *C9ORF72* mouse ortholog cause fatal autoimmune disease. *Science Translational Medicine*, *8*(347).
<https://doi.org/10.1126/scitranslmed.aaf6038>
- Burberry, A., Wells, M. F., Limone, F., Couto, A., Smith, K. S., Keaney, J., Gillet, G., Van Gastel, N., Wang, J.-Y., Pietilainen, O., Qian, M., Eggan, P., Cantrell, C., Mok, J., Kadiu, I., Scadden, D. T., & Eggan, K. (2020). *C9orf72* suppresses systemic and neural inflammation induced by gut bacteria. *Nature*, *582*(7810), 89–94. <https://doi.org/10.1038/s41586-020-2288-7>
- Chang, M. C., Srinivasan, K., Friedman, B. A., Suto, E., Modrusan, Z., Lee, W. P., Kaminker, J. S., Hansen, D. V., & Sheng, M. (2017). Progranulin deficiency causes impairment of autophagy and TDP-43 accumulation. *Journal of Experimental Medicine*, *214*(9), 2611–2628.
<https://doi.org/10.1084/jem.20160999>
- Chen, X., Firulyova, M., Manis, M., Herz, J., Smirnov, I., Aladyeva, E., Wang, C., Bao, X., Finn, M. B., Hu, H., Shchukina, I., Kim, M. W., Yuede, C. M., Kipnis, J., Artyomov, M. N., Ulrich, J. D., & Holtzman, D. M. (2023). Microglia-mediated T

- cell infiltration drives neurodegeneration in tauopathy. *Nature*, 615(7953), 668–677. <https://doi.org/10.1038/s41586-023-05788-0>
- Chen, Y., Li, S., Su, L., Sheng, J., Lv, W., Chen, G., & Xu, Z. (2015). Association of progranulin polymorphism rs5848 with neurodegenerative diseases: A meta-analysis. *Journal of Neurology*, 262(4), 814–822. <https://doi.org/10.1007/s00415-014-7630-2>
- Chou, V., Pearse, R. V., Aylward, A. J., Ashour, N., Taga, M., Terzioglu, G., Fujita, M., Fancher, S. B., Sigalov, A., Benoit, C. R., Lee, H., Lam, M., Seyfried, N. T., Bennett, D. A., De Jager, P. L., Menon, V., & Young-Pearse, T. L. (2023). INPP5D regulates inflammasome activation in human microglia. *Nature Communications*, 14(1), 7552. <https://doi.org/10.1038/s41467-023-42819-w>
- Cruts, M., Gijssels, I., Van Der Zee, J., Engelborghs, S., Wils, H., Pirici, D., Rademakers, R., Vandenberghe, R., Dermaut, B., Martin, J.-J., Van Duijn, C., Peeters, K., Sciot, R., Santens, P., De Pooter, T., Mattheijssens, M., Van Den Broeck, M., Cuijt, I., Vennekens, K., ... Van Broeckhoven, C. (2006). Null mutations in progranulin cause ubiquitin-positive frontotemporal dementia linked to chromosome 17q21. *Nature*, 442(7105), 920–924. <https://doi.org/10.1038/nature05017>
- Daniel, R., Daniels, E., He, Z., & Bateman, A. (2003). Progranulin (acrogranin/PC cell-derived growth factor/granulin-epithelin precursor) is expressed in the placenta, epidermis, microvasculature, and brain during murine development. *Developmental Dynamics*, 227(4), 593–599. <https://doi.org/10.1002/dvdy.10341>
- Ducharme, S., Price, B. H., Larvie, M., Dougherty, D. D., & Dickerson, B. C. (2015).

- Clinical Approach to the Differential Diagnosis Between Behavioral Variant Frontotemporal Dementia and Primary Psychiatric Disorders. *American Journal of Psychiatry*, 172(9), 827–837. <https://doi.org/10.1176/appi.ajp.2015.14101248>
- Fredi, M., Cavazzana, I., Biasiotto, G., Filosto, M., Padovani, A., Monti, E., Tincani, A., Franceschini, F., & Zanella, I. (2019). C9orf72 Intermediate Alleles in Patients with Amyotrophic Lateral Sclerosis, Systemic Lupus Erythematosus, and Rheumatoid Arthritis. *NeuroMolecular Medicine*, 21(2), 150–159. <https://doi.org/10.1007/s12017-019-08528-8>
- Gate, D., Saligrama, N., Leventhal, O., Yang, A. C., Unger, M. S., Middeldorp, J., Chen, K., Lehallier, B., Channappa, D., De Los Santos, M. B., McBride, A., Pluinage, J., Elahi, F., Tam, G. K.-Y., Kim, Y., Greicius, M., Wagner, A. D., Aigner, L., Galasko, D. R., ... Wyss-Coray, T. (2020). Clonally expanded CD8 T cells patrol the cerebrospinal fluid in Alzheimer's disease. *Nature*, 577(7790), 399–404. <https://doi.org/10.1038/s41586-019-1895-7>
- Gendron, T. F., & Petrucelli, L. (2018). Disease Mechanisms of C9ORF72 Repeat Expansions. *Cold Spring Harbor Perspectives in Medicine*, 8(4), a024224. <https://doi.org/10.1101/cshperspect.a024224>
- Hashimoto, K., Jahan, N., Miller, Z. A., & Huang, E. J. (2022). Neuroimmune dysfunction in frontotemporal dementia: Insights from progranulin and C9orf72 deficiency. *Current Opinion in Neurobiology*, 76, 102599. <https://doi.org/10.1016/j.conb.2022.102599>
- He, Z., & Bateman, A. (2003). Progranulin (granulin-epithelin precursor, PC-cell-derived growth factor, acrogranin) mediates tissue repair and tumorigenesis. *Journal of*

Molecular Medicine, 81(10), 600–612. [https://doi.org/10.1007/s00109-003-0474-](https://doi.org/10.1007/s00109-003-0474-3)

3

Hickman, S., Izzy, S., Sen, P., Morsett, L., & El Khoury, J. (2018). Microglia in neurodegeneration. *Nature Neuroscience*, 21(10), 1359–1369.

<https://doi.org/10.1038/s41593-018-0242-x>

Hofmann, J. W., Seeley, W. W., & Huang, E. J. (2019). RNA Binding Proteins and the Pathogenesis of Frontotemporal Lobar Degeneration. *Annual Review of Pathology: Mechanisms of Disease*, 14(1), 469–495.

<https://doi.org/10.1146/annurev-pathmechdis-012418-012955>

Hogan, D. B., Jetté, N., Fiest, K. M., Roberts, J. I., Pearson, D., Smith, E. E., Roach, P., Kirk, A., Pringsheim, T., & Maxwell, C. J. (2016). The Prevalence and Incidence of Frontotemporal Dementia: A Systematic Review. *Canadian Journal of Neurological Sciences / Journal Canadien Des Sciences Neurologiques*, 43(S1), S96–S109. <https://doi.org/10.1017/cjn.2016.25>

Jian, J., Zhao, S., Tian, Q.-Y., Liu, H., Zhao, Y., Chen, W.-C., Grunig, G., Torres, P. A., Wang, B. C., Zeng, B., Pastores, G., Tang, W., Sun, Y., Grabowski, G. A., Kong, M. X., Wang, G., Chen, Y., Liang, F., Overkleeft, H. S., ... Liu, C. (2016). Association Between Progranulin and Gaucher Disease. *EBioMedicine*, 11, 127–137. <https://doi.org/10.1016/j.ebiom.2016.08.004>

Kao, A. W., McKay, A., Singh, P. P., Brunet, A., & Huang, E. J. (2017). Progranulin, lysosomal regulation and neurodegenerative disease. *Nature Reviews Neuroscience*, 18(6), 325–333. <https://doi.org/10.1038/nrn.2017.36>

Kessenbrock, K., Fröhlich, L., Sixt, M., Lämmermann, T., Pfister, H., Bateman, A.,

- Belaouaj, A., Ring, J., Ollert, M., Fässler, R., & Jenne, D. E. (2008). Proteinase 3 and neutrophil elastase enhance inflammation in mice by inactivating antiinflammatory progranulin. *Journal of Clinical Investigation*, JCI34694. <https://doi.org/10.1172/JCI34694>
- Krabbe, G., Minami, S. S., Etcheagaray, J. I., Taneja, P., Djukic, B., Davalos, D., Le, D., Lo, I., Zhan, L., Reichert, M. C., Sayed, F., Merlini, M., Ward, M. E., Perry, D. C., Lee, S. E., Sias, A., Parkhurst, C. N., Gan, W., Akassoglou, K., ... Gan, L. (2017). Microglial NFκB-TNFα hyperactivation induces obsessive–compulsive behavior in mouse models of progranulin-deficient frontotemporal dementia. *Proceedings of the National Academy of Sciences*, 114(19), 5029–5034. <https://doi.org/10.1073/pnas.1700477114>
- Lall, D., Lorenzini, I., Mota, T. A., Bell, S., Mahan, T. E., Ulrich, J. D., Davtyan, H., Rexach, J. E., Muhammad, A. K. M. G., Shelest, O., Landeros, J., Vazquez, M., Kim, J., Ghaffari, L., O'Rourke, J. G., Geschwind, D. H., Blurton-Jones, M., Holtzman, D. M., Sattler, R., & Baloh, R. H. (2021). C9orf72 deficiency promotes microglial-mediated synaptic loss in aging and amyloid accumulation. *Neuron*, 109(14), 2275-2291.e8. <https://doi.org/10.1016/j.neuron.2021.05.020>
- Lashley, Tammarn, Rohrer, J. D., Mahoney, C. J., Gordon, E., Beck, J., Mead, S., Warren, J. D., Rossor, M. N., & Revesz, T. (2014). A pathogenic progranulin mutation and C9orf72 repeat expansion in a family with frontotemporal dementia. *Neuropathology and Applied Neurobiology*, 40(4), 502–513. <https://doi.org/10.1111/nan.12100>
- Lee, S., Shang, Y., Redmond, S. A., Urisman, A., Tang, A. A., Li, K. H., Burlingame, A.

- L., Pak, R. A., Jovičić, A., Gitler, A. D., Wang, J., Gray, N. S., Seeley, W. W., Siddique, T., Bigio, E. H., Lee, V. M.-Y., Trojanowski, J. Q., Chan, J. R., & Huang, E. J. (2016). Activation of HIPK2 Promotes ER Stress-Mediated Neurodegeneration in Amyotrophic Lateral Sclerosis. *Neuron*, *91*(1), 41–55. <https://doi.org/10.1016/j.neuron.2016.05.021>
- Leroy, M., Bertoux, M., Skrobala, E., Mode, E., Adnet-Bonte, C., Le Ber, I., Bombois, S., Cassagnaud, P., Chen, Y., Deramecourt, V., Lebert, F., Mackowiak, M. A., Sillaire, A. R., Wathélet, M., Pasquier, F., Lebouvier, T., the Méotix network, Abied, R., Adnet, C., ... Verpoort, C. (2021). Characteristics and progression of patients with frontotemporal dementia in a regional memory clinic network. *Alzheimer's Research & Therapy*, *13*(1), 19. <https://doi.org/10.1186/s13195-020-00753-9>
- Levine, T. P., Daniels, R. D., Gatta, A. T., Wong, L. H., & Hayes, M. J. (2013). The product of C9orf72, a gene strongly implicated in neurodegeneration, is structurally related to DENN Rab-GEFs. *Bioinformatics*, *29*(4), 499–503. <https://doi.org/10.1093/bioinformatics/bts725>
- Liu, Y., Wang, T., Ji, Y. J., Johnson, K., Liu, H., Johnson, K., Bailey, S., Suk, Y., Lu, Y.-N., Liu, M., & Wang, J. (2018). A C9orf72–CARM1 axis regulates lipid metabolism under glucose starvation-induced nutrient stress. *Genes & Development*, *32*(21–22), 1380–1397. <https://doi.org/10.1101/gad.315564.118>
- Lui, H., Zhang, J., Makinson, S. R., Cahill, M. K., Kelley, K. W., Huang, H.-Y., Shang, Y., Oldham, M. C., Martens, L. H., Gao, F., Coppola, G., Sloan, S. A., Hsieh, C. L., Kim, C. C., Bigio, E. H., Weintraub, S., Mesulam, M.-M., Rademakers, R.,

- Mackenzie, I. R., ... Huang, E. J. (2016). Progranulin Deficiency Promotes Circuit-Specific Synaptic Pruning by Microglia via Complement Activation. *Cell*, 165(4), 921–935. <https://doi.org/10.1016/j.cell.2016.04.001>
- Marsan, E., Velmeshev, D., Ramsey, A., Patel, R. K., Zhang, J., Koontz, M., Andrews, M. G., De Majo, M., Mora, C., Blumenfeld, J., Li, A. N., Spina, S., Grinberg, L. T., Seeley, W. W., Miller, B. L., Ullian, E. M., Krummel, M. F., Kriegstein, A. R., & Huang, E. J. (2023). Astroglial toxicity promotes synaptic degeneration in the thalamocortical circuit in frontotemporal dementia with GRN mutations. *Journal of Clinical Investigation*, 133(6), e164919. <https://doi.org/10.1172/JCI164919>
- Martens, L. H., Zhang, J., Barmada, S. J., Zhou, P., Kamiya, S., Sun, B., Min, S.-W., Gan, L., Finkbeiner, S., Huang, E. J., & Farese, R. V. (2012). Progranulin deficiency promotes neuroinflammation and neuron loss following toxin-induced injury. *Journal of Clinical Investigation*, 122(11), 3955–3959. <https://doi.org/10.1172/JCI63113>
- McCauley, M. E., O'Rourke, J. G., Yáñez, A., Markman, J. L., Ho, R., Wang, X., Chen, S., Lall, D., Jin, M., Muhammad, A. K. M. G., Bell, S., Landeros, J., Valencia, V., Harms, M., Arditi, M., Jefferies, C., & Baloh, R. H. (2020a). C9orf72 in myeloid cells suppresses STING-induced inflammation. *Nature*, 585(7823), 96–101. <https://doi.org/10.1038/s41586-020-2625-x>
- McCauley, M. E., O'Rourke, J. G., Yáñez, A., Markman, J. L., Ho, R., Wang, X., Chen, S., Lall, D., Jin, M., Muhammad, A. K. M. G., Bell, S., Landeros, J., Valencia, V., Harms, M., Arditi, M., Jefferies, C., & Baloh, R. H. (2020b). C9orf72 in myeloid cells suppresses STING-induced inflammation. *Nature*, 585(7823), 96–101.

<https://doi.org/10.1038/s41586-020-2625-x>

- Merlini, M., Kirabali, T., Kulic, L., Nitsch, R. M., & Ferretti, M. T. (2018). Extravascular CD3+ T Cells in Brains of Alzheimer Disease Patients Correlate with Tau but Not with Amyloid Pathology: An Immunohistochemical Study. *Neurodegenerative Diseases*, *18*(1), 49–56. <https://doi.org/10.1159/000486200>
- Miller, Z. A., Rankin, K. P., Graff-Radford, N. R., Takada, L. T., Sturm, V. E., Cleveland, C. M., Criswell, L. A., Jaeger, P. A., Stan, T., Heggeli, K. A., Hsu, S. C., Karydas, A., Khan, B. K., Grinberg, L. T., Gorno-Tempini, M. L., Boxer, A. L., Rosen, H. J., Kramer, J. H., Coppola, G., ... Miller, B. L. (2013). TDP-43 frontotemporal lobar degeneration and autoimmune disease. *Journal of Neurology, Neurosurgery & Psychiatry*, *84*(9), 956–962. <https://doi.org/10.1136/jnnp-2012-304644>
- Miller, Z. A., Sturm, V. E., Camsari, G. B., Karydas, A., Yokoyama, J. S., Grinberg, L. T., Boxer, A. L., Rosen, H. J., Rankin, K. P., Gorno-Tempini, M. L., Coppola, G., Geschwind, D. H., Rademakers, R., Seeley, W. W., Graff-Radford, N. R., & Miller, B. L. (2016). Increased prevalence of autoimmune disease within C9 and FTD/MND cohorts: Completing the picture. *Neurology Neuroimmunology & Neuroinflammation*, *3*(6), e301. <https://doi.org/10.1212/NXI.0000000000000301>
- Minami, S. S., Min, S.-W., Krabbe, G., Wang, C., Zhou, Y., Asgarov, R., Li, Y., Martens, L. H., Elia, L. P., Ward, M. E., Mucke, L., Farese, R. V., & Gan, L. (2014). Progranulin protects against amyloid β deposition and toxicity in Alzheimer's disease mouse models. *Nature Medicine*, *20*(10), 1157–1164. <https://doi.org/10.1038/nm.3672>
- Mountz, J. D., Gause, W. C., Finkelman, F. D., & Steinberg, A. D. (1988). Prevention of

lymphadenopathy in MRL-lpr/lpr mice by blocking peripheral lymph node homing with Mel-14 in vivo. *The Journal of Immunology*, 140(9), 2943–2949.

<https://doi.org/10.4049/jimmunol.140.9.2943>

Nguyen, A. D., Nguyen, T. A., Zhang, J., Devireddy, S., Zhou, P., Karydas, A. M., Xu, X., Miller, B. L., Rigo, F., Ferguson, S. M., Huang, E. J., Walther, T. C., & Farese, R. V. (2018). Murine knockin model for progranulin-deficient frontotemporal dementia with nonsense-mediated mRNA decay. *Proceedings of the National Academy of Sciences*, 115(12). <https://doi.org/10.1073/pnas.1722344115>

Olney, N. T., Spina, S., & Miller, B. L. (2017). Frontotemporal Dementia. *Neurologic Clinics*, 35(2), 339–374. <https://doi.org/10.1016/j.ncl.2017.01.008>

Olszewska, D. A., Lonergan, R., Fallon, E. M., & Lynch, T. (2016). Genetics of Frontotemporal Dementia. *Current Neurology and Neuroscience Reports*, 16(12), 107. <https://doi.org/10.1007/s11910-016-0707-9>

O'Rourke, J. G., Bogdanik, L., Yáñez, A., Lall, D., Wolf, A. J., Muhammad, A. K. M. G., Ho, R., Carmona, S., Vit, J. P., Zarrow, J., Kim, K. J., Bell, S., Harms, M. B., Miller, T. M., Dangler, C. A., Underhill, D. M., Goodridge, H. S., Lutz, C. M., & Baloh, R. H. (2016). *C9orf72* is required for proper macrophage and microglial function in mice. *Science*, 351(6279), 1324–1329. <https://doi.org/10.1126/science.aaf1064>

Pierce, S. K. (2009). Understanding B cell activation: From single molecule tracking, through Tolls, to stalking memory in malaria. *Immunologic Research*, 43(1–3), 85–97. <https://doi.org/10.1007/s12026-008-8052-y>

Pisetsky, D. S. (2023). Pathogenesis of autoimmune disease. *Nature Reviews*

- Nephrology*, 19(8), 509–524. <https://doi.org/10.1038/s41581-023-00720-1>
- Pottier, C., Ravenscroft, T. A., Sanchez-Contreras, M., & Rademakers, R. (2016). Genetics of FTLN: Overview and what else we can expect from genetic studies. *Journal of Neurochemistry*, 138(S1), 32–53. <https://doi.org/10.1111/jnc.13622>
- Pottier, C., Ren, Y., Perkerson, R. B., Baker, M., Jenkins, G. D., Van Blitterswijk, M., DeJesus-Hernandez, M., Van Rooij, J. G. J., Murray, M. E., Christopher, E., McDonnell, S. K., Fogarty, Z., Batzler, A., Tian, S., Vicente, C. T., Matchett, B., Karydas, A. M., Hsiung, G.-Y. R., Seelaar, H., ... Rademakers, R. (2019). Genome-wide analyses as part of the international FTLN-TDP whole-genome sequencing consortium reveals novel disease risk factors and increases support for immune dysfunction in FTLN. *Acta Neuropathologica*, 137(6), 879–899. <https://doi.org/10.1007/s00401-019-01962-9>
- Religa, D., Fereshtehnejad, S.-M., Cermakova, P., Edlund, A.-K., Garcia-Plata, S., Granqvist, N., Hallbäck, A., Kåwe, K., Farahmand, B., Kilander, L., Mattsson, U.-B., Nägga, K., Nordström, P., Wijk, H., Wimo, A., Winblad, B., & Eriksdotter, M. (2015). SveDem, the Swedish Dementia Registry – A Tool for Improving the Quality of Diagnostics, Treatment and Care of Dementia Patients in Clinical Practice. *PLOS ONE*, 10(2), e0116538. <https://doi.org/10.1371/journal.pone.0116538>
- Rohrer, J. D., Guerreiro, R., Vandrovicova, J., Uphill, J., Reiman, D., Beck, J., Isaacs, A. M., Authier, A., Ferrari, R., Fox, N. C., Mackenzie, I. R. A., Warren, J. D., De Silva, R., Holton, J., Revesz, T., Hardy, J., Mead, S., & Rossor, M. N. (2009). The heritability and genetics of frontotemporal lobar degeneration. *Neurology*,

- 73(18), 1451–1456. <https://doi.org/10.1212/WNL.0b013e3181bf997a>
- Rosso, S. M. (2003). Frontotemporal dementia in The Netherlands: Patient characteristics and prevalence estimates from a population-based study. *Brain*, 126(9), 2016–2022. <https://doi.org/10.1093/brain/awg204>
- Sabatino, J. J., Pröbstel, A.-K., & Zamvil, S. S. (2019). B cells in autoimmune and neurodegenerative central nervous system diseases. *Nature Reviews Neuroscience*, 20(12), 728–745. <https://doi.org/10.1038/s41583-019-0233-2>
- Sachinidis, A., Xanthopoulos, K., & Garyfallos, A. (2020). Age-Associated B Cells (ABCs) in the Prognosis, Diagnosis and Therapy of Systemic Lupus Erythematosus (SLE). *Mediterranean Journal of Rheumatology*, 31(3), 311. <https://doi.org/10.31138/mjr.31.3.311>
- Salazar, D. A., Butler, V. J., Argouarch, A. R., Hsu, T.-Y., Mason, A., Nakamura, A., McCurdy, H., Cox, D., Ng, R., Pan, G., Seeley, W. W., Miller, B. L., & Kao, A. W. (2015). The Progranulin Cleavage Products, Granulins, Exacerbate TDP-43 Toxicity and Increase TDP-43 Levels. *Journal of Neuroscience*, 35(25), 9315–9328. <https://doi.org/10.1523/JNEUROSCI.4808-14.2015>
- Santiago-Raber, M.-L., Baudino, L., & Izui, S. (2009). Emerging roles of TLR7 and TLR9 in murine SLE. *Journal of Autoimmunity*, 33(3–4), 231–238. <https://doi.org/10.1016/j.jaut.2009.10.001>
- Santiago-Raber, M.-L., Dunand-Sauthier, I., Wu, T., Li, Q.-Z., Uematsu, S., Akira, S., Reith, W., Mohan, C., Kotzin, B. L., & Izui, S. (2010). Critical role of TLR7 in the acceleration of systemic lupus erythematosus in TLR9-deficient mice. *Journal of Autoimmunity*, 34(4), 339–348. <https://doi.org/10.1016/j.jaut.2009.11.001>

- Shang, Y., Zhang, J., & Huang, E. J. (2018). HIPK2-Mediated Transcriptional Control of NMDA Receptor Subunit Expression Regulates Neuronal Survival and Cell Death. *The Journal of Neuroscience: The Official Journal of the Society for Neuroscience*, *38*(16), 4006–4019. <https://doi.org/10.1523/JNEUROSCI.3577-17.2018>
- Sharma, K., Schmitt, S., Bergner, C. G., Tyanova, S., Kannaiyan, N., Manrique-Hoyos, N., Kongi, K., Cantuti, L., Hanisch, U.-K., Philips, M.-A., Rossner, M. J., Mann, M., & Simons, M. (2015). Cell type– and brain region–resolved mouse brain proteome. *Nature Neuroscience*, *18*(12), 1819–1831. <https://doi.org/10.1038/nn.4160>
- Smith, K. R., Damiano, J., Franceschetti, S., Carpenter, S., Canafoglia, L., Morbin, M., Rossi, G., Pareyson, D., Mole, S. E., Staropoli, J. F., Sims, K. B., Lewis, J., Lin, W.-L., Dickson, D. W., Dahl, H.-H., Bahlo, M., & Berkovic, S. F. (2012). Strikingly Different Clinicopathological Phenotypes Determined by Progranulin-Mutation Dosage. *The American Journal of Human Genetics*, *90*(6), 1102–1107. <https://doi.org/10.1016/j.ajhg.2012.04.021>
- Sullivan, P. M., Zhou, X., Robins, A. M., Paushter, D. H., Kim, D., Smolka, M. B., & Hu, F. (2016). The ALS/FTLD associated protein C9orf72 associates with SMCR8 and WDR41 to regulate the autophagy-lysosome pathway. *Acta Neuropathologica Communications*, *4*(1), 51. <https://doi.org/10.1186/s40478-016-0324-5>
- Testi, S., Tamburin, S., Zanette, G., & Fabrizi, G. M. (2015). Co-Occurrence of the C9ORF72 Expansion and a Novel GRN Mutation in a Family with Alternative

Expression of Frontotemporal Dementia and Amyotrophic Lateral Sclerosis.
Journal of Alzheimer's Disease, 44(1), 49–56. <https://doi.org/10.3233/JAD-141794>

Thurman, J. M., & Yapa, R. (2019). Complement Therapeutics in Autoimmune Disease.
Frontiers in Immunology, 10, 672. <https://doi.org/10.3389/fimmu.2019.00672>

Van Blitterswijk, M., Baker, M. C., DeJesus-Hernandez, M., Ghidoni, R., Benussi, L., Finger, E., Hsiung, G.-Y. R., Kelley, B. J., Murray, M. E., Rutherford, N. J., Brown, P. E., Ravenscroft, T., Mullen, B., Ash, P. E. A., Bieniek, K. F., Hatanpaa, K. J., Karydas, A., Wood, E. M., Coppola, G., ... Rademakers, R. (2013). C9ORF72 repeat expansions in cases with previously identified pathogenic mutations. *Neurology*, 81(15), 1332–1341.
<https://doi.org/10.1212/WNL.0b013e3182a8250c>

Van Damme, P., Van Hoecke, A., Lambrechts, D., Vanacker, P., Bogaert, E., Van Swieten, J., Carmeliet, P., Van Den Bosch, L., & Robberecht, W. (2008). Progranulin functions as a neurotrophic factor to regulate neurite outgrowth and enhance neuronal survival. *The Journal of Cell Biology*, 181(1), 37–41.
<https://doi.org/10.1083/jcb.200712039>

Van Der Flier, W. M., & Scheltens, P. (2018). Amsterdam Dementia Cohort: Performing Research to Optimize Care. *Journal of Alzheimer's Disease*, 62(3), 1091–1111.
<https://doi.org/10.3233/JAD-170850>

Van Vliet, D., De Vugt, M. E., Bakker, C., Pijnenburg, Y. A. L., Vernooij-Dassen, M. J. F. J., Koopmans, R. T. C. M., & Verhey, F. R. J. (2013). Time to diagnosis in young-onset dementia as compared with late-onset dementia. *Psychological Medicine*,

43(2), 423–432. <https://doi.org/10.1017/S0033291712001122>

- Velmeshev, D., Schirmer, L., Jung, D., Haeussler, M., Perez, Y., Mayer, S., Bhaduri, A., Goyal, N., Rowitch, D. H., & Kriegstein, A. R. (2019). Single-cell genomics identifies cell type–specific molecular changes in autism. *Science*, *364*(6441), 685–689. <https://doi.org/10.1126/science.aav8130>
- Veys, E. M., Gabriel, P. A., Coigne, E., & Mielants, H. (1976). Rheumatoid factor and serum IgG, IgM and IgA levels in rheumatoid arthritis with vasculitis. *Scandinavian Journal of Rheumatology*, *5*(1), 1–6.
- Volkov, M., Coppola, M., Huizinga, R., Eftimov, F., Huizinga, T. W. J., Van Der Kooij, A. J., Oosten, L. E. M., Raaphorst, J., Rispens, T., Sciarrillo, R., Titulaer, M. J., Wieske, L., Toes, R. E. M., Huijbers, M. G. M., Van Schie, K. A., & Van Der Woude, D. (2022). Comprehensive overview of autoantibody isotype and subclass distribution. *Journal of Allergy and Clinical Immunology*, *150*(5), 999–1010. <https://doi.org/10.1016/j.jaci.2022.05.023>
- Wang, X., & Xia, Y. (2019). Anti-double Stranded DNA Antibodies: Origin, Pathogenicity, and Targeted Therapies. *Frontiers in Immunology*, *10*, 1667. <https://doi.org/10.3389/fimmu.2019.01667>
- Ward, M. E., Chen, R., Huang, H.-Y., Ludwig, C., Telpoukhovskaia, M., Taubes, A., Boudin, H., Minami, S. S., Reichert, M., Albrecht, P., Gelfand, J. M., Cruz-Herranz, A., Cordano, C., Alavi, M. V., Leslie, S., Seeley, W. W., Miller, B. L., Bigio, E., Mesulam, M.-M., ... Green, A. J. (2017). Individuals with progranulin haploinsufficiency exhibit features of neuronal ceroid lipofuscinosis. *Science Translational Medicine*, *9*(385), eaah5642.

<https://doi.org/10.1126/scitranslmed.aah5642>

Xiao, S., MacNair, L., McGoldrick, P., McKeever, P. M., McLean, J. R., Zhang, M., Keith, J., Zinman, L., Rogaeva, E., & Robertson, J. (2015). Isoform-specific antibodies reveal distinct subcellular localizations of C9orf72 in amyotrophic lateral sclerosis. *Annals of Neurology*, 78(4), 568–583.

<https://doi.org/10.1002/ana.24469>

Yang, M., Liang, C., Swaminathan, K., Herrlinger, S., Lai, F., Shiekhata, R., & Chen, J.-F. (2016). A C9ORF72/SMCR8-containing complex regulates ULK1 and plays a dual role in autophagy. *Science Advances*, 2(9), e1601167.

<https://doi.org/10.1126/sciadv.1601167>

Yin, F., Banerjee, R., Thomas, B., Zhou, P., Qian, L., Jia, T., Ma, X., Ma, Y., Iadecola, C., Beal, M. F., Nathan, C., & Ding, A. (2010). Exaggerated inflammation, impaired host defense, and neuropathology in progranulin-deficient mice. *Journal of Experimental Medicine*, 207(1), 117–128.

<https://doi.org/10.1084/jem.20091568>

Zhang, J., Velmeshev, D., Hashimoto, K., Huang, Y.-H., Hofmann, J. W., Shi, X., Chen, J., Leidal, A. M., Dishart, J. G., Cahill, M. K., Kelley, K. W., Liddel, S. A., Seeley, W. W., Miller, B. L., Walther, T. C., Farese, R. V., Taylor, J. P., Ullian, E. M., Huang, B., ... Huang, E. J. (2020). Neurotoxic microglia promote TDP-43 proteinopathy in progranulin deficiency. *Nature*, 588(7838), 459–465.

<https://doi.org/10.1038/s41586-020-2709-7>

Zhang, W., Chen, Y., & Pei, H. (2023). C1q and central nervous system disorders. *Frontiers in Immunology*, 14, 1145649.

<https://doi.org/10.3389/fimmu.2023.1145649>

Zhang, W., Xiao, D., Mao, Q., & Xia, H. (2023). Role of neuroinflammation in neurodegeneration development. *Signal Transduction and Targeted Therapy*, 8(1), 267. <https://doi.org/10.1038/s41392-023-01486-5>

Zhang, Y., Chen, K., Sloan, S. A., Bennett, M. L., Scholze, A. R., O’Keeffe, S., Phatnani, H. P., Guarnieri, P., Caneda, C., Ruderisch, N., Deng, S., Liddelow, S. A., Zhang, C., Daneman, R., Maniatis, T., Barres, B. A., & Wu, J. Q. (2014). An RNA-Sequencing Transcriptome and Splicing Database of Glia, Neurons, and Vascular Cells of the Cerebral Cortex. *The Journal of Neuroscience*, 34(36), 11929–11947. <https://doi.org/10.1523/JNEUROSCI.1860-14.2014>

Zhu, J., Nathan, C., Jin, W., Sim, D., Ashcroft, G. S., Wahl, S. M., Lacomis, L., Erdjument-Bromage, H., Tempst, P., Wright, C. D., & Ding, A. (2002). Conversion of Proepithelin to Epithelins. *Cell*, 111(6), 867–878. [https://doi.org/10.1016/S0092-8674\(02\)01141-8](https://doi.org/10.1016/S0092-8674(02)01141-8)

Publishing Agreement

It is the policy of the University to encourage open access and broad distribution of all theses, dissertations, and manuscripts. The Graduate Division will facilitate the distribution of UCSF theses, dissertations, and manuscripts to the UCSF Library for open access and distribution. UCSF will make such theses, dissertations, and manuscripts accessible to the public and will take reasonable steps to preserve these works in perpetuity.

I hereby grant the non-exclusive, perpetual right to The Regents of the University of California to reproduce, publicly display, distribute, preserve, and publish copies of my thesis, dissertation, or manuscript in any form or media, now existing or later derived, including access online for teaching, research, and public service purposes.

DocuSigned by:

Naznin Jahan

087C22AC53F4457...

Author Signature

3/17/2024

Date